PLASTICITY AS A DEPINNING PHASE TRANSITION

BY

GEORGIOS TSEKENIS

DISSERTATION

Submitted in partial fulfillment of the requirements
for the degree of Doctor of Philosophy in Physics
in the Graduate College of the
University of Illinois at Urbana-Champaign, 2012

Urbana, Illinois

Doctoral Committee:

Professor Alfred Hubler, Chair
Associate Professor Karin A. Dahmen, Director of Research
Professor Emeritus Michael Weismann
Professor David Ceperley

Abstract

Crystalline materials deform in an intermittent way with slip-avalanches that are power-law distributed. In this work we study plasticity as a pinning-depinning phase transition employing a discrete dislocation dynamics (DDD) model and a phase field crystal (PFC) model in two dimensions. Below a critical (flow) stress, the dislocations are pinned/jammed within their glide plane due to long-range elastic interactions and the material exhibits plastic response. Above this critical stress the dislocations are mobile (the depinned/unjammed phase) and the material constantly flows.

We employ discrete dislocation dynamics to resolve the temporal profiles of slip-avalanches and extract the finite-size scaling properties of the slip-avalanche statistics, going beyond gross aggregate statistics of slip avalanche sizes. We provide a comprehensive set of scaling exponents, including the depinning exponent β. Our work establishes that the dynamics of plasticity, in the absence of hardening, is consistent with the mean field interface depinning universality class, even though there is no quenched disorder.

We also use dislocation dynamics and scaling arguments in two dimensions to show that the critical stress grows with the square root of the dislocation density (Taylor's relation). Consequently, dislocations jam at any density, in contrast to granular materials, which only jam above a critical density.

Finally, we utilize a phase field crystal model to extract the size, energy and duration distributions of the avalanches and show that they exhibit power law behavior in agreement with the mean field interface depinning universality class.

To my Parents: Maria & Kostas,

to my Godfather Giannis,

to my Uncle Leonidas.

Acknowledgments

What a ride! It had everything: intense debates, deep soul searching, vices and a lot of different people. All in all a process of discovering the world and its peoples from up close and from deep inside. This project would not have been possible without the support of many people.

First and foremost I would like to thank my advisor Prof. Karin Dahmen. I learned a great deal from her. From basic science to networking and I am indebted to her for all. What I appreciate the most is that I was given the time to form my own opinion. I was given the opportunity to try and fail and learn my own way. I was able to follow my own path which I think is the best way for (determined/stubborn people like) me but still have her unwavering support and brilliant example on my side at all times. She was also comfortable trying new things and being positively influenced.

I would also like to thank Prof. Nigel Goldenfeld who served to me as another advisor. I have come to appreciate his "interest in everything" and his passion to differ by sticking to ones own truthful view of the world.

I have come to interact with several members of the Dahmen group. I was office mates with Dr. Yang Liu (now at Northeastern U) for many years. That allowed us to interact very closely and form a very solid friendship for years to come. I really appreciate his openness and objectivity as well as his strive to excel. Dr. A. Missel and Dr. M. Delgado helped me in my beginnings. I am leaving several strong and eager-for-success students: Mr. N. Friedman, Mr. B. A. W. Brinkman, Mr. T. M. Earnest all helped me a lot and taught me equally as much. I am particularly content to see Mr. N. Friedman assume the greater roles he can fulfill. Also I am very happy to have interacted with Mr. T. Fehm (now at Ludwig-Maximilians-U) and I hope we will interact more in the future. I want to wish good luck to the new members of the Dahmen Group: Mr. M. Leblanc, Mr. W. Benalcazar, Mr. M. Wraith.

I have come to meet and interact with several members of the Goldenfeld Group as well. Dr. Pak Yuen Chan did an awesome job with the phase field crystal model and set an excellent graduate student example for me. Also I have enjoyed and hope will keep enjoying interesting scientific interactions with, and advice from, Dr. M. Assaf and Dr. L. Angheluta.

Prof. M.-C. Miguel (U Barcelona) not only spend a considerable amount of time with us when we were still trying to understand the problem and her model but also gave her honest opinion about her results and encouraged us to proceed forward with ours even though some were going to correct some of hers. She even came to visit us in Illinois.

Prof. J. R. Greer (Caltech) served as another brilliant and successful scientist example. I would like to thank her for sharing her experimental data and positive attitude with us.

Prof. M. Zaiser (U of Edinburg) and Prof. J. Weiss (CNRS, Grenoble, France) both spent several hours with me back in 2007 in Todi, Perugia, Italy when I was still an aspiring scientist and shared with me all of their experience and concerns on small-scale plasticity. I am thankful to both of them for taking the time to convey their knowledge and setting an example of good open science.

Prof. S. Nagel (U Chicago) and Prof. H. Jaeger (U Chicago) spent the time to discuss physics with me and showed me how it is to be really good at what you do and enjoy it through their friendship.

Prof. R. Weaver (U Illinois) and Dr. D. Mertens (Northwestern U) were only there to help unreluctantly.

Prof. Y. Oono (U Illinois) tingled my brain during our conversations and gave me his book to read for free. With Dr. J. Tan and Mr. O. Osuagwu we had countless stimulating conversations about economics and politics, driving and spicy food.

Prof. K. Schulten (U Illinois) and Dr. Robert Brunner (U Illinois) and Dr. V. Paschalidis (U Illinois) showed interest in my research and computational efforts and backed me up with their experience and knowledge.

Prof. J. Sethna (Cornell U) and Dr. S. Papanikolaou (Cornell U) discussed with us a lot as we often found ourselves in parallel science.

I would also like to thank my Prelim and Final Defense Committee. Prof. Alfred Hubler gave me a chance to present my work in his class and experience how it is to cause someone else to be inspired. He has done that to me with his unconventional research. Prof. D. Ceperley besides giving me specific ideas to speed up my simulation considerably ("look-up" table) he also served as an example with his simple and powerful intuition in physics. Finally Prof. M. Weismann has inspired me with his personal life and career choices although he may not know it.

The research presented in this Thesis was supported in part by the National Science Foundation grant DMR 03-25939 ITR through the Materials Computation Center at the University of Illinois and NSF grant DMR 1005209. Any opinions, findings, and conclusions or recommendations expressed in this publication are those of the author(s) and do not necessarily reflect the views of the National Science Foundation.

We also thank the University of Illinois for funding, support and hospitality. Prof. J. Stack has been an

awesome graduate student advisor and Prof. L. Cooper is putting in the effort to outdo him in awesomeness. Mrs. J. Wilde served as an amazing undergraduate student secretary and very good to me as a Teaching Assistant. Also Mrs. W. R. Wimmer assistant to the graduate student advisor did not hesitate to help me when I needed her.

The authors gratefully acknowledge the use of the Turing and Taub cluster maintained and operated by the Computational Science and Engineering Program at the University of Illinois.

This research was also supported in part by the National Science Foundation through TeraGrid resources provided by the Texas Advanced Computing Center and the National Center for Supercomputing Applications under grant number TG-DMR090061. We specifically acknowledge the technical assistance of J. Estabrook and A. Wettstein.

I have made a lot of friends in this process and I have grown considerably first as a person and second into a full fledged researcher. I want to acknowledge here the people that touched my heart, soul, and mind. Costis, Vivi, Stratos, Elizabeth, Lee, Sasha, Stan. I would also like to thank my old good friends that supported me throughout this PhD: Giorgos and Antonis. And Dan and Dan for sharing the fun. I made a ton of good friends and am still meeting awesome people that benefit me everyday: Ayush, Cesar, Sara, Marinos, Pete, Aaron, Jessica & Nepheli, Max & Masha, Daniel, Elitsa, Matias, Aya. Finally I would like to thank the Sellountos Family for taking care of me as one of their own.

Table of Contents

List of Abbreviations

MFT	Mean Field Theory.
DDD	Discrete Dislocation Dynamics.
PFC	Phase Field Crystal.
PF	Phase Field.
AE	Acoustic Emission.

List of Symbols

t	time.
T	temperature
γ	shear strain.
τ	shear stress.
τ_c	critical shear stress.
N	number of dislocations.
L	linear side of simulation cell.
ρ	dislocation density.
b	Burger's vector.

$V(t) = \sum_{i=1}^{N} |v_i(t)|$ collective dislocation speed (or acoustic emission signal).

$V'(t) \sum_{i=1}^{N} b_i v_i(t)$ collective dislocation velocity (or strain rate).

$S = \int_{\text{avalanche}} V(t)dt = \left(\sum_{i=1}^{N} |\Delta x_i| \right)_{\text{avalanche}}$ slip avalanche size.

$S' = \int_{\text{avalanche}} V'(t)dt = \left(\sum_{i=1}^{N} b_i \Delta x_i \right)_{\text{avalanche}} = \Delta\gamma_{\text{avalanche}}$ slip avalanche size.

D_S	probability distribution of slip avalanche sizes at fixed stress.
$D_{S,\text{int}}$	probability distribution of slip avalanche sizes for all stresses.
t_{aval}	slip avalanche duration.
D_t	probability distribution of slip avalanche duration at fixed stress.
$D_{t,\text{int}}$	probability distribution of slip avalanche durations for all stresses.

$E = \int_{\text{avalanche}} V(t)^2 dt$ slip avalanche energy.

D_E	probability distribution of slip avalanche energies at fixed stress.
$D_{E,\text{int}}$	probability distribution of slip avalanche energies for all stresses.
ω	angular frequency.
PS	power spectrum.
β	depinning exponent.
ν	correlation length and finite-size effect exponent.

ζ	roughness exponent.
z	dynamic exponent.
κ	power law exponent of slip avalanche size distribution.
σ	exponent of maximum size (or distribution cutoff size).
δ	temperature or thermal exponent.
f	generic scaling function
f_S	scaling function of the probability distribution of slip avalanche sizes at fixed stress.
f_t	scaling function of the probability distribution of slip avalanche durations at fixed stress.
f_E	scaling function of the probability distribution of slip avalanche energies at fixed stress.

Chapter 1

Overview

1.1 Thesis Outline

In Chapter 1 (here) we give an overview of what this Thesis is about and the research efforts that went into it as well as publications that already resulted from this work or are in preparation. The topic: Plasticity as a depinning phase transition.

In Chapter 2 we provide an introduction to plasticity starting from how it was originally approached phenomenologically and how in the last years discoveries on small scales came to suggest it as a mean field interface depinning transition. More specifically in Section 2.1 we present how traditional plasticity theory was built as a continuum theory. The metallurgist community used continuum models to study the strength of a piece of metal. The deforming body is assumed to behave smoothly in time and in space. At sufficiently small scales where the presence of dislocations can be observed the previous assumption seizes being a good approximation. In Section 2.2 we introduce dislocations; they break the translational symmetry of the ideal crystal. Dislocations allow the atoms of crystalline materials to move and consequently enable the solid to deform. The dislocations interact via long-range non-local stress fields. The dislocation network exhibits avalanches and collective behavior. On small scales crystalline materials deform in a jerky manner that is intermittent in time and inhomogeneous in space. Plastic response to external stress is characterized by slip avalanches of many orders of magnitude in size. Lastly in Section 2.3 we explain how plasticity can be studied as a depinning non-equilibrium phase transition. The material is pinned and the dislocations are jammed below the flow stress. The material is constantly flowing and the dislocations are unjammed above the flow stress. The slip avalanches grow bigger as the flow stress is approached.

In Chapter 3 we review ground breaking experiments that investigated plasticity on tiny length scales. Experiments in micro- and nano- crystals revealed power law distributed avalanche behavior as the material slips under stress.

In Chapter 4 we discuss the computational models that were employed to shed light on the experimental findings on the avalanche statistics. Besides the continuum models that were phenomenologically adapted

to explain the intermittent character of plasticity, new models of interacting dislocations were invented in an effort to study the dislocations' collective behavior. The majority of the experimental and computational results indicate that plasticity can be studied as a depinning phase transition.

At its maturity this massive effort revealed that (mainly) the static aspects of plasticity may belong to the mean field interface depinning universality class. There were some unresolved inconsistencies reported, however. For example dynamic properties such as power spectra, temporal avalanches profiles and the depinning exponent extracted from simulations did not match mean field theoretical (MFT) predictions. In this Thesis we report on the results of our careful analysis of extensive numerical simulations. We show that both the static properties and the dynamic properties of plasticity are fully consistent with the MFT predictions. So in Chapter 5 we present the mean field theory (MFT) of a generic interface depinning model.

In Chapter 6 we give the details of the discrete dislocation dynamics (DDD) model we implemented.

And in Chapter 7 we present our results from the discrete dislocation model at zero temperature. We extract the average slip avalanche speed profiles (shapes). We find that the profiles are self-similar and do in fact collapse with a MF critical exponent. The scaling function is a parabola as indicated by MFT. We calculate the power spectra of the computational acoustic emission signal and find that it matches with the average temporal avalanche profiles and MFT predictions. We also study the finite-size effects on the avalanches and show that they too agree with MFT. We extract the depinning exponent of the transition which agrees with MFT as well. All in all we provide an extensive set (Table 7.1) of newly (and correctly) calculated critical exponents that show that not only the statics and aggregate statistics of avalanches but also the dynamics of plasticity are in agreement with the mean field interface depinning universality class.

In Chapter 8 we study the critical (flow) stress with dislocation density and we suggest a putative jamming phase diagram for dislocations in which there is no jamming point. Based on discrete dislocation dynamics simulations and analytical scaling arguments we show that dislocations (and by analogy particles with long-range interactions) will require a non-zero external shear stress to unjam for any finite density. This behavior is distinctly different from granular materials where grains interact via short-range interactions and the material exhibits zero shear modulus for a low enough (but finite) density.

In Chapter 9 we present a modern phase field crystal (PFC) model to study the effect of finite temperature on plasticity.

And in Chapter 10 we show that the phase field crystal model exhibits plastic response through slip avalanches when we shear it at a fixed strain rate and a given temperature. The slip avalanches exhibit power law statistics that are consistent with the mean field interface depinning universality class.

Lastly in Chapter 11 we retell the story of plasticity and present the exciting future possibilities of our

work.

1.2 Research Challenges and Collaborations

I developed and ran the discrete dislocation dynamics simulations. It was quite a feat building a code of objects interacting long range. I also collected and analyzed the data above and below the flow stress. With the help of Mr. B. A. W. Brinkman graduate student in our group we came up with analytical scaling arguments for the jamming of dislocations. On all aspects of my research, from understanding the problem to preparing publications I enjoyed guidance by my advisor Prof. Karin Dahmen and from Prof. Nigel Goldenfeld (both at the Physics Department of the University of Illinois at Urbana). I then gave the experience I developed to Mr. N. Friedman (another graduate student in our group) and helped analyze experimental data from Prof. J. R. Greer's group (Material Science and Mechanics, Caltech). Our findings in deforming nano-crystals will appear in the literature soon.

The phase field crystal model was developed by Prof. Nigel Goldenfeld (Physics), Prof. Jonathan Dantzig (Mechanical Engineering) and Dr. Pak Yuen Chan (Physics) who also built and run the PFC code. I was involved in analyzing the data and extracting the scaling characteristics of the crystal under shear relying on the expertise of Prof. Karin Dahmen on non-equilibrium critical phenomena. A wealth of data was produced by Mr. Thomas Fehm (Physics, Illinois and Ludwig-Maximilians-Universität München) in our group under my guidance. Those data gave me better statistics and reduced errorbars allowing me to obtain considerably cleaner avalanche distributions.

1.3 Publications

Our work at zero temperature with the discrete dislocation dynamics model has already given us a Physical Review Letter on the modern topic of dislocation jamming. Very recently we submitted for publication another manuscript to Physical Review Letters. It is on our results of the scaling of the dynamic characteristics of plasticity. We expect to put together a longer paper to submit to Physical Review E where we present all the details of our work with the discrete dislocation dynamics. Finally our observation of slip avalanches with the phase field crystal model resulted into a published Physical Review Letter as well. Currently with Thomas Fehm we are exploring the effect of temperature on the depinning transition of plasticity.

Chapter 2

Introduction to Plasticity

2.1 Homogeneous Plasticity; Traditional Continuum Mechanics

[1]Plastic deformation remains on the solid body after the external driving force has been removed. Elastic deformation disappears in the absence of the external force. The two kinds of deformation are distinctly different from each other. At the same time they are complementary to each other. The two kinds of deformation are sufficient and necessary to describe in a simple way the effect of an external force on a solid material.

In general plasticity is isochoric (i.e. constant volume) and irreversible in the thermodynamic sense. It is associated with hysteresis, a non-equilibrium phenomenon. For small strains the total strain, γ, is composed of an elastic and a plastic part

$$\gamma = \gamma_{\text{elastic}} + \gamma_{\text{plastic}} \tag{2.1}$$

The elastic strain is directly proportional to the external stress, τ, (this is Hook's law)

$$\tau \propto \gamma_{\text{elastic}} \tag{2.2}$$

and will vanish once the external stress is removed denoting a reversible process while the plastic strain will remain. Here we work with shear stress, τ, and shear strain, γ [2].

In order to proceed we need to relate plastic strain to external stress. The simplest approach, termed ideal plasticity, is rate-independent. In this case the solid deforms elastically for external stresses up to the yield stress, τ_y. Plastic deformation ensues once the yield stress is reached. The solid deforms constantly with the applied stress at τ_y and experiences a permanent plastic deformation, γ_{plastic} measurable on the body, when the stress is removed (Fig. 2.1).

[1]For this introduction we found particularly elucidating Zaiser's review [1].

[2]In this thesis we exclusively study shear stress and strain and we do not deal with transformation plasticity where the solid transitions to a different crystal structure.

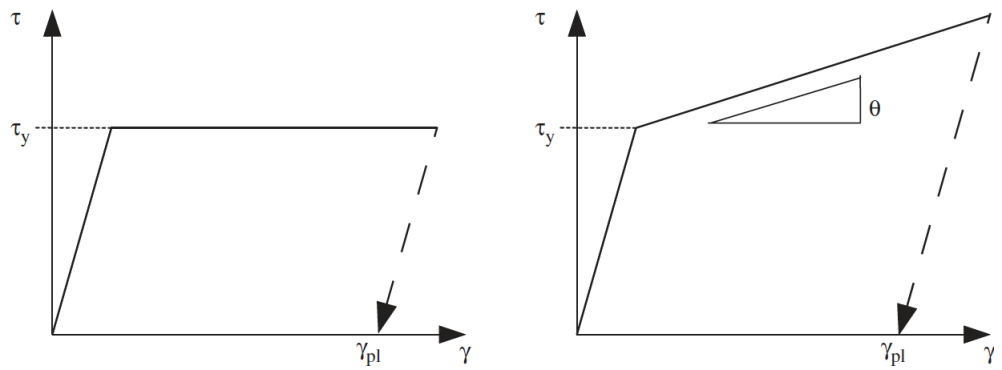

Figure 2.1: Strain-rate independent plasticity. Ideal plasticity without hardening (left) and with hardening (right). The figure is taken from Zaiser [1], Scale invariance in plastic flow of crystalline solids, M. Zaiser, Advances in Physics, 55(1):185-245, 2006, Taylor & Francis, reprinted by permission of the publisher (Taylor & Francis Ltd, http://www.tandfonline.com).

We can amend the rate-independent approach to include strain hardening, the fact that the yield stress can increase with strain. In other words the added stress needed to plastically deform a body, $\tau - \tau_y$, increases with increasing plastic strain, with the simplest relationship being the linear,

$$\tau - \tau_y \propto \gamma_{\text{plastic}}. \tag{2.3}$$

Note that for applied stress less than the yield stress Hook's law holds, Eq. (2.2). The slope of the stress-strain curve for the plastic part of the deformation is the strain-hardening coefficient, θ.

$$\theta = \frac{\partial \gamma_{\text{plastic}}}{\partial \tau} = \frac{\partial \gamma}{\partial \tau_y} \tag{2.4}$$

A more sophisticated approach is to account for a rate-dependent deformation process (Fig. 2.2). Linear viscoplasticity describes a solid that requires an increasing applied stress to flow

$$\dot{\gamma} \propto \begin{cases} \tau - \tau_y & \text{for} \quad \tau > \tau_y > 0 \\ 0 & \text{for} \quad 0 < \tau < \tau_y \end{cases} \tag{2.5}$$

The applied stress above the yield stress needed for plastic flow is called flow stress, τ_f, and is a function of the deformation rate,

$$\tau_f(\dot{\gamma}) = \tau_y + \mu\dot{\gamma}. \tag{2.6}$$

μ is the viscoplastic coefficient of the material assumed constant here. The above reduces to the rate-

independent plastic deformation for $\mu\dot{\gamma} << \tau_y$ and the flow stress coincides with the yield stress. Other reasonable phenomenological approximations to the stress-strain curve are the power law and the saturation exponential model which seems to describe well a number of aluminum alloys [2].

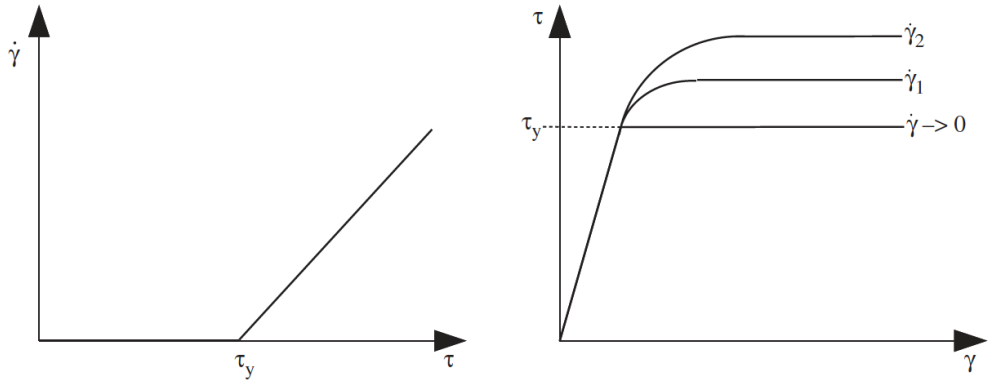

Figure 2.2: Plasticity with linear dependence on strain rate. Strain rate vs stress (left) and stress vs strain for different strain rates (right). The figure is taken from Zaiser [1], Scale invariance in plastic flow of crystalline solids, M. Zaiser, Advances in Physics, 55(1):185-245, 2006, Taylor & Francis, reprinted by permission of the publisher (Taylor & Francis Ltd, http://www.tandfonline.com).

The overarching notion in traditional continuum mechanics is that plasticity of crystalline solids is considered to be smooth in time, and homogenous in space, since fluctuations are supposed to average out at "large enough" spatial scales. In special cases though small fluctuations in strain, $\delta\gamma$, can become underdamped and grow considerably and one has a plastic instability. For example one gets a strain softening instability when θ becomes negative under constant stress rate loading. Under constant strain rate deformation conditions and when $\mu < 0$ one gets a strain rate softening instability. These include non-linear oscillations, traveling waves, deformation localization, patterning and chaos. In general plastic instabilities reveal characteristic internal time and length scales. We will see in Sections below how these hypotheses cannot fully describe the deformation process at small scales and the interactions of discrete dislocations give rise to power law distributed phenomena of many decades.

2.2 Dislocation-based Plasticity, A Collective Phenomenon

In this Thesis we study plasticity from the point of view of critical phenomena. In plastically deforming solids collective dislocation motion gives rise to slip avalanches that span many orders of magnitude and lack a characteristic length scale. The traditional picture and approach to plasticity discussed above becomes increasingly unable to describe deformation in smaller spatial scales and we must follow a fundamentally different approach. At "small enough" spatial scales one can actually observe the intermittent motion of

dislocations.

A dislocation is, in short, the topological boundary of a crystal half plane that does not preserve the periodicity of a perfect crystal [3]. An edge dislocation and a screw dislocation are shown in Fig. 2.3. In real crystalline solids both kinds are present, as well as mixed dislocation lines with segments that can be of edge or screw character.

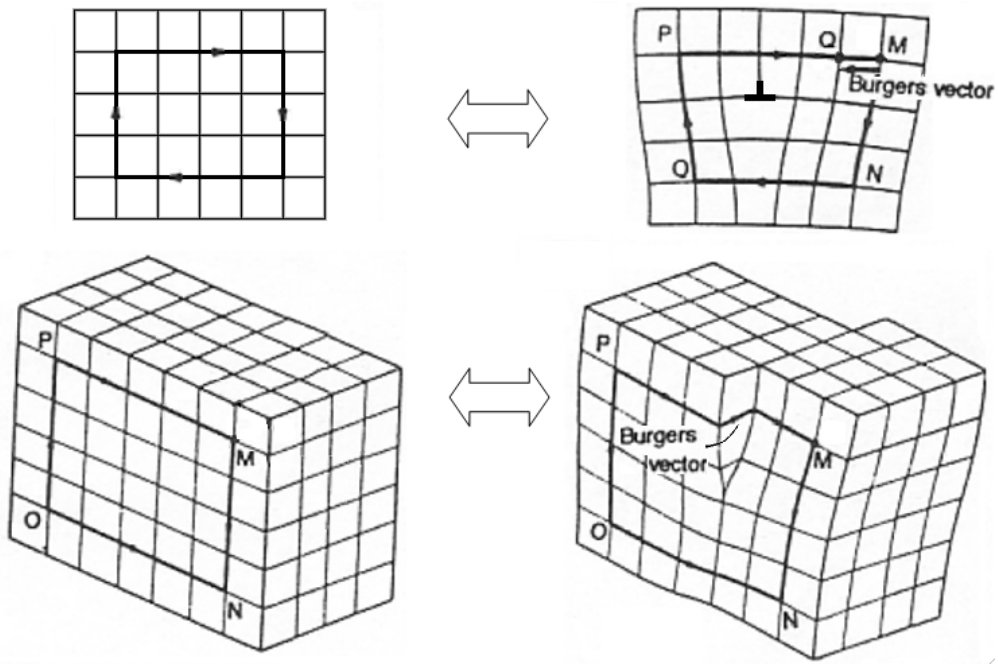

Figure 2.3: Edge (top) and screw (bottom) dislocation. The difference in the circulation integral between a crystal without a dislocation (left) and a crystal hosting a dislocation (right) is the Burgers vector characterizing the dislocation. The Burgers vector is parallel to a screw line and perpendicular to an edge line and parallel to the direction of motion of an edge line. For more info go to http://en.wikipedia.org/wiki/Dislocation . Image taken from wikipedia.org under the GNU Free Documentation License, http://en.wikipedia.org/wiki/GNU_Free_Documentation_License .

In this new picture of plasticity, dislocations are carrying the elementary discrete amounts of slip. Crystal deformation takes place in an inhomogenous-in-space and intermittent-in-time manner a direct effect of the discreteness of the dislocations. When a crystal is deformed the dislocations are found to be moving in a collective fashion exhibiting long-range correlations in space and in time. What is more, one can observe slip avalanches spanning several orders of magnitude in size distributed according to a power law.

Dimiduk et al. [4] used ultrahigh displacement resolution nanoindentation systems (effectively nanoscale seismometers) to detect displacement events of pure metallic single micro-crystals. They found power law distributions of event sizes spanning several decades in slip size (Fig. 2.4). These observations strongly support the interpretation that dislocations, in slowly compressed micro-crystals, move collectively in avalanches.

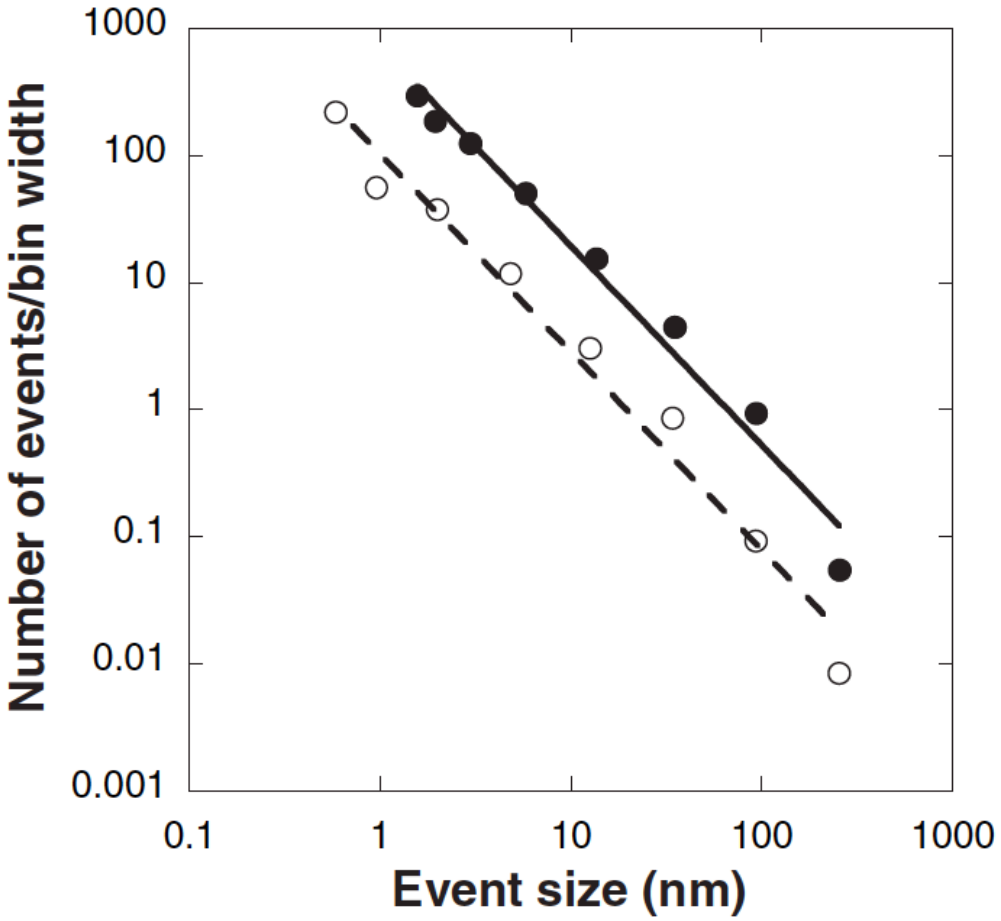

Figure 2.4: Power-law distribution of slip avalanche sizes, $S = \Delta\gamma$, from pure Ni samples with a fitted exponent $\kappa \approx 1.5 - 1.6$ (defined in Chapters 3 and 4). The figure is taken from the experimental paper by Dimiduk et al. [4], Scale-Free Intermittent Flow in Crystal Plasticity, D. M. Dimiduk, C. Woodward, R. LeSar, and M. D. Uchic, Science, 312(5777):1188-1190, 2006). Reprinted with permission from AAAS.

2.3 Material Flow as a Depinning Phase Transition

The substantial experimental evidence of power law distributed phenomena in deforming solids inspired a great deal of theoretical work. Several computational models can reproduce the experimental findings and reveal even more scale invariant, power-law distributed phenomena [1]. Discrete dislocation dynamics models [5, 6, 7, 8, 9, 10, 11], stochastic continuum models [6], phase field models [12, 13] and phase field crystal models [14] indicate that plastically deformed systems can operate near a non-equilibrium critical point [15].

Perhaps the most crucial finding came from Zaiser *et al.* who combined discrete dislocation dynamics coupled with extremal dynamics and automaton techniques [6]. They achieved a scaling collapse of the distribution of the slip avalanches at different external stresses below the flow stress. This collapse revealed that the slip avalanches grow bigger (and consequently span more decades) the closer the system approaches

to the flow stress (Fig. 2.5). The flow stress can be thought of as a non-equilibrium critical point separating two distinct phases: a low stress pinned phase where dislocations are stuck on average and the material is exhibiting plastic response and a high stress depinned phase where dislocations are mobile and the material is constantly flowing. In another study utilizing a stochastic continuum model Zaiser *et al.* [16] implemented a stochastic microstrain evolution model with similar success.

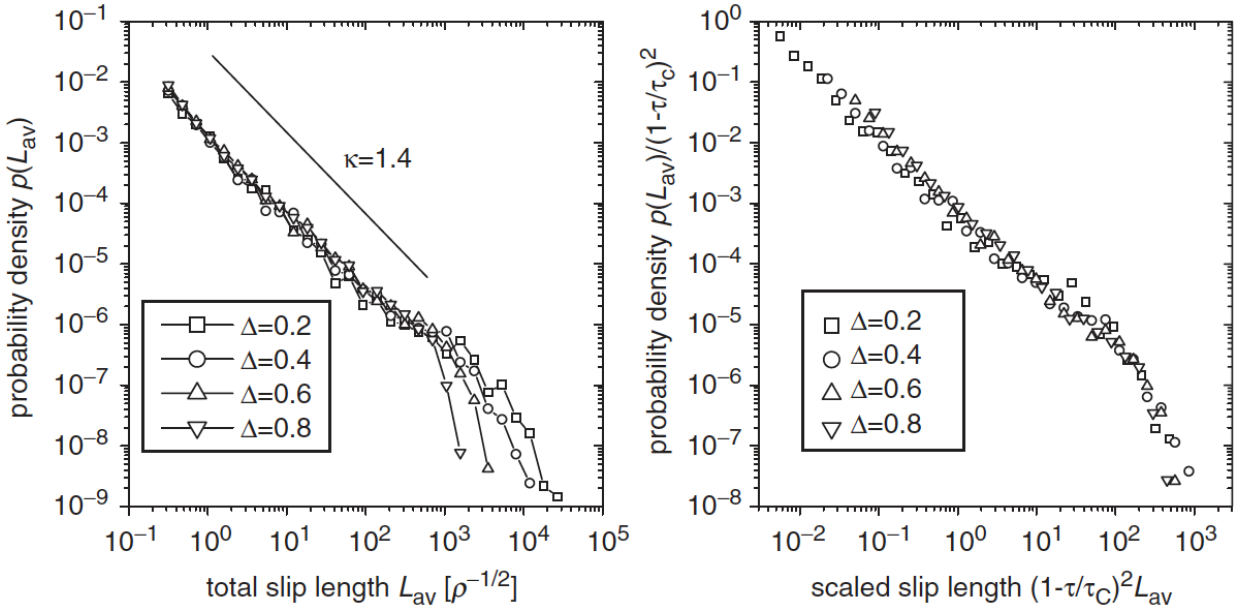

Figure 2.5: Distribution of slip avalanche sizes binned in stress, obtained using discrete dislocation dynamics (left) and collapse (right) by Zaiser et al. [6]. The fitted power law gives exponent $\kappa = 1.4$ and the collapse $1/\sigma = 2$. $\Delta = 1 - \tau/\tau_c$. and indicates the center of the window in stress for each curve. Both figures are in good agreement with our simulations (see Chapters 7 and 10 for our results, also Table 7.1). The figure is taken from Zaiser [1], Scale invariance in plastic flow of crystalline solids, M. Zaiser, Advances in Physics, 55(1):185-245, 2006, Taylor & Francis, reprinted by permission of the publisher (Taylor & Francis Ltd, http://www.tandfonline.com).

The approach to the critical point (which lies at the flow stress) happens in an intermittent manner through slip avalanches. A set of critical exponents and scaling functions that are expected to be material independent (universal) quantifies the non-equilibrium phase transition. In fact the majority of the up-to-date results indicate that dislocation systems fall into the universality class of the mean field interface depinning phase transition of an elastically moving interface in a disordered medium.

Although a single dislocation line can be thought of as an elastic line moving through a background of pinning centers (e.g. arrested or forested dislocations as they are often called) a collection of dislocations has been hard to deal with analytically. Therefore various kinds of computer simulations of the interacting dislocation network have been successfully employed to study plastic deformation as an interface depinning problem. In this work we employ a traditional discrete dislocation dynamics model and a modern phase field

crystal model. We successfully recover (and often times correct) previous computational results and reveal even more scaling laws all in agreement with the mean field interface depinning universality class.

Chapter 3

Experimental Evidence

3.1 Micro-pillar Deformation

Acoustic emission experiments on ice single crystals are one of the most trusted means of verifying the intermittent character of deformation since ice monocrystals or polycrystals can be easily grown in the laboratory. In addition, the transparency of ice permits the verification that the acoustic emission is not due to microcracking, and excellent coupling between ice sample and acoustic emission transducer can be achieved with fusion/freezing [17, 18, 19, 20, 5] [1].

The acoustic emission transducer picks up the acoustic emission signal, $V(t)$, at a sequence of discrete times t. It is made up of all the acoustic waves emitted by the moving dislocations in the deforming sample. The acoustic emission signal contains a continuous background due to slow dynamic phenomena such as grain boundaries bending, superimposed by fluctuations of all sizes. The fluctuations constitute slip avalanches which reveal the jerky character of plastic deformation.

Richeton *et al.* [17] analyzed the acoustic emission signal from hexagonal closed packed metallic single crystals (Cd and Zn-0.00%Al) and found a power law distribution of the acoustic emission energy of the slip events of

$$D(E) \sim E^{-1.5} \tag{3.1}$$

spanning 6 decades in acoustic emission energy defined as $E = \int_{\text{avalanche}} V(t)^2 dt$. They compressed metallic single crystals with the activated slip planes oriented at an angle to the compression direction.

In a similar work Miguel *et al.* [5] measured the acoustic emission signal of deforming ice single crystals.

[1] Several of the experimental works measure the peak amplitude of the signal during an avalanche in order to characterize an avalanche which may involve tedious mathematics to extract the scaling of its distribution. However the experiments we discuss explicitly in this chapter provide robust measurements of slip avalanche size and energy that can be easily compared to simulations and theory (see also Table 7.1).

They found a power law distribution of the slip events energy for over 6 decades

$$D(E) \sim E^{-1.6}. \tag{3.2}$$

Alternatively, Dimiduk *et al.* [4] used ultrahigh displacement resolution nanoindentation systems (effectively nanoscale seismometers) to detect displacement events of pure metallic single crystals. They measured the nominal displacement timeseries of the sample and extracted the displacement rate, $V'(t)$, via differentiation. They found a power law distribution of the slip event sizes of

$$D(S) \sim S'^{-(1.5\sim16)} \tag{3.3}$$

which extended for over 2 orders of magnitude is size $S' = \int_{\text{avalanche}} V'(t)dt = \Delta\gamma$ (Fig. 2.4).

3.2 Nano-pillar Deformation

The deformation of micro-sized pillars revealed slip avalanche statistics that matched well the collective dislocation behavior the models predict and they are in satisfactory agreement with the MFT of interface depinning (Chapter 5). But a question still remained: How small can a crystal be and still reveal such behavior? A manufacturing and testing challenge on its own.

In sub-micron-sized specimens there exist different dislocation creation mechanisms and their plastic response is difficult to study because of their tiny size (some maybe smaller than a human virus). There are 2 significant works we are going to discuss here that appeared recently in the literature.

Zaiser *et al.* [21] tested Mo (molybdenum, body center cubic (bcc) single crystal) nano-pillars down to 150nm in diameter and found power law avalanche size distribution

$$D(S') \sim S'^{-1.5}. \tag{3.4}$$

Brinckmann *et al.* [22] worked with Au (gold, face centered cubic (fcc) single crystals) and Mo nano-pillars down to 155nm in diameter and found the same result.

In all cases power law distributions of different measures of slip events spanning several decades were found, further documenting the collective dislocation motion in deforming crystals. Later in Chapter 7 we will show through our work that the results given in this Chapter are consistent with each other and in satisfactory agreement with the mean field theory of the interface depinning universality class (Table 7.1).

Chapter 4

Previous Computational Results

In the effort to understand better the phenomenon of plasticity as an interface depinning problem, several theoretical models were built and implemented drawing from the significant experimental works. Continuum models [6], discrete dislocation dynamics (DDD) models [5, 6, 7, 8, 11, 9, 10], phase field (PF) models [12, 13] and phase field crystal models [14] can reproduce the experimental findings and reveal even more scale invariant, power-law distributed phenomena. For our work we relied on traditional discrete dislocation dynamics (we explain the DDD model in Chapter 6) and were able to extract even more scaling laws (Chapters 7 and 8) and tested a phase field crystal (PFC)model (we present the PFC model in Chapter 9) for plasticity avalanches that are power-law distributed (Chapters 10). Here we discuss computational results from the literature from the point of view that plastically deformed systems can operate near a non-equilibrium critical point [15] [1].

4.1 Stochastic Continuum Models

Existing continuum models can be adapted to include stochastic fluctuations in their local stress-strain dependence phenomenologically in an effort to incorporate the disorder inherent in plastically deformed systems that gives rise to the power law collective behavior. These models describe plasticity at a mesoscopic scale above the microscopic scale of the individual dislocations but smaller than the macroscopic dimensions of the material. The spatial inhomogeneity of the crystal is introduced into these models by making the local yield stress random in space and strain.

Zaiser *et al.* [16] implemented a microstrain evolution model which included random stress fluctuations in space and in strain and was able to recover power law avalanche statistics, binned-in-stress (Fig. 2.5) and integrated-in-stress. More specifically they showed that the avalanche size distribution at stress τ scales as,

$$D(S') \sim S'^{-1.4} f\left(S'\left(1-\frac{\tau}{\tau_c}\right)^2\right) \tag{4.1}$$

[1] Similar behavior has been discovered in magnetic systems [15] and turbulence [23].

and its integrated-in-stress form scales as,

$$D_{\text{int}}(S') \sim S'^{-1.4-\frac{1}{2}} \sim S'^{-1.9}. \tag{4.2}$$

Here $S' = \Delta\gamma$, the strain increment in a slip avalanche and f a generic universal scaling function. The two previous scaling expressions are consistent with each other and in close agreement with the results of the MFT of interface depinning. The MFT of interface depinning is presented in Chapter 5 where we also define the universal scaling exponents and function shown.

In the same work and with the same microstrain evolution model, Zaiser *et al.* [16], also revealed the effect of work hardening by allowing the dislocation density to depend on with strain essentially introducing dislocation creation and annihilation. More specifically they made the root-mean-square of the local stress fluctuations to grow proportionally with the square root of the dislocation density, which in turn causes the local stress fluctuations to increase with strain. The maximum slip avalanche is dictated by the hardening coefficient $\theta \sim d\tau/d\gamma$

$$D(S') \sim S'^{-1.4} f(S'\theta) \tag{4.3}$$

4.2 Discrete Dislocation Dynamics Models

In one of the first works of Miguel *et al.* [7], a discrete dislocation dynamics (DDD) in 2 dimensions was utilized where a collection of interacting (parallel, straight, edge) dislocations was allowed to slip, driven by their long-range interaction and a uniform external stress. They successfully showed the Andrade power-law creep under constant external stress for a stress above the yield stress but below the flow stress (and constant temperature)

$$\gamma \sim t^{1/3} \tag{4.4}$$

from the strain rate decay with time as $d\gamma/dt \sim t^{-2/3}$. The strain rate is defined as $d\gamma/dt = V'(t) = \sum_{i=\text{all dislocations}} b_i v_i(t)$. Here v_i is the velocity of a dislocation and b_i its Burger's vector. They also managed to extract a power-law distribution of avalanche sizes (defined as $S^* = \sum_{i,\text{avalanche}} V^*(t_i)$ where $V^*(t) = \sum_{i=\text{mobile}} |v_i(t)|$ is the instantaneous collective speed of the mobile dislocations in an avalanche)

with a power-law exponent of 1.6,

$$D(S^*) \sim S^{*-1.6}. \tag{4.5}$$

In a later publication based on the same model Miguel *et al.* [24] showed that Andrade power-law creep of $\gamma \sim t^{1/3}$ can also be observed at initial times with an external applied stress above the flow stress (and constant temperature). The Andrade creep turned into linear creep, $\gamma \sim t$, at large times (the dislocations flowed constantly). The crossover time decreased for higher dislocation creation and/or higher temperature. For external stresses below the yield stress they saw the strain rate approaching zero and the dislocations jamming. However they got

$$\left\langle \frac{d\gamma}{dt} \right\rangle \sim (\tau - \tau_c)^{1.8}, \tag{4.6}$$

as the external stress, τ, moves from below to above the critical stress, τ_c (where the system changes from the pinned to the depinned phase). This means that the depinning exponent they obtained, $\beta \approx 1.8$, a value that differs substantially from the mean field theory of interface depinning (Chapter 5). In Chapter 7 we perform a careful measurement of β which gives the MF value of $\beta \approx 1$. In Miguel *et al.* [5] (again 2d DDD) the authors calculated the distribution of the avalanche energies, $E^* = \int_{\text{avalanche}} V^*(t)^2 dt$ ($V^*(t) = \sum_{i=\text{mobile}} |v_i(t)|$), to follow a power law of,

$$D(E^*) \sim E^{*-1.8} \tag{4.7}$$

which compared well with acoustic emission experiments on ice (same work), $D(E) \sim E^{-1.6}$ with $E = \int_{\text{avalanche}} V^2(t) dt$.

Laurson and Alava [8] extracted the temporal avalanche speed profiles, power spectra and average avalanche sizes versus their duration above the flow stress but with exponents that disagree with MF interface depinning. In their calculation of average avalanche profiles, an exponent of 1.5 was assumed,

$$V(t) = {t_{\text{aval}}}^{1.5} f(t/t_{\text{aval}}) \tag{4.8}$$

and then all avalanches of similar duration t_{aval} were averaged. Here f is a universal scaling function, that is predicted to be a parabola in MFT. In the resulting plot the avalanche profiles appeared to overlap although in a proper scaling collapse one varies the exponent until the average profiles of different durations overlap.

The best collapse gives the scaling exponent. The authors then proceeded to extract power spectra

$$PS(\omega) = \omega^{-1.5} \tag{4.9}$$

and average avalanche sizes versus their duration

$$\langle S \rangle = {t_{\text{aval}}}^{1.5} \tag{4.10}$$

that gave the same apparent exponent. They work exclusively above the critical stress where in general the individual avalanches tend to merge together and their resulting shape may be distorted from the pure single avalanche shape and may not be amenable to a collapse. Their exponents disagree with MFT. We perform a proper scaling collapse of the avalanche profiles (and define the above scaling exponents and function) in Chapter 7 and show that it is in agreement with the power spectra of the collective speed of the dislocations both above and below the critical stress. Our results indicated that the power spectra and the temporal avalanche speed profiles are consistent with the MF interface depinning universality class.

Zaiser *et al.* [6] achieved a scaling collapse of the distribution of the slip avalanches at different external stresses below the flow stress,

$$D(S') \sim S'^{-1.4} f\left(S' \left(1 - \frac{\tau}{\tau_c} \right)^2 \right) \tag{4.11}$$

($S' = \int_{\text{avalanche}} V'(t)dt = \Delta\gamma$, $V'(t) = \sum b_i v_i(t) = d\gamma/dt$) combining discrete dislocation dynamics coupled with extremal dynamics and automaton techniques (as we already discussed in Section 2.3 and showed in Fig. 2.5). Their work convincingly shows that a correlation length can be defined, which diverges as the system approaches the critical point. Therefore plastically deformed systems can be thought of as depinning systems.

Finally, Csikor *et al.* [11] undertook the immense effort to build a 3 dimensional DDD with both edge and screw dislocations segments to extract the full avalanche size distribution, meaning power law and cutoff exponents and the scaling function,

$$D(S') \propto S'^{-1.5} \exp(-(S'/S'_0)^2) \tag{4.12}$$

Both critical exponents and the scaling function are in agreement with the mean field interface depinning universality class (Chapter 5). Here S'_0 is the maximum avalanche size up to which the power law distribution

extends (a similar definition we discuss in Chapter 7).

4.3 Phase Field Models

Koslowski *et al.* [12, 13] introduced a phase field model to describe the dislocation configurations in a disordered slip plane. It accurately describes single crystals that are isotropic and experience single slip deformation. The evolution of the dislocation configurations is described through an integer-valued phase field. The model incorporates in an energy functional the dislocation interaction, the effect of an externally applied stress and also accounts for the dislocation core energy. The dynamics are determined through minimization of a work functional which besides the dislocation energy includes a dissipative interaction with the quenched disorder representing forest dislocations. The model needs no extra creation and annihilation conditions to be supplied as in the DDD models. The phase field keeps track of the dislocation number in space through the amount of slip; slip at a point increases (decreases) by +1 (in units of a Burgers' vector) when a dislocation crosses that point with a positive (negative) velocity. During external loading the dislocations are forced to move through the disordered landscape bowing at the pinning centers until they get depinned leading to slip avalanches.

The phase field model with quenched disorder was able to reproduce the avalanche behavior of plastically deforming crystals. As the external stress is increased adiabatically slowly the system responds with larger and larger slip events that follow a power of about 2 decades,

$$D(A) \sim A^{-1.8} \tag{4.13}$$

where $A = \max_{t \in \text{avalanche}}\{V(t)\}$ of the acoustic emission signal $V(t) = \sum_{i=\text{all dislocations}} |v_i(t)|$. This value is in rough agreement with the literature but logarithmic binning could improve the result and a scaling collapse of the avalanche distributions at different stresses could even reveal the full distribution of slip avalanches (i.e. critical exponents and scaling function). Finally characterizing the slip avalanches by their size S or energy E (as defined for example above or in Chapter 7) would make it easier to compare critical exponents and scaling functions with the theory of interface depinning.

4.4 Discussion

The discrete dislocation dynamics models describe plasticity at a microscopic level. They constitute the most straight-forward approach. Plastic deformation is directly produced by the motion of the individual

dislocations. Microstrain evolution models are stochastic continuum plasticity models. Plastic deformation is expressed in terms of the evolution of a continuous plastic strain field. The effect of the dislocation dynamics is introduced by adding microstructural heterogeneity and randomness to the equations of the strain field phenomenologically (the models still maintain their homogeneity at macroscopic scales). Phase-field models lie at an intermediate scale between the other two. Plastic deformation is described by a strain field. The strain field is resolved on a microscopic scale and dislocations appear as localized gradients of that field. However, in order to observe metastable dislocation configurations, quenched disorder needs to be introduced in both the continuum and the phase field models. This is different from the discrete dislocation dynamics models (ours is defined in Chapter 6) and the phase field crystal model (defined in Chapter 9) where self-pinning due to the long-range dislocation interaction is already included.

The models discussed so far, with or without quenched disorder, indicate that the static properties of plasticity fall into the universality class of the mean field version of the depinning phase transition of an elastically moving interface in a disordered medium [1]. In Chapter 5 we elaborate on the interface depinning model and present its mean field theory. In Chapter 7 we show our results from a DDD model and in Chapter 10 we discuss our results from our PFC model. We extract a wealth of universal (i.e. material independent) critical exponents and scaling functions providing several new findings and correcting the literature. Our work shows that the dynamics of plasticity belong to the mean field interface depinning universality class. The reader that cannot wait can just turn to Table 7.1 where all of our results are presented side-by-side with experimental and computational results from the literature and the mean field theory of interface depinning.

Chapter 5

Interface Depinning

5.1 A general model of Interface Depinning

[1]Let us first give here a generic simple model which describes an interface driven by an externally applied force through a disordered medium. The interface has configurations that are on average stuck if the driving force is below a critical value. The interface is moving constantly if the force is above the critical value. Examples of such interface depinning problems include fluid invasion in porous media [26, 27], magnetic wall depinning [28, 29, 30], charged density waves driven by electric fields [31, 32, 33, 34, 35, 36, 37].

The interface can be visualized as a line, which lies on a 2-dimensional plane (x, y), and can be driven by a uniform force $\vec{F} = |\vec{F}|\hat{x}$. Assuming small deviations from the straight line its configuration can by represented by the displacement field $u(y)$ away from a reference straight line along the y direction perpendicular to the x direction. In the following we assume that the interface is self-affine, i.e. without overhangs [38, 39]. In many interface depinning systems inertia does not play a significant role since many systems are overdamped, i.e. the dynamics of the interface are purely dissipative. To lowest order in deviations from flat, i.e. for small $u(y)$, we have the following equation of motion [25],

$$\eta \frac{\partial u(y,t)}{\partial t} = F + \sigma(y,t) - f_p[y] \tag{5.1}$$

where η is the viscosity of the medium, f_p the force from the randomly distributed pinning centers and

$$\sigma(y,t) = \int dt' \int dy' J(y-y', t-t')[u(y',t') - u(y,t)] \tag{5.2}$$

is the self-stress on the interface, meaning the stress on a specific segment from the rest of segments of the interface. Elastic interactions along the interface (for example surface tension) preserve its straightness and

[1]For this Chapter on the MFT of interface depinning we found particularly elucidating Fisher's notes [25] and Zaiser's review [1].

that can be modeled through $J(y-y',t-t')$ as,

$$J(y-y',t-t') \propto \delta(t-t')\nabla^2\delta(y-y') \tag{5.3}$$

In monotonic models

$$J(y,t) \geq 0 \ \text{ for all } \ y,t \tag{5.4}$$

and a configuration that is initially ahead of another will always be ahead as the interface is driven by F. Middleton [40] has shown that Eq. (5.4) implies that pinned (not moving) ($F < F_c$) and constantly moving ($F > F_c$) solutions cannot coexist at the same driving force F. Therefore, the critical force, F_c, is unique and well defined for monotonic models.

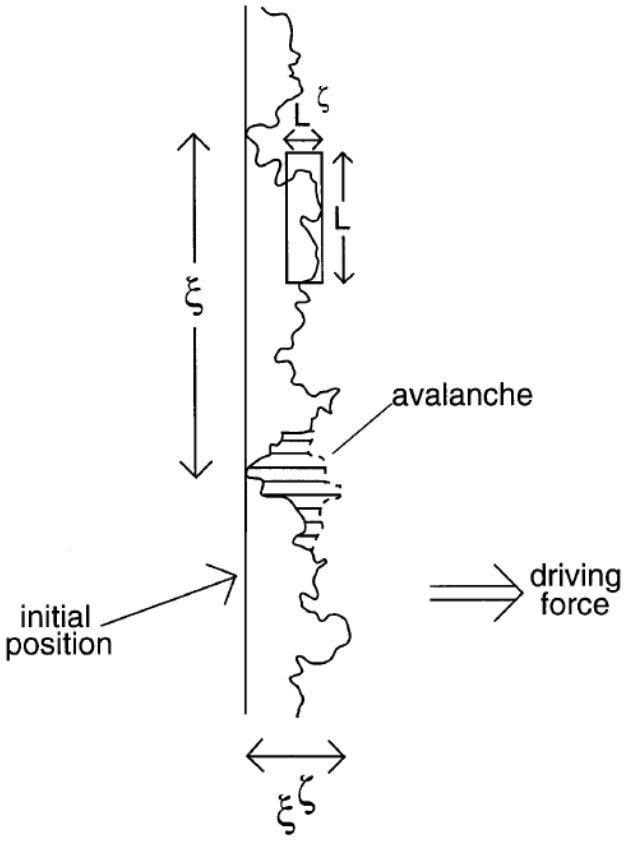

Figure 5.1: A generic model of an interface depinning through a background of pinning centers. Taken from Fisher [25]. Reprinted from Physics Reports, 301, D. S. Fisher, Collective transport in random media: from superconductors to earthquakes, 113-150, Copyright (1998), with permission from Elsevier.

5.1.1 Scaling Expressions

This problem has been studied as a non-equilibirum critical phenomenon [41, 38, 35, 40, 25]. F_c sits between two phases: a pinned (stuck) phase for $F < F_c$ and a moving phase for $F > F_c$. $\langle V \rangle = \langle d(\langle x \rangle + u(y))/dt \rangle$ is the mean velocity of the interface and the average $\langle ... \rangle$ is over all y on the interface. Then $\langle V \rangle > 0$ for $F > F_c$ and $\langle V \rangle = 0$ for $F < F_c$. In analogy to equilibrium phase transition theory a correlation length, ξ, can be defined that has been shown to scale in the same way above and below the critical point [25]

$$\xi \sim |F_c - F|^{-\nu} \tag{5.5}$$

i.e. ξ diverges near the critical point. Eq. (5.5) defines the critical exponent ν. Middleton also showed that the depinning transition at F_c is continuous rather than a first order transition [40]. The average velocity $\langle V \rangle$ at which the interface moves is zero below the critical point and scales with the depinning exponent β above it,

$$\langle V \rangle \sim \begin{cases} 0 & F < F_c \\ (F - F_c)^{\beta} & F > F_c \end{cases} \tag{5.6}$$

For forces well above the critical force, $F >> F_c$, where the system is outside the critical region, the disorder becomes less important and the mean velocity increases linearly with stress.

The interface becomes self-affine as it proceeds through the disordered medium (Fig. 5.1). In other words the transformation $y \to \lambda y, u \to \lambda^{\zeta} u$, where λ is a positive constant and ζ the roughness exponent, leaves it statistically invariant [1],

$$\big\langle |u(y) - u(y + l)| \big\rangle \sim l^{\zeta} f_u(l/\xi) \tag{5.7}$$

Here the scaling function $f_u(w << 1) = 1$ and $f_u(w >> 1) = w^{-\zeta}$ according to the Family–Vicsek scaling [42]. The height-height correlation in Eq. (5.7) exhibits a power law with the separation, l^{ζ} for $l < \xi$ and turns into a constant ξ^{ζ} for $l > \xi$.

The interface proceeds with avalanches as some segments advance rapidly through the disordered landscape before they get pinned again. Below the critical force and for an external force increased adiabatically (or quasi-statically) slowly the interface will be pinned at the local energy minima (metastable configurations) and will proceed with distinct avalanches in between. These avalanches distribute themselves according to

a power law with a maximum size $S_{\max}$,

$$D_S(S, F_c - F) \sim S^{-\kappa} f_S(S/S_{\max}) \tag{5.8}$$

where

$$S_{\max} \sim (F_c - F)^{-\frac{1}{\sigma}} \tag{5.9}$$

and the universal scaling function $f_S(w \to 0) \to 1$ and $f_S(w \to \infty) \to 0$.

In the critical region (i.e. for F close enough to F_c) the interface advances incrementally with avalanches (Fig. 5.1). The time t it takes the interface to proceed locally over a distance l (which is essentially the linear size of an avalanche, a valid assumption in isotropic problems) is related to that distance through the dynamic exponent z [1],

$$t \sim l^z. \tag{5.10}$$

5.1.2 Exponent Relations

The mean velocity of the interface can be expressed as the distance traveled over time

$$\langle V \rangle \sim \frac{x}{t} \sim \frac{\xi^\zeta}{\xi^z} \sim (F - F_c)^{-\nu(\zeta - z)}. \tag{5.11}$$

Together with $\langle V \rangle \sim (F - F_c)^\beta$ this gives us the first exponent relation

$$\beta = \nu(z - \zeta) \tag{5.12}$$

The mean avalanche size is the mean distance travelled by the interface over some (adiabatically) small increase in the applied force [2] [1]

$$\langle S \rangle \sim \frac{\xi^\zeta}{|F_c - F|} \sim \frac{\xi^\zeta}{\xi^{-1/\nu}} \sim \xi^{\frac{1+\nu\zeta}{\nu}} \sim |F_c - F|^{-(1+\nu\zeta)} \tag{5.13}$$

In the general case of a d-dimensional interface moving in $(d+1)$-dimensional space (in this example $d = 1$)

[2] It is in general more straightforward to define and extract avalanches below F_c (for an example see Chapter 7). Special care may be necessary for the fluctuations above F_c, for an example see Chapter 10.

the maximum avalanche scales as (e.g. see Fig. 5.1)

$$S_{\max} \sim \xi^d \times \xi^\zeta \sim |F_c - F|^{-\nu(d+\zeta)}. \tag{5.14}$$

The mean avalanche size relates to the maximum as

$$\begin{aligned}
\langle S \rangle &\sim \int_0^{S_{\max}} S D(S) dS && (5.15)\\
&\sim \int_0^{S_{\max}} S^{1-\kappa} f_S(S/S_{\max}) dS && (5.16)\\
&\sim S_{\max}^{2-\kappa} \int_0^1 (S/S_{\max})^{1-\kappa} f_S(S/S_{\max}) d(S/S_{\max}) && (5.17)\\
&\sim S_{\max}^{2-\kappa} && (5.18)\\
&\sim |F_c - F|^{-(2-\kappa)\nu(d+\zeta)} && (5.19)
\end{aligned}$$

Combining the above Eq. (5.13) with Eq. (5.19) we have the scaling relations

$$\kappa = 2 - \frac{1 + \nu\zeta}{\nu(d+\zeta)} \tag{5.20}$$

while combining Eq. (5.9) with Eq. (5.14) we arrive at the following scaling relation

$$\frac{1}{\sigma} = \nu(d+\zeta). \tag{5.21}$$

5.2 Mean Field Theory of Interface Depinning

In mean field theory (MFT) all spatial information of the interaction is neglected and constant interactions between all segments of the interface are assumed. Using renormalization tools this approximation has been shown to give the exact values for the critical scaling exponents and scaling functions for all dimensions above the upper critical dimension. The upper critical dimension and consequently the applicability of MFT is ultimately determined by the long wavelength behavior of the interaction. In the general case

$$\int dt J(\vec{r}, t) \sim r^{-d-\tilde{\Gamma}} \tag{5.22}$$

with a Fourier transform that scales in the static limit as [25]

$$\tilde{J}(\vec{k}, \omega = 0) \sim |\vec{k}|^{\tilde{\Gamma}} \tag{5.23}$$

The upper critical dimension d_c is then given by

$$d_c(\Gamma) = 2\Gamma \;\text{ with }\; \Gamma = \min[\tilde{\Gamma}, 2] \tag{5.24}$$

and the MF critical exponents and scaling functions are exactly correct for dimensions $d > d_c(\Gamma)$.

In MFT the velocity force relationship becomes linear even close to the critical point and the depinning exponent $\beta_{\rm MF}$ is unity,

$$\langle V \rangle \sim (F - F_c)^{\beta_{\rm MF}} \;\text{ for }\; F > F_c \;\text{ with }\; \beta_{\rm MF} = 1 \tag{5.25}$$

The rest of the fundamental exponents in MFT are compiled in the following Table 5.1 [3]. Also the avalanche

exponent	MF value
$\beta_{\rm MF}$	1
$\nu_{\rm MF}$	$\frac{2}{d_c}$
$\zeta_{\rm MF}$	0
$\kappa_{\rm MF}$	$\frac{3}{2}$
$\sigma_{\rm MF}$	$\frac{1}{2}$

Table 5.1: Table of MF exponents of the interface depinning universality class.

size distribution scaling function takes the form of an exponential.

All the critical exponents characterizing the interface depinning universality class depend on the dimension of the elastic manifold, the power-law decay of the interaction if it is long range and on the type of dynamics but not on other details of the system. On the other hand the critical force or the proportionality coefficients will in general depend on the details and thus will be non-universal.

5.3 A simple Mean Field Theory Model for Plastic Deformation of Solids

A more specific daughter model to the generic interface depinning discussed above was synthesized to include dynamic weakening effects seen in plastic deformation of solids [44]. It gives universal predictions for stress-strain curves and avalanche statistics in all three cases of deformation: brittle behavior (positive weakening), ductile behavior (zero weakening) and hardening (negative weakening).

The model assumes that a slowly sheared material has weak spots (labeled with r) where slip initiates

[3] These exponents are calculated also by Functional Renormalization Group ϵ-expansion to second order by Fisher [25], Nattermann et al. [41], Leschhorn et al. [43].

when the local stress exceeds a random local failure stress $\tau_{s,r}$. A failed spot r slips until the local stress is reduced to some random arrest stress $\tau_{a,r}$, and then re-sticks. Such a local slip event can trigger other weak spots to slip, resulting in a slip avalanche. To model brittle materials after a spot has failed for the first time its failure stress will be weakened to a diminished value $\tau_{d,r}$ with $\tau_{a,r} < \tau_{d,r} < \tau_{s,r}$ and it stays at the diminished value for the remainder of the slip avalanche. The amount of weakening is parametrized by

$$\epsilon = \frac{\tau_{s,r} - \tau_{d,r}}{\tau_{s,r} - \tau_{a,r}} > 0 \tag{5.26}$$

At the end of an avalanche all failure stresses return to their initial static failure stresses. In contrast, in order to model hardening behavior each spot's failure stress is increased by an amount proportional to $|\epsilon|/N$ (can be defined differently, see [1] and/or Chapter 2)

$$\tau_{s,r} \to \Big(1 + \frac{|\epsilon|}{N}\Big)\tau_{s,r} \tag{5.27}$$

where N is the volume of the system or the total number of spots in the discrete model.

In all three cases of plastic deformation modeled above the elastic interactions between slipping sites ($J(\vec{r})$) are so long range that the upper critical dimension is lower than the dimension of the system (see Eq. (5.24)). In that case the interactions can be approximated by infinite range interactions and the MFT of interface depinning will give exact results for the universal scaling behavior on long length scales in all dimensions [44, 45]. For example in MFT it possible to analytically solve for the probability density distribution $D(S, \tau)$ of slip-avalanche sizes S, at applied stress τ (see Eq. (5.8)). Here, the slip size S is given by the total strain increase during a slip avalanche.

5.4 Proposed Thermal Rounding of the Depinning Transition of Plasticity

At zero temperature there is no thermally induced dislocation creep. Dislocations are pinned below the critical stress and flow above it. The mean dislocation speed is zero below, and continuously increases to non-zero values above the critical stress with a discontinuous jump in its first derivative with respect to the applied stress. For non-zero temperatures thermal dislocation creep is induced. This causes the dislocations to flow at any positive stress, even though the external stress may be below its zero-temperature critical value. The critical point is located where the zero-temperature curve, $\langle V \rangle(F)$, has a sharp discontinuity in its first derivative (where the arrow points in Fig. 5.2). The higher the temperature the larger the velocity

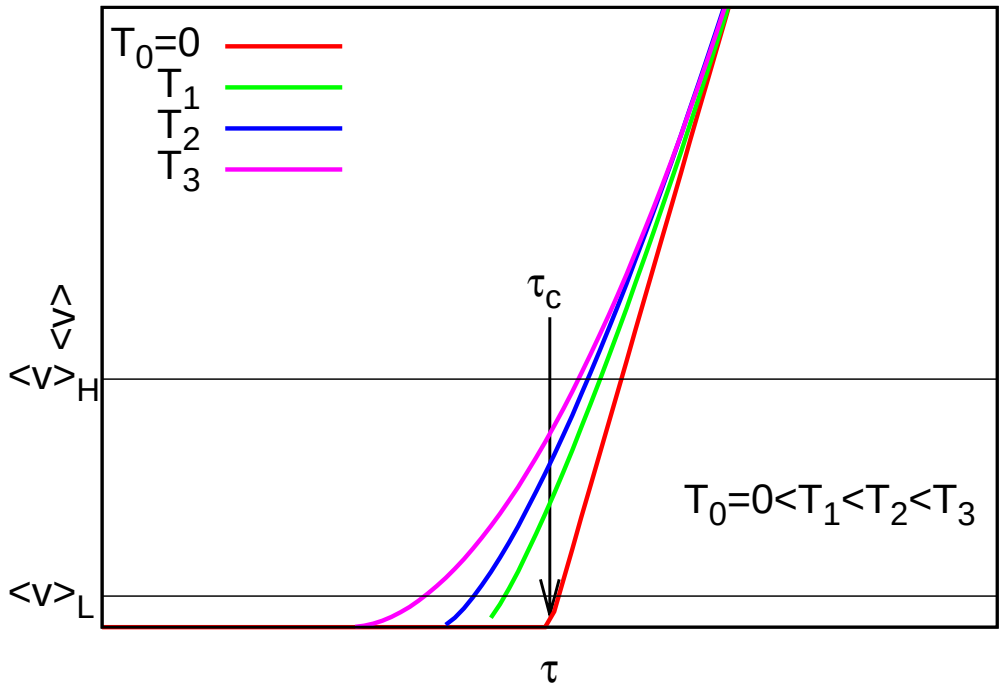

Figure 5.2: (color online) The proposed behavior of the strain rate, $\langle V \rangle$, of the depinning phase transition of plasticity due to temperature. In this schematic the thermal rounding of the transition is illustrated. The behavior is expected to be similar to the temperature effect on the depinning of charge-density waves as studied by Middleton [37] or Roters et al. [29]. Figure courtesy of Thomas Fehm.

at the critical stress as it is illustrated in Fig. 5.2.

One can impose a fixed shearing rate instead of controlling the applied shear stress on a deforming body. The system can operate in a steady flowing state for different temperatures. Systems that operate closer to the zero-temperature critical point will exhibit longer correlation lengths and distributions of slip avalanches with more decades of power law scaling, i.e. with larger maximum (cutoff) avalanche sizes $S_{\max}$. More specifically, for low enough shearing rate ($v_0 = \langle v \rangle_{\mathrm{L}}$ in Fig. 5.2) the lower temperature can be closer to the critical point. For high enough shearing rate ($v_0 = \langle v \rangle_{\mathrm{H}}$ in Fig. 5.2) the situation is reversed and the higher temperature is closer to the critical point (meaning, it has a larger associated correlation length).

In summary at zero temperature the pinning-depinning transition is sharp and the critical point clearly separates the pinned phase ($\tau < \tau_c$) from the depinned phase ($\tau > \tau_c$). At nonzero temperatures the transition becomes rounded. This effect is illustrated in the relationship of the shear strain rate with the external stress:

$$\langle V \rangle \sim T^{\delta} \tag{5.28}$$

and schematically depicted in Fig. 5.2. Here T is the temperature and δ the temperature or thermal critical

exponent (defined through this scaling expression). This behavior is analogous to the temperature effect on the depinning of charge-density waves as studied by Middleton [37] or Roters et al. [29].

5.5 Jamming-Unjamming vs Pinning-Depinning

A clarification is in order at this point. The dislocation system is jammed below a critical value of the external stress. Applying a constant external stress above the critical (flow) stress allows the system to flow, and the dislocations are unjammed. It is important to stress that in the glide plane of the dislocations, there is effectively no external pinning potential (i.e. no quenched disorder) [4], so that the jamming is an emergent phenomenon. However, recent work has shown that the behavior of the transition appears to be in the universality class of the interface pinning-depinning transition [6], as if there was an effective external pinning potential induced by the collective interactions between the dislocations. The dislocations can be thought of as pinned (stuck) below a critical value of the external stress. The dislocations get depinned (mobile) when a constant external stress above the critical (flow) stress is applied. Henceforth, in this Thesis we will use the two terms interchangeably without abiding to their strict definition since they effectively describe the same phases of the dislocation system and plastic deformation.

[4] Here we are describing the setup of the DDD model. However there is no quenched disorder in the PFC model either.

Chapter 6

The Model @ T=0 (DDD)

6.1 Discrete Dislocation Dynamics

In our effort to investigate plasticity, we have implemented a model that presents a straight-forward approach to the problem: discrete dislocation dynamics. As we will see below the interaction between the dislocations is long range. For that reason we expect DDD to give results according to the MFT of interface depinning (see next Chapter 7).

In a square box of side length L we place N straight edge dislocations parallel to the z-axis. They are allowed to move continuously along the x-axis, our shear direction. Their y position is fixed at consecutive integer values simulating parallel slip planes separated by integer multiples of the lattice constant. In that way we simulate materials with strong plastic anisotropy that deform by glide on a single plane, like ice [5]. Due to high plastic anisotropy dislocation climb is negligible in such systems, while the temperature is not high enough to active considerable dislocation motion by climb. The problem is effectively two-dimensional and it has been shown to have the same scaling behavior in three dimensions [5, 8, 6, 11, 9].

The shear stress produced by an edge dislocation with Burgers vector $\vec{b} = (b, 0)$ at a distance $\vec{r} = (x, y)$ in the host medium is (from linear elasticity theory):

$$\tau_{\rm int}(\vec{r}) = \frac{b\mu}{2\pi(1-\nu)} \frac{x(x^2-y^2)}{(x^2+y^2)^2} \tag{6.1}$$

$$= \frac{b\mu}{2\pi(1-\nu)} \frac{\cos(\theta)\cos(2\theta)}{r}. \tag{6.2}$$

It is anisotropic in the (x,y)-plane and for large $r = \sqrt{x^2+y^2}$ decays as $\tau_{\rm int} \sim 1/r$ as it is shown in Fig. 6.1. Here μ is the shear modulus and ν is the Poisson ratio of the host medium [3]. Each dislocation moves in response to the interaction stress from the rest, $\tau_{\rm int}$, and the external shear stress, $\tau_{\rm ext}$. Their stick-slip

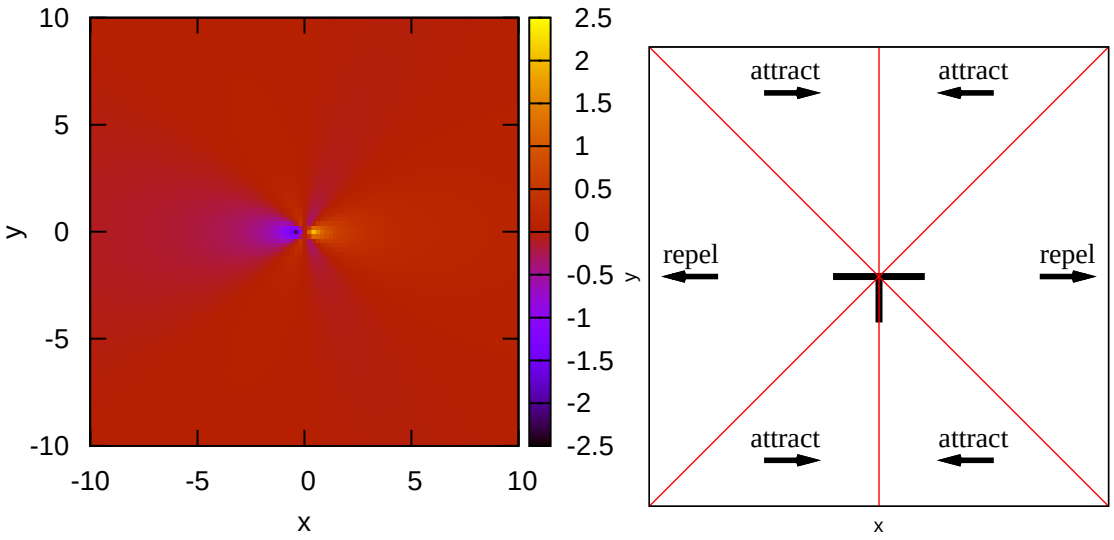

Figure 6.1: (color online) The shear stress field of an edge dislocation (located at the origin) as mediated by the medium is long-range and anisotropic. Exact functional form plotted on the left, schematic of anisotropy on the right.

motion can be described by overdamped equations of motion (without inertia):

$$\eta \frac{dx_i}{dt} = b_i \left(\sum_{j \neq i}^{N} \tau_{\rm int}(\vec{r}_j - \vec{r}_i) + \tau_{\rm ext} \right) \tag{6.3}$$

for $i, j = 1, ..., N$ where x_i is the x coordinate of the ith dislocation at point $\vec{r}_i$ with Burgers vector b_i, $\vec{r}_j$ with $j \neq i$ are the coordinates of the other $N-1$ dislocations, t is time and η is the effective viscosity in the host medium [5, 8, 6].

In our computer simulations we impose periodic boundary conditions in both x and y directions in order to simulate materials that are bigger than our basic simulation cell and avoid edge effects. To treat the long-range character of the dislocation interaction and avoid edge effects, we found the Lekner summation method [46] particularly straight forward and useful. According to that method, we introduce an infinite number of image cells around the basic simulation cell. Each one of the image cells contains an image dislocation for each one of the N dislocations in the basic cell at the same relative position. The image dislocations follow exactly the motion of the N dislocations in the basic cell. The total stress between a pair of dislocations, i, j, of the basic cell includes now all their images [1],

$$\tau_{\rm int}(\vec{r_i} - \vec{r_j}) = b_j \sum_{\text{all images}} \frac{(x_i - x_j)((x_i - x_j)^2 - (y_i - y_j)^2)}{((x_i - x_j)^2 + (y_i - y_j)^2)^2} \tag{6.4}$$

[1] For all the details on how we derived the stress interaction applying the Lekner summation method of images please see Appendix A.

$$= b_j \left[\frac{4\pi^2}{L} \sum_{l=-\infty}^{\infty} \sum_{m=1}^{+\infty} m(\chi_{i,j}+l)\cos(2\pi m\psi_{i,j}) e^{-2\pi|m(\chi_{i,j}+l)|} \right] \tag{6.5}$$

where

$$x_i - x_j = \chi_{i,j} L \qquad y_i - y_j = \psi_{i,j} L \qquad |\chi_{i,j}|, |\psi_{i,j}| < 1 \tag{6.6}$$

where $x_i - x_j$ ($y_i - y_j$) is the $x(y)$-distance between the dislocations i and j while the integers $l(m)$ count the images in the $x(y)$ direction. Since they both reside in the basic cell, their x(y)-distance is a less-than-one fraction $\chi_{i,j}(\psi_{i,j})$ of the linear size of the basic cell L. The calculation of the long-range interaction over all the images is the most time-consuming part of the simulation. In order to speed up the simulation we calculate the interaction for all possible pairs of distances with some resolution and place those values in a table. During runtime for a given pair of dislocations we find the interaction stress by interpolation [2].

The equations of motion are solved by the adaptive-step fifth-order Runge-Kutta method. During every time-step new positions are calculated in parallel for all dislocations in the basic cell. The method compares the new positions obtained with the fifth-order Runge-Kutta method to those obtained with the fourth-order Runge-Kutta method and accepts them if they are within the specified accuracy. Otherwise more accurate positions are calculated repeatedly until accuracy is reached, up to a maximum number of recalculations [47] [3].

We have set the temperature to $T = 0$, the distance scale to $b = 1$ and the time scale to $t_0 = \eta/(\mu/(2\pi(1-\nu)) = 1$. The dislocation number is constant, since for the time being, we considered neither dislocation creation nor annihilation[4] [5]. There are equal numbers of dislocations with positive, $\vec{b} = +\hat{x}$, and negative, $\vec{b} = -\hat{x}$, Burgers vectors, rendering the system 'neutral',

$$\sum_{i=1}^{N} b_i = 0. \tag{6.7}$$

Also, we are not allowing dislocation climb since it is negligible compared to the effect of glide in materials that exhibit power law statistics. It would only increase the computational complexity but not add to the

[2]For a detailed explanation of how we set up and implemented the "look-up" table please see Appendix A.

[3]The details of the Runge-Kutta we used can be found in [47].

[4]Having a constant number of dislocations should be particularly true for nanometer sized materials where prolific dislocation sources are scarce and exhibit minimal hardening as it is evident from the stress-strain curves in single crystal FCC nanopillars like Au [22] or Cu [48] and elucidated by the numerical work of Weinberger and Cai [49]. Friedman *et al.* [50] analyzed deformation avalanches from nano-scale samples and found it agrees with MFT as well.

[5]Dislocation creation and annihilation introduce strain-hardening to the system. More specifically by making the creation rate depend on the local (or external) stress the system would possess a non-constant critical stress that would increase with strain. In that case the size of the maximum avalanche would scale inversely with the strain-hardening coefficient [16, 51], which is analogous to the demagnetization factor in spin-systems [28].

physics we are probing[6]. When two dislocations on the same glide plane come very close ($1b$) they get pinned as they are not allowed to climb over each other. In that way we can still use linear elasticity theory for their interaction.

We define the dislocation collective speed (also called dislocation activity) $V(t)$, i.e. the sum of the absolute values of the velocities $|v_i(t)|$ of all the dislocations at each time to be,

$$V(t) = \sum_{i=1}^{N} |v_i(t)| \tag{6.8}$$

The acoustic emission signal is proportional to the dislocation collective speed. Thus their statistics should be similar. Another popular choice is

$$V'(t) = \sum_{i=1}^{N} b_i v_i(t) \propto \dot{\gamma}, \tag{6.9}$$

which is proportional to the strain rate [1].

[6]Dislocation climb is necessary for investigating pattern formation [52] but is not expected to change the scaling results we present in the next Chapter 7. Csikor et al. [11] implemented a full 3-dimensional DDD model with edge, screw and mixed dislocation segments that could glide in different slip planes and recover essentially the same avalanche size distribution scaling as in the 2-dimensional DDD models. (Their equations of motion are overdamped with inertia. The dislocations are allowed to form junctions and dislocations with opposite Burgers' vectors can annihilate. Edge dislocations are not allowed to climb but screw dislocations are allowed to cross-slip depending on temperature. The simulations are initialized with Frank-Read sources.)

Chapter 7

Results @ T=0 (DDD)

The interaction between two parallel straight edge dislocations is given by the shear stress element τ_{xy} of the elasticity tensor which scales as

$$\tau_{xy} \sim \frac{1}{r} \text{ for } r \to \infty \tag{7.1}$$

This means that the stress kernel is also long range,

$$\begin{aligned} \int d^d r J(r) &\sim \tau_{xy} \\ \int dr r^{d-1} J(r) &\sim \frac{1}{r} \\ J(r) &\sim r^{-d-1} \end{aligned} \tag{7.2}$$

Thinking of dislocation dynamics as an interface depinning problem we can determine an analogous upper critical dimension by seeing that

$$\tilde{\Gamma} = 1 \tag{7.3}$$

and [1]

$$d_c = 2\tilde{\Gamma} = 2. \tag{7.4}$$

Although the problem is still not completely solved analytically[1] we can offer here the following simple visualization. We view the dislocations as part of an abstract interface which slips in the direction of the external applied stress while it is "held" together and pinned at the same time by the individual dislocation interaction. In that sense we have an abstract ($d =$)2-dimensional slip interface depinning in ($d + 1 =$)3-dimensional space (the stress interaction between 2 straight parallel edge dislocations is calculated to be

[1]The full analytical Renormalization Group calculation of the DDD critical exponents is made extra tedious by the extra difficulty of the anisotropy of the dislocation interaction.

$\tau_{xy} \sim 1/r$ in linear elasticity for an infinite-long straight edge dislocation line living in the unbounded 3-dimensional space.). According to the above simple visualization

$$d_c = 2 = d \tag{7.5}$$

for 2d DDD and one can expect to get results in the MF interface depinning universality class.

In the following we describe exactly how we performed the computer simulations and analyzed the results from DDD.

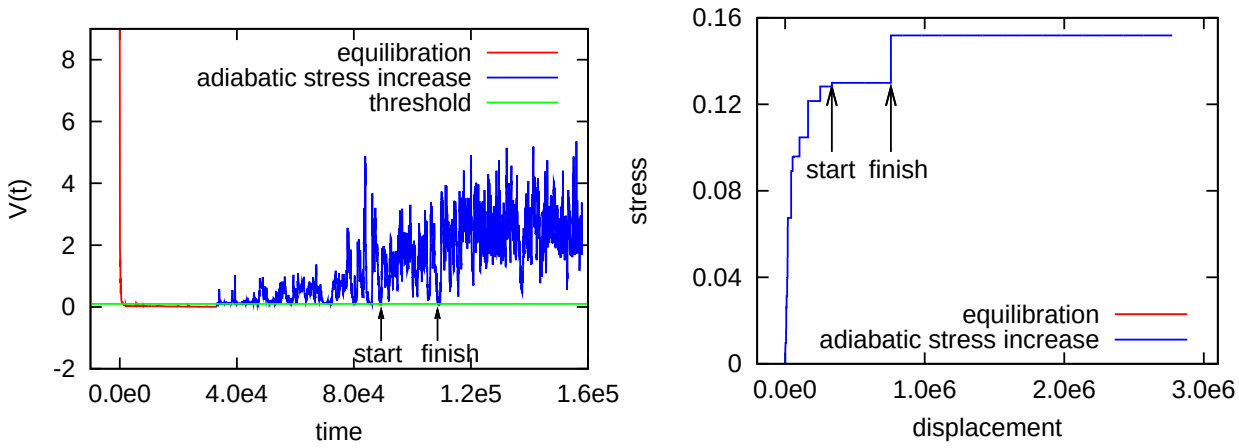

Figure 7.1: (color online) (left) Time series of the collective speed of the dislocations for $N = 64$ dislocations in a square box of side $L = 100$. Displacement at time t is the total distance all the dislocations traveled from the beginning of the simulation ($t = 0$) till time t: $\int_0^t dt' \sum_{i=1}^N b_i dx_i(t')$. (right) External stress vs total dislocation displacement for the same run. The arrows indicate the start and finish of the last large avalanche. (Note that in the stress vs displacement figure the equilibration occurs at zero external stress.)

7.1 Below the critical stress

We start by randomly seeding the N dislocations in the simulation box and letting the system relax to the nearest (metastable) equilibrium state at zero external stress. The dislocation activity approaches zero the closer the system gets to the nearest local energy minimum. A simple eigenmode analysis shows that the time needed for the system to reach zero activity diverges. When the dislocation activity, $V(t)$ (see Eq. (6.8) for definition) has fallen below a threshold, $V_{\rm thr}$, the system is sufficiently close to the nearest local energy minimum [2].

For a typical system of $N = 64$ dislocations in a square box of side $L = 100$, $V_{\rm thr} = 0.1$, which is roughly 100 times less than the initial activity of the system. We increase the external stress adiabatically

[2]The closer the system gets to a local energy minimum the slower it moves and the time it is needed to reach the exact bottom of the energy well diverges, so a threshold has to be applied.

(or quasi-statically) slowly whenever and for as long as the system's activity is below the specified threshold, $V(t) < V_{\rm thr}$. Eventually the increased external stress pushes the system's activity above the threshold. During the time that $V(t) > V_{\rm thr}$ the system produces an avalanche and we keep the external stress constant until the avalanche has completed (Fig. 7.1). We have checked that the scaling behavior is insensitive to the threshold for a value up to ten times larger and smaller.

For relatively low values of the external stress the system responds with small avalanches. As the stress τ approaches the flow stress τ_c, it responds with larger and larger avalanches until at τ_c it finally flows steadily with an infinite avalanche. When the applied stress exceeds the critical value, i.e. $\tau > \tau_c$, we observe the dislocations moving constantly, exiting from one side of the simulation cell and reemerging at the other as a result of the periodic boundary conditions, without ever getting jammed (pinned) again. This is the point when the sample flows in a deformation experiment. In summary, for $\tau < \tau_c$ the system is jammed (pinned). For $\tau > \tau_c$ the system is constantly flowing (Fig. 7.1).

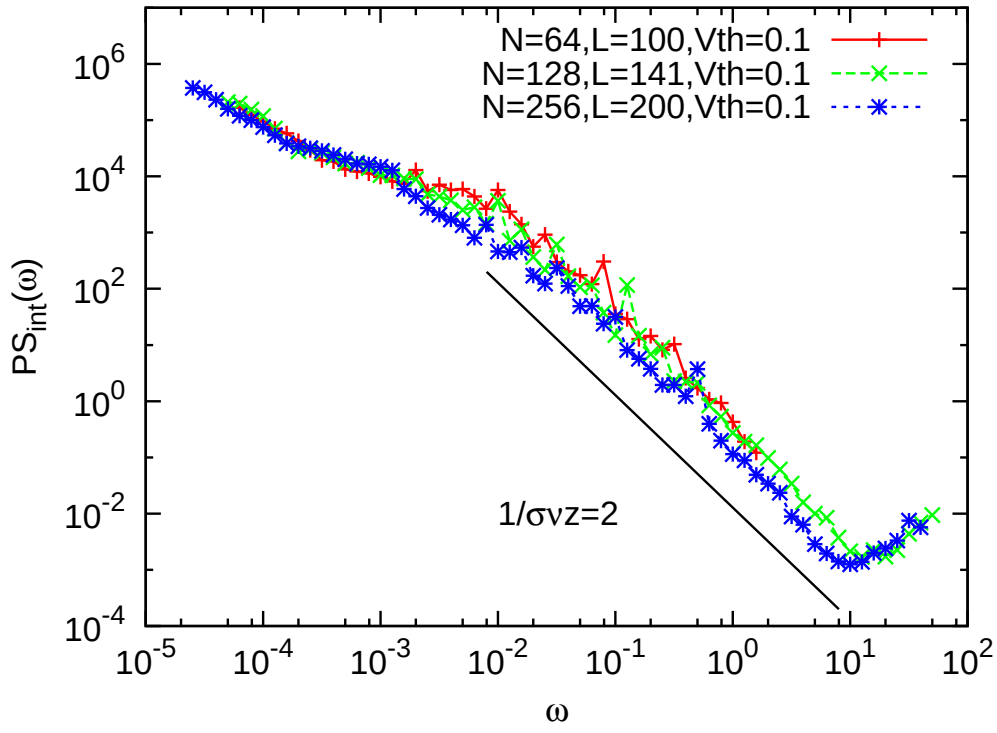

Figure 7.2: (color online) The power spectrum of the dislocation activity, $V(t)$, of the adiabatic increase of the external stress gives a power law of $\frac{1}{\sigma\nu z} \approx 2$ in agreement with MFT. The power-law regime corresponds approximately to the inverse of the $D_t(t_{\rm aval})$ power-law region. Extracted from 288 runs of the system with $N = 64$ dislocations in a box of $L = 100$ and from 96 runs for the systems with $N = 128$ and $L = 141$ and, $N = 256$ and $L = 200$.

7.1.1 Power Spectra Below the critical stress

We calculated the power spectra of the time series of the activity $V(t)$ for all stresses, i.e. $0 < \tau < \tau_c$ (integrated-over-stress), using the Lomb periodogram technique [47]. From Kuntz and Sethna [53] and for a size distribution exponent $\kappa < 2$ the power spectra scales as

$$PS_{\rm int}(\omega) = \left| \int V(t) e^{i\omega t} dt \right|^2 \sim \omega^{-\frac{1}{\sigma\nu z}}. \tag{7.6}$$

Our results are shown in Fig. 7.2 where we find $\frac{1}{\sigma\nu z} \approx 2$ in agreement with MFT.

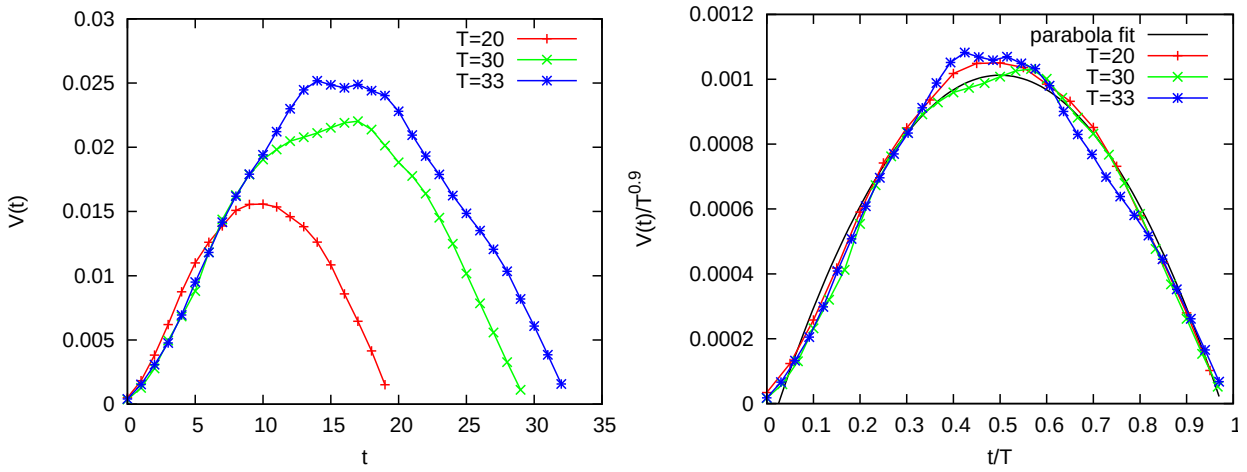

Figure 7.3: (color online) Scaling collapse (right) of the averaged temporal avalanche profiles for $\tau < \tau_c$ shown on the left. The collapse yields $\frac{1}{\sigma\nu z} \approx 1.9$ in agreement with the power spectra both below (Fig. 7.2) and above (Fig. 7.10) τ_c and MFT. Averaged avalanche profiles (shapes) are shown for 3 different durations from the power-law regime of $D_t(t_{\rm aval})$. Extracted from 96 runs with $N = 64$ dislocations in a box of $L = 100$. (Note that $V_{\rm thr} = 0.1$ was subtracted from the signal $V(t)$).

7.1.2 Slip avalanche shapes below the critical stress

A slip avalanche is defined as starting at time $t_{\rm start}$ when $V(t^+_{\rm start}) > V_{\rm thr}$ with $V(t^-_{\rm start}) < V_{\rm thr}$. It ends at $t_{\rm finish}$ when $V(t^-_{\rm finish}) > V_{\rm thr}$ and $V(t^+_{\rm finish}) < V_{\rm thr}$ provided that $V(t) > V_{\rm thr}$ for all $t_{\rm start} < t < t_{\rm finish}$ (see an example in Fig. 7.1). The duration of an avalanche is then

$$t_{\rm aval} = t_{\rm finish} - t_{\rm start}. \tag{7.7}$$

From our simulations we were able to extract for the first time the temporal avalanche speed profiles in the jammed/pinned phase. We collected all the avalanches within $\pm 5\%$ of a duration and averaged their profiles. For sufficiently small durations the avalanches are taken from the power law regime of the duration

distribution. Following Kuntz and Sethna [53] we were able to collapse them using

$$V(t) = t_{\text{aval}}{}^{\frac{1}{\sigma\nu z}-1} f_{\text{shape}}\Big(\frac{t}{t_{\text{aval}}}\Big). \tag{7.8}$$

We obtained a good collapse which indicates that the scaling exponent has the MF value of $\frac{1}{\sigma\nu z} \approx 2$ (Fig. 7.3). In addition the power spectra exponent and the exponent that collapses the avalanche shapes are in excellent agreement. In [8] a power spectra exponent of about 1.5 was found for the activity fluctuations above the critical stress while the system was in the flowing state. In general the activity fluctuations in the flowing state (depinned phase) can be comprised out of several avalanches merged together (in contrast to the pinned phase where increasing the external stress adiabatically slowly makes the system respond with individual avalanches). In the case when individual avalanches merge together their shape may be different from the pure single avalanche shape and may not be amenable to a collapse. One also needs a very large number of avalanches (good statistics) above and below the critical stress in order to produce an average avalanche shape that will reveal self-similarity and give a collapse. In contrast, our power spectra above the critical stress (Fig. 7.10) give the same power-law exponent of $\frac{1}{\sigma\nu z} \approx 2$ as our power spectra below the critical stress (Fig. 7.2).

7.1.3 Slip avalanche distributions below the critical stress

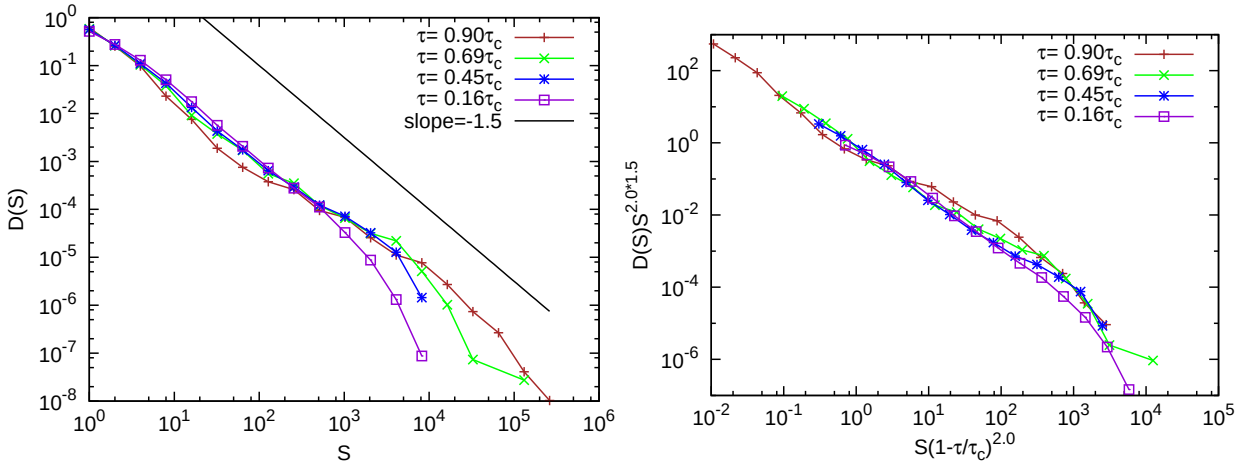

Figure 7.4: (color online) Avalanche size distributions (left) and their scaling collapse (right). It gives $\kappa \approx 1.5$ and $\frac{1}{\sigma} \approx 2$ in agreement with MFT. Extracted from 96 runs with $N = 256$ dislocations in a box of $L = 200$. For the collapse shown we found more convenient the form $D_S(S,\tau)(1-\tau/\tau_c)^{-\kappa/\sigma} \sim g_S(S(1-\tau/\tau_c)^{1/\sigma})$ where g_S is a another scaling function. The scaling function can in principle be extracted by a fit on the collapsed curves. (In producing these distributions we used logarithmic binning and ignored bins with only one count to avoid the trivial power law of $1/S$ that comes from normalizing the logarithmic bins with their size.)

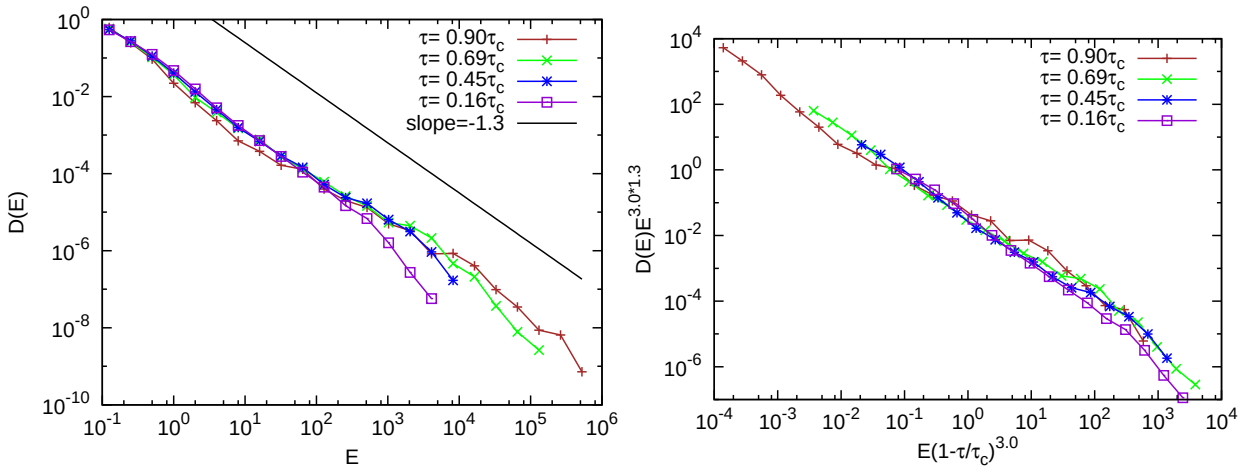

Figure 7.5: (color online) Avalanche energy distributions (left) and their scaling collapse (right). It gives $\kappa_E = 1 + \frac{\kappa-1}{2-\sigma\nu z} \approx 1.3$ and $\frac{2-\sigma\nu z}{\sigma\nu z} \approx 3$ in agreement with MFT. Extracted from 96 runs with $N = 256$ dislocations in a box of $L = 200$. For the collapse shown we found more convenient the form $D_E(E,\tau)(1-\tau/\tau_c)^{-\kappa_E(2-\sigma\nu z)/\sigma} \sim g_E(E(1-\tau/\tau_c)^{(2-\sigma\nu z)/\sigma})$ where g_E is a another scaling function. The scaling function can in principle be extracted by a fit on the collapsed curves. (In producing these distributions we used logarithmic binning and ignored bins with only one count to avoid the trivial power law of $1/E$ that comes from normalizing the logarithmic bins with their size.)

We were also able to extract the probability distribution of the avalanche sizes, durations and energies. We define the size of an avalanche as

$$S = \int_{t_{aval}} V(t)dt \tag{7.9}$$

and the energy as

$$E = \int_{t_{aval}} V^2(t)dt. \tag{7.10}$$

The distribution of energies (shown in Fig. 7.5) at different stresses can be shown to scale as

$$D_E(E,\tau) \sim E^{-1-\frac{\kappa-1}{2-\sigma\nu z}} f_E\left(E\left(1-\frac{\tau}{\tau_c}\right)^{\frac{2-\sigma\nu z}{\sigma}}\right) \tag{7.11}$$

($\kappa_E = 1 + \frac{\kappa-1}{2-\sigma\nu z}$) and the distribution of durations as

$$D_t(t_{aval},\tau) \sim {t_{aval}}^{-1-\frac{\kappa-1}{\sigma\nu z}} f_t\left(t_{aval}\left(1-\frac{\tau}{\tau_c}\right)^{\nu z}\right) \tag{7.12}$$

($\kappa_t = 1 + \frac{\kappa-1}{\sigma\nu z}$) starting from the distribution of sizes (shown in Fig. 7.4)

$$D_S(S,\tau) \sim S^{-\kappa} f_S\left(S\left(1-\frac{\tau}{\tau_c}\right)^{\frac{1}{\sigma}}\right) \tag{7.13}$$

[6], the correlation length as

$$\xi \sim \left(1-\frac{\tau}{\tau_c}\right)^{-\nu} \tag{7.14}$$

and the dynamic exponent is defined as

$$t_{\text{aval}} \sim \xi^z \tag{7.15}$$

(see [1] and/or Appendix B). We calculated all the power-law and cut-off exponents above from our simulations and they are consistent with MFT (see Table 7.1).

The distribution of durations, $D_t(t_{\text{aval}})$, could not be extracted due to finite size effects although we were able to get the power law exponent from the phase field crystal model (PFC) (see Chapter 10). Also much larger system sizes than our maximum $L = 200$ and $N = 256$ are needed to probe the cut-off region of the distributions and finally measure the correct integrated-over-stress ($0 < \tau < \tau_c$) power-law exponents. For example the scaling exponent of $D_{S,\text{int}}(S) \sim S^{-(\kappa+\sigma)}$ has only been observed with continuum models and not yet with DDD models [6] because of the very strong finite size effects that require large systems and long simulations. We present all the exponents in Table 7.1.

7.1.4 Average avalanche size versus duration and average avalanche duration versus size.

The avalanches size S and can be written as

$$S = \int_{\text{t}_{\text{aval}}} V(t)dt = \langle V \rangle t_{\text{aval}} \tag{7.16}$$

where $\langle V \rangle = 1/t_{\text{aval}} \int_{\text{t}_{\text{aval}}} V(t)dt$ is the average height of an avalanche. From Eq. (7.8) we know that $\langle V \rangle \sim {t_{\text{aval}}}^{\frac{1}{\sigma\nu z}-1}$ which gives,

$$S = {t_{\text{aval}}}^{\frac{1}{\sigma\nu z}}. \tag{7.17}$$

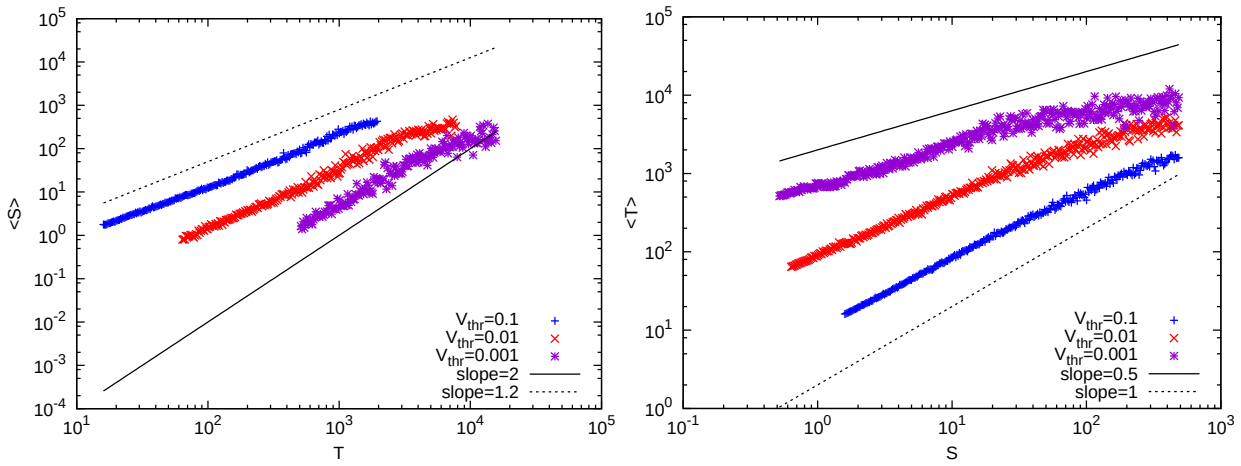

Figure 7.6: (color online) Average avalanche sizes versus durations (left) and average avalanche durations versus sizes (right) for same system sizes and number of dislocations. As the threshold is lowered we get $\frac{1}{\sigma\nu z} \to 2$ and $\sigma\nu z \to \frac{1}{2}$ in agreement with MFT. The power law exponents converge to their MF values as $V_{\rm thr}$ is lowered and the durations are sampled better (The D_t's for lower $V_{\rm thr}$ could not reveal the correct exponents however.). Extracted from 96 runs with $N = 128$ dislocations in a box of $L = 141$ and 3 different thresholds $V_{\rm thr} = 0.1, 0.01, 0.001$.

We can extract this exponent by plotting the average avalanche size for a narrow bin in durations and the average duration in a narrow bin in size,

$$\langle S \rangle = t_{\rm aval}{}^{\frac{1}{\sigma\nu z}} \quad \text{and} \quad \langle t_{\rm aval} \rangle = S^{\sigma\nu z} \tag{7.18}$$

which we show in Fig. 7.6 below. The avalanche durations are plagued by finite-size effects in the sense that we get a few decades in $t_{\rm aval}$ for several decades in S because avalanches can have very different areas for similar horizontal - in time - extensions. However lowering the threshold we get exponent value that converge to the MF predicted value.

7.1.5 Finite-size effects

As the system approaches the flow stress from below, $\tau \to \tau_c$, (i.e. the critical point of the depinning transition) the correlation length diverges,

$$\xi \sim \left(1 - \frac{\tau}{\tau_c}\right)^{-\nu}. \tag{7.19}$$

Up to the point where the correlation length is smaller than the linear system size ($\xi < L$) the maximum avalanche is given by $S_{\rm max} \sim \left(1 - \frac{\tau}{\tau_c}\right)^{-\frac{1}{\sigma}} \sim \xi^{\frac{1}{\sigma\nu}}$. However when the correlation length outgrows the system

size ($\xi > L$) the maximum avalanche is dictated by the system size, $S_{\max} \sim L^{\frac{1}{\sigma\nu}}$.

$$S_{\max} \sim \begin{cases} \xi^{\frac{1}{\sigma\nu}} & \text{for} \quad \xi < L \\ L^{\frac{1}{\sigma\nu}} & \text{for} \quad \xi > L \end{cases} \tag{7.20}$$

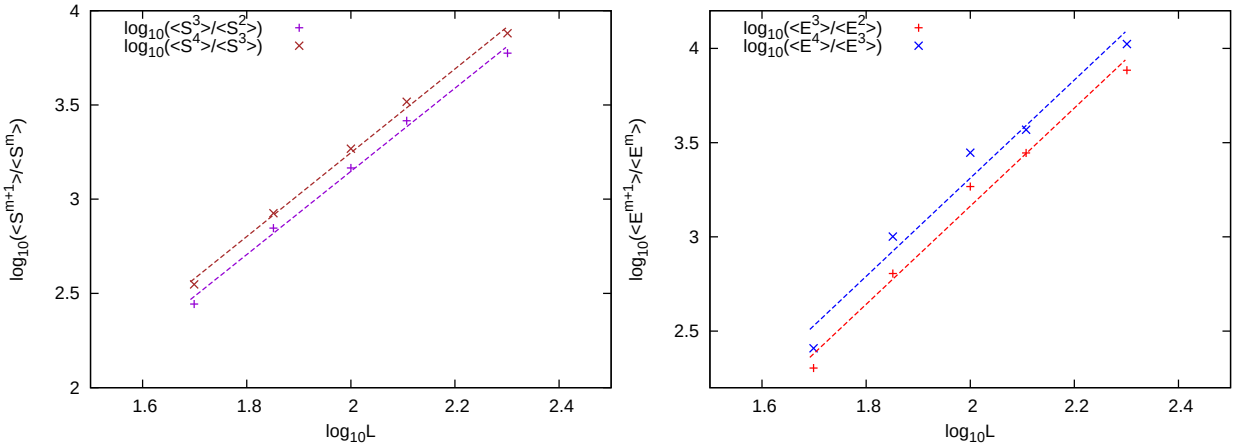

Figure 7.7: (color online) Finite-size scaling analysis for same density dislocation systems at different linear sizes L.We used $N = 16, 32, 64, 128, 256$ dislocations in square boxes of side $L = 50, 71, 100, 141, 200$ respectively and excluded spanning avalanches (a spanning avalanche has at least one dislocation travel by L). The individual linear fits on the moments ratios (dashed lines) are expected to scale as $\log_{10}\frac{\langle S^{m+1}\rangle}{\langle S^m\rangle} \sim \frac{1}{\nu\sigma}\cdot\log_{10}(L)$ (left) and as $\log_{10}\frac{\langle E^{m+1}\rangle}{\langle E^m\rangle} \sim \frac{2-\sigma\nu z}{\nu\sigma}\cdot\log_{10}(L)$ (right) giving for the finite-size exponent $\nu = 1.0 \pm 0.2$.

We can quantify the finite-size effects through the exponent ν (Fig. 7.7). The integrated size distribution can be modified to account for finite-size effects,

$$D_{S,\text{int}}(S, L) \sim S^{-(\kappa+\sigma)} f_{S,int}(SL^{-\frac{1}{\sigma\nu}}). \tag{7.21}$$

We were able to qualitatively observe the increase of the maximum avalanche of $D_{S,int}(S, L)$ with L. We were able to quantify that dependence through the moments,

$$\langle S^m\rangle = \int_0^{S_{\max}} S^m D_{S,\text{int}}(S, L)dS. \tag{7.22}$$

For $m > \kappa + \sigma$ the integral does not diverge at the lower limit and we get

$$\langle S^m\rangle \sim L^{\frac{1+m-\kappa-\sigma}{\nu\sigma}}. \tag{7.23}$$

By plotting

$$\log_{10}\frac{\langle S^{m+1}\rangle}{\langle S^{m}\rangle} \sim \frac{1}{\nu\sigma}\cdot\log_{10}(\mathrm{L}) \tag{7.24}$$

we get consistent values for ν, independent of m. Our results are consistent when we use

$$\langle E^{m}\rangle \sim L^{(m-\frac{\kappa-2}{2-\sigma\nu z})\frac{2-\sigma\nu z}{\nu\sigma}} \tag{7.25}$$

and plot

$$\log_{10}\frac{\langle E^{m+1}\rangle}{\langle E^{m}\rangle} \sim \frac{2-\sigma\nu z}{\nu\sigma}\cdot\log_{10}(L) \tag{7.26}$$

We also tried to extract the dynamic exponent z that shows up in the scaling of the duration moments with the system size,

$$\langle {t_{\mathrm{aval}}}^{m}\rangle \sim L^{(m-\frac{\kappa+\sigma-1}{\sigma\nu z})z} \tag{7.27}$$

through plotting

$$\log_{10}\frac{\langle {t_{\mathrm{aval}}}^{m+1}\rangle}{\langle {t_{\mathrm{aval}}}^{m}\rangle} \sim z\cdot\log_{10}(L). \tag{7.28}$$

Determining z by applying Eq. (7.28) to the data does not yield reliable results because the data for the durations is plagued by unusually large finite size effects and large errorbars. The duration moments are more strongly affected by finite size effects than the moments of the sizes and energies above. Note that the size and energy distributions also have a much wider scaling regime (to be expected as they measure distributions of physical quantities that scale with volume rather than length). We encountered the same strong finite size effects when we attempted to extract z from the distribution of durations above (see Section 7.1.3).

7.2 Above the critical stress

We take as the critical stress τ_c for each system the stress that it reached at the end of the adiabatic run. This is the stress at which the system has reached the infinite avalanche with the dislocations moving out of the basic cell at one side and in at the other due to the periodic boundary conditions.

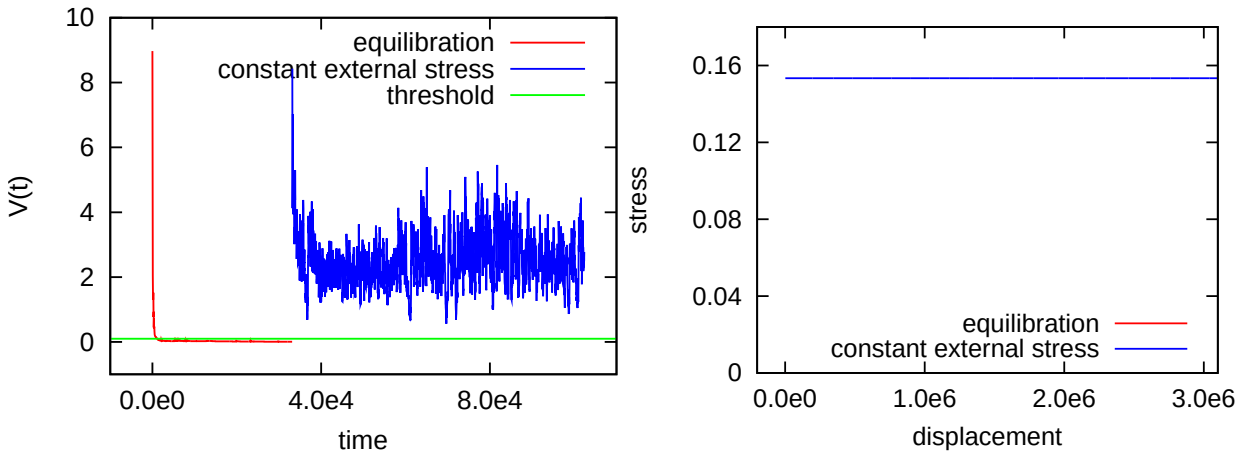

Figure 7.8: (color online) (left) Time series of the collective speed of the dislocations for $N = 64$ dislocations in a square box of side $L = 100$ at 1% higher stress than the critical stress ($\tau = 1.01\tau_c$) of the adiabatic run of the same system and initial conditions. Displacement at time t is the total distance all the dislocations traveled from the beginning of the simulation ($t = 0$) till time t: $\int_0^t dt' \sum_{i=1}^{N} b_i dx_i(t')$. (right) External stress vs total dislocation displacement for the same run. The dislocation system is constantly flowing although one can observe activity fluctuations but no avalanches since the activity does not slow down below $V_{\rm thr}$, the threshold level. (Note that in the stress vs displacement figure the equilibration occurs at zero external stress.)

7.2.1 Average flow rate above the critical stress

The critical stress τ_c is not a universal quantity and every system with the same number of dislocations and box size has a different τ_c. Knowing the critical stresses from the adiabatic run allowed us to run at a fixed fraction above each realization's own critical stress.

We obtain a transition from the pinned to the depinned phase and a linear relationship between mean dislocation activity and distance from the critical point for stresses above the critical stress:

$$\langle V \rangle \sim \left(\frac{\tau}{\tau_c} - 1 \right)^{\beta} \quad \text{with} \quad \beta \approx 1 \tag{7.29}$$

(Fig. 7.9). This result agrees with MFT predictions [28, 45] and it is different from [24] where the critical stress was determined in a collective manner for the entire ensemble. Our treatment suppresses the effect of the ensemble stress fluctuations on the calculation of β, but we expect that the two approaches should yield the same exponent in the thermodynamic limit.

7.2.2 Power Spectra Above the critical stress

We also calculated the power spectra of the dislocation collective speed for stresses above the critical stress. They exhibit power law that extends for over 2 decades in frequency and from very close to the critical

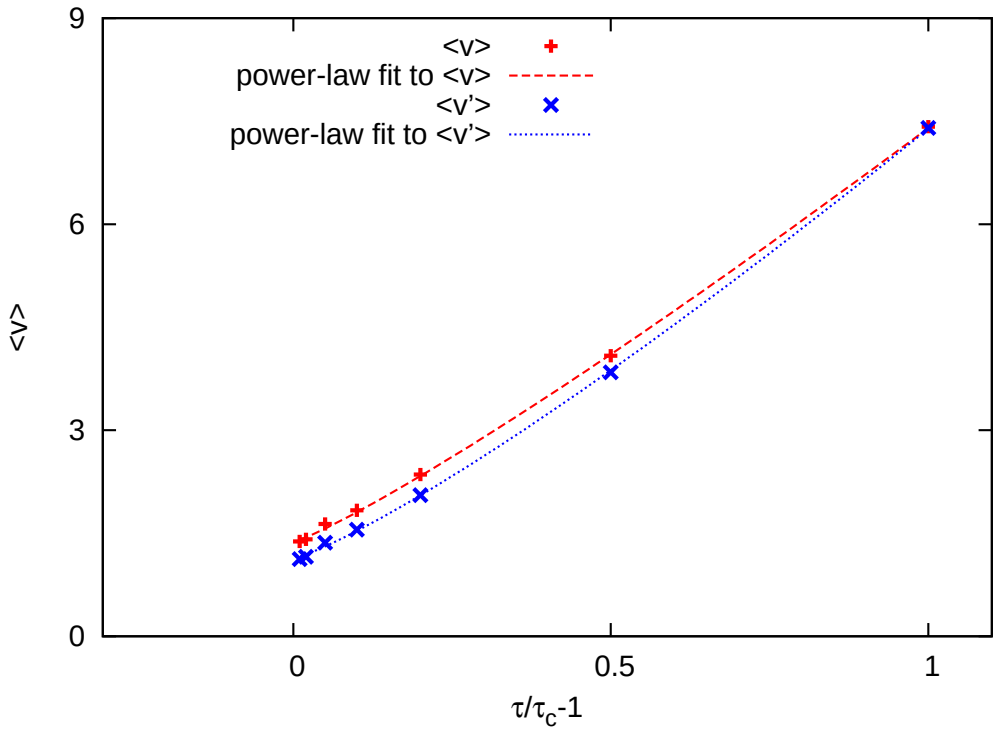

Figure 7.9: (color online) Mean collective speed ($V(t) = \sum_{i=1}^{N} |v_i(t)|$) and mean strain rate ($V'(t) = \sum_{i=1}^{N} b_i v_i(t)$) plotted against the reduced stress above the critical stress. Power-law fits were performed: $\langle V \rangle \approx 1.38(\pm 0.03) + 6.03(\pm 0.05)(\tau/\tau_c - 1)^{1.14(\pm 0.02)}$ and $\langle V' \rangle \approx 1.13(\pm 0.03) + 6.26(\pm 0.04)(\tau/\tau_c - 1)^{1.19(\pm 0.02)}$. Both measures yield a MF value of $\beta \approx 1$. (The value of β is more sensitive to the number of points used in the fit than the statistical errors indicate. The statistical errors quoted are not the dominant errors. In the numerical study of a critical phenomenon the systematic errors dominate.) Each of the 7 points $(\tau/\tau_c = 1.01, 1.02, 1.05, 1.1, 1.2, 1.5, 2.0)$ is extracted from 96 runs with $N = 64$ dislocations in a square box of side $L = 100$.

stress, $\tau = 1.01\tau_c$, to up to $\tau = 2.00\tau_c$ or 100% above the critical stress. One can see this in Fig. 7.10. Note that the power spectrum at stress $\tau = 3.00\tau_c$ does not follow a power law meaning that the critical region does not extend to 200% above the critical stress.

7.3 Discussion

We presented here the first avalanche shape collapse and power spectrum below the critical point of plasticity. The avalanche shape collapse exponent, $1/\sigma\nu z$, agrees with the power spectrum scaling exponent. In fact all the exponents we calculated are in very good agreement with the MF values of the Interface Depinning Transition Universality Class. Thus we have shown that even the temporal characteristics of crystalline deformation, in the absence of work-hardening, belong to the universality class of the MF pinning-depinning phase transition. This should be particularly true for nanometer sized materials where prolific dislocation sources are scarce and exhibit minimal hardening as is evident from the stress-strain curves in single crystal

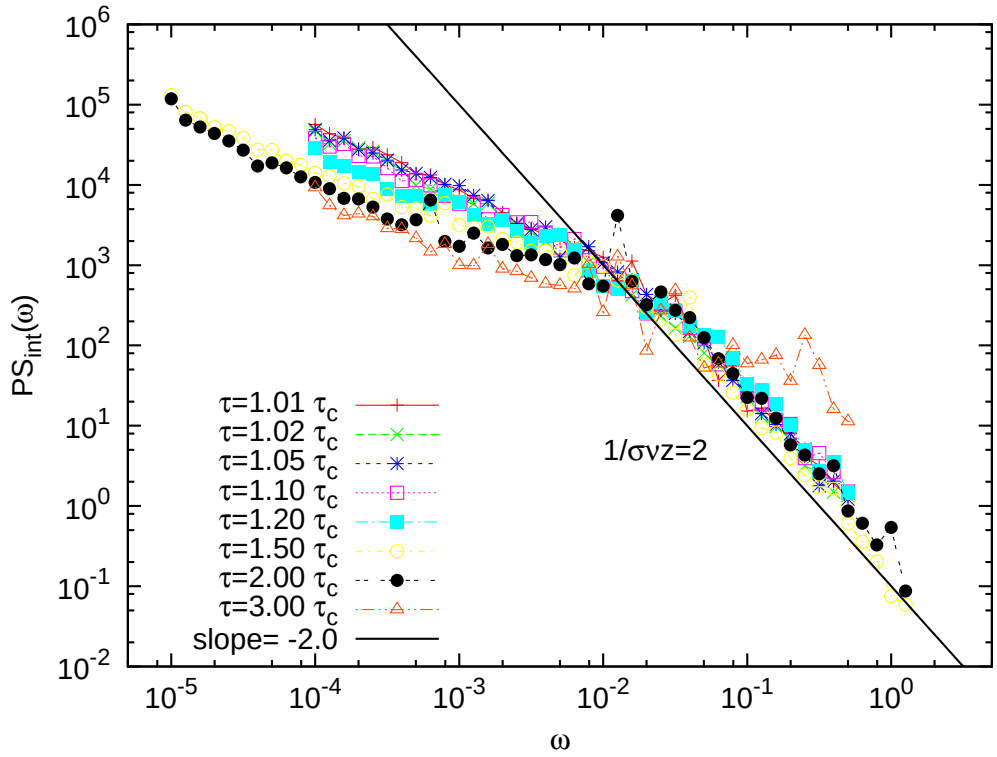

Figure 7.10: (color online) The power spectrum of the dislocation activity, $V(t)$, for external stress above the critical stress gives a power law of $\frac{1}{\sigma\nu z} \approx 2$. This is in agreement with the power spectra below the critical stress (Fig. 7.2), the avalanche shapes collapse (Fig. 7.3) and MFT. Extracted from 96 runs of the system with $N = 64$ dislocations in a box of $L = 100$ and $\tau = 1.01, 1.02, 1.05, 1.1, 1.2, 1.5, 2.0, 3.0\tau_c$. Notice that for $\tau = 3.0\tau_c$ the power spectrum does not follow a power law and thus it is outside the critical region. Presumably the upper end of the critical region up to where the critical power law scaling of the depinning transition is seen is at a stress, $\tau_{\rm upper}$, that lies $2.0\tau_c < \tau_{\rm upper} < 3.0\tau_c$.

FCC nanopillars like Au [22] or Cu [48] and elucidated by the numerical work of Weinberger and Cai [49]. Friedman *et al.* [50] analyzed deformation avalanches from nano-scale samples and found it agrees with MFT as well.

quantity	exponent	ours DDD	ours PFC	MFT	sims	experiments
$D(S) \sim S^{-\kappa}$	κ	1.5 (Fig. 7.4)	1.5 (Fig. 10.3, 10.4)	$\frac{3}{2}$	1.4[6],1.6[7],1.5[11]*	1.5-1.6[4],1.5[22]
$S_{\max} \sim \left(1-\frac{\tau}{\tau_c}\right)^{-\frac{1}{\sigma}}$	$\frac{1}{\sigma}$	2 (Fig. 7.4)		2	2[6],2[11]*	2[6]
$D(V_{\max})$						2[54], 2.0 ± 0.1[18],
"						1.5-2[20],1.2-2.2[19]
$D_t \sim {t_{\text{aval}}}^{-1-\frac{\kappa-1}{\sigma\nu z}}$	$\kappa_t = 1+\frac{\kappa-1}{\sigma\nu z}$		2 (Fig. 10.3, 10.4)	2		
$t_{\text{aval,max}} \sim \left(1-\frac{\tau}{\tau_c}\right)^{-\nu z}$	νz			1		
$D(E) \sim E^{-\frac{1+\kappa-\sigma\nu z}{2-\sigma\nu z}}$	$\kappa_E = 1+\frac{\kappa-1}{2-\sigma\nu z}$	1.3 (Fig. 7.5)	1.3 (Fig. 10.3, 10.4)	$\frac{4}{3}$	$1.8 \pm .2$[5]$^+$	1.6 ± 0.05[5],$1.5 \pm .1$[17]
$E_{\max} \sim \left(1-\frac{\tau}{\tau_c}\right)^{-\frac{2-\sigma\nu z}{\sigma}}$	$\frac{2-\sigma\nu z}{\sigma}$	3 (Fig. 7.5)		3		
$\langle S\rangle \sim {t_{\text{aval}}}^{\frac{1}{\sigma\nu z}}$	$\frac{1}{\sigma\nu z}$	$\to 2$ (Fig. 7.6)	2 (Fig. 10.3, 10.4)	2	1.5[8]$^+$	
$\langle t_{\text{aval}}\rangle \sim S^{\sigma\nu z}$	$\sigma\nu z$	$\to 0.5$ (Fig. 7.6)		$\frac{1}{2}$		
$V(t)_{\text{shape}} \sim {t_{\text{aval}}}^{\frac{1}{\sigma\nu z}-1}$	$\frac{1}{\sigma\nu z}$	~ 1.9 (Fig. 7.3)		2	1.5[8]$^+$	
$PS_{\text{int}}(\omega) \sim \omega^{-\frac{1}{\sigma\nu z}}$	$\frac{1}{\sigma\nu z}$	~ 2 (Fig. 7.2, 7.10)		2	1.5[8]$^+$	
$\langle S^m\rangle \sim L^{\frac{1+m-\kappa-\sigma}{\nu\sigma}}$	ν	1.0 ± 0.2 (Fig. 7.7)		1		
$\langle v\rangle \sim \left(\frac{\tau}{\tau_c}-1\right)^{\beta}$	β	~ 1.1 (Fig. 7.9)		1	1.8[24]$^+$	

Table 7.1: Table of exponents. Our results from a 2d DDD are shown in the second column. Results from a full 3d DDD simulation are indicated with an asterisk (*). Results from a 2d DDD simulation with creation and annihilation in the steady state are indicated with a plus sign ($^+$). In the numerical work of [6, 1], the total slip of the dislocation system $L_{\text{aval}} = \int_{t_{\text{aval}}} dt \sum_{i=1}^{N} b_i v_i(t) = \sum_{i=1}^{N} b_i \Delta x_{i,t_{\text{aval}}}$ was used to measure the size of the avalanche. Our simulations calculate the collective slip produced by the dislocation system $S = \int_{t_{\text{aval}}} dt \sum_{i=1}^{N} |v_i(t)| = \sum_{i=1}^{N} |\Delta x_{i,t_{\text{aval}}}|$ during an avalanche. For large avalanches, the total slip and collective slip have the same scaling behavior. (It's common in acoustic emission experiments to consider the distribution of the maximum peak activity, $V_{\max}$, during an avalanche (e.g. [18, 19, 20]). Extremal (a.k.a. order) statistics for non-independent and non-identically distributed variables (non-i.i.d.) are complicated to calculate analytically. The values $V(t)$ in an avalanche are correlated because the power spectrum is not white noise. Therefore the derivation of the scaling of the statistics of $V_{\max}$ is not straightforward. On the other hand the distributions of the avalanche measures S, E and L_{aval} are easily derived and compared to MFT.)

Chapter 8

Dislocation Jamming

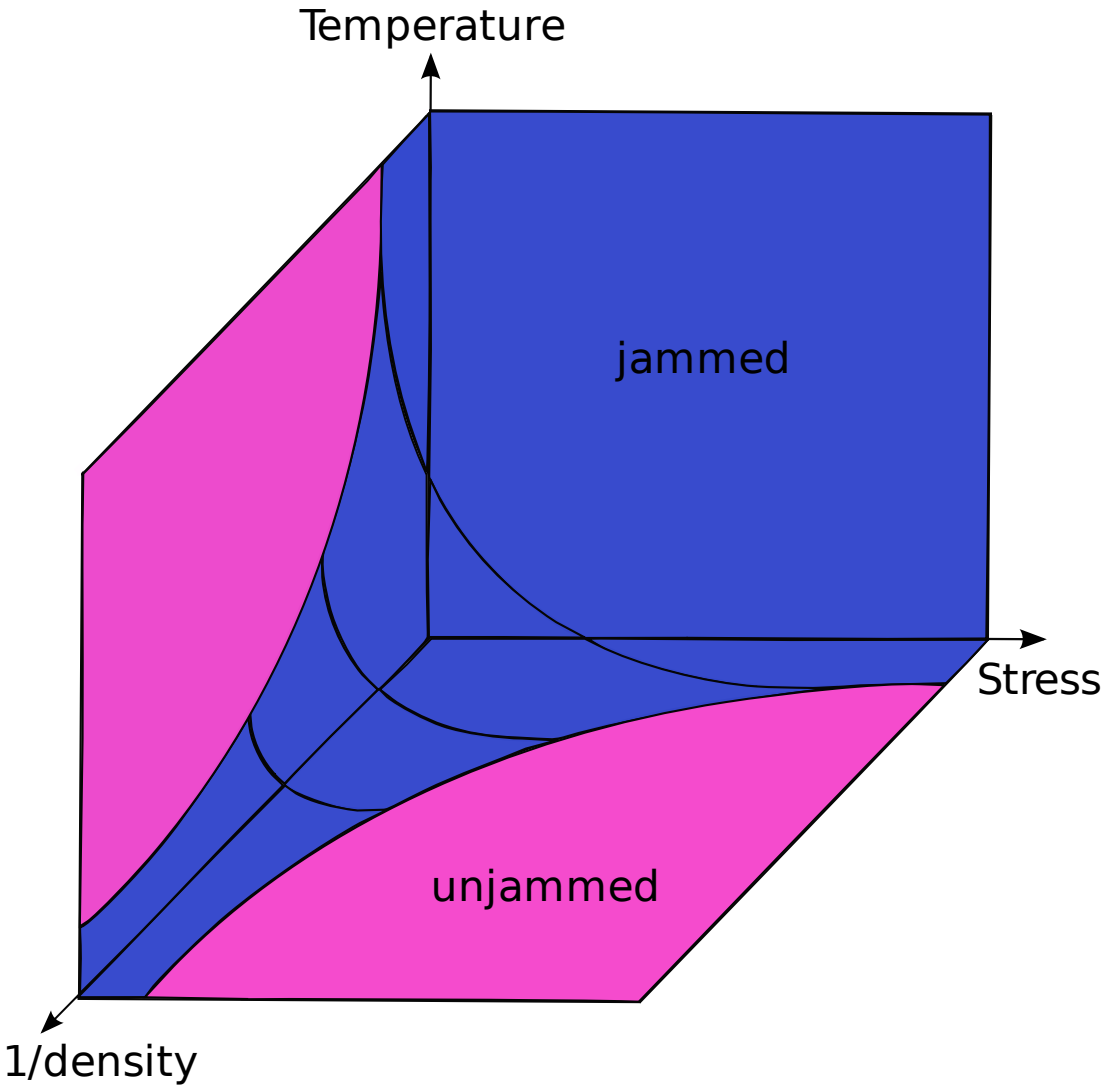

Figure 8.1: (color online) Proposed jamming phase diagram for dislocation systems. Notice the absence of a jamming point.

[1] In this chapter we study connections between the plastic yield point of systems with long range inter-

[1]This work of ours was published in Physical Review Letters [10].

actions, such as dislocation systems and the jamming transition of systems with short range interactions, such as sheared granular materials and molecular liquids [55, 56, 57, 58]. When a system jams it undergoes a transition from a flowing state (analogous to a depinned phase) to a rigid state (analogous to a pinned phase). In contrast to the ordered solid phase obtainable via crystallization, the solid phase reached via jamming remains disordered. Liu and Nagel [55], O'Hern *et al.* [56, 57] and others [58] studied jamming of granular materials with short range interactions in simulations and experiments. They found that below a critical density these materials do not jam at any stress. This critical density is called the jamming point J of granular materials. In contrast, we show here that dislocations jam at any nonzero density, i.e. dislocations have no jamming point. The physical reason is that dislocations have long range interactions that can lead to pinning for arbitrarily large distances between the dislocations. Fig. 8.1 sketches the putative jamming phase diagram (in the absence of screening) for dislocation-mediated plasticity. It is closely related to the jamming phase diagram of [58] for granular materials, except for the absence of a jamming point J for dislocations.

In the following we employ analytical calculations and discrete dislocation dynamics simulations to study how the critical (flow) stress depends on the dislocation density ρ. Our analytical calculations verify and generalize the numerical findings.

8.1 Numerical Calculation of Critical Stress; Taylor relation

The critical stress τ_c is not a universal quantity and every system with the same number of dislocations and box size has a different τ_c. We performed an adiabatically slow increase of the stress for different dislocation densities, $\rho = N/L^2$. The cumulative distributions of the critical stresses is shown in left Fig. 8.2 & 8.4. One can observe that the distributions become narrower for smaller densities, as does the mean critical stress of the ensemble. The scaling collapse shown in right Fig. 8.2 & 8.4 gives (to first order in ρ) the relationship

$$\tau_c \sim \sqrt{\rho} \tag{8.1}$$

also known as the Taylor relation [59].

The dislocation system exhibits jamming for $\tau < \tau_c$ analogous to the work of Liu and Nagel [55] and O'Hern *et al.* [56, 57]. Their systems are different from ours in that they had exclusively short range interactions (contact interactions of soft spheres) and we have long range (besides the core interactions that are enforcing the "no climb" constraint). They observed similar distributions of depinning stresses and a similar concave up dependence of the flow stress on the density (Fig. 8.3). However in contrast to their

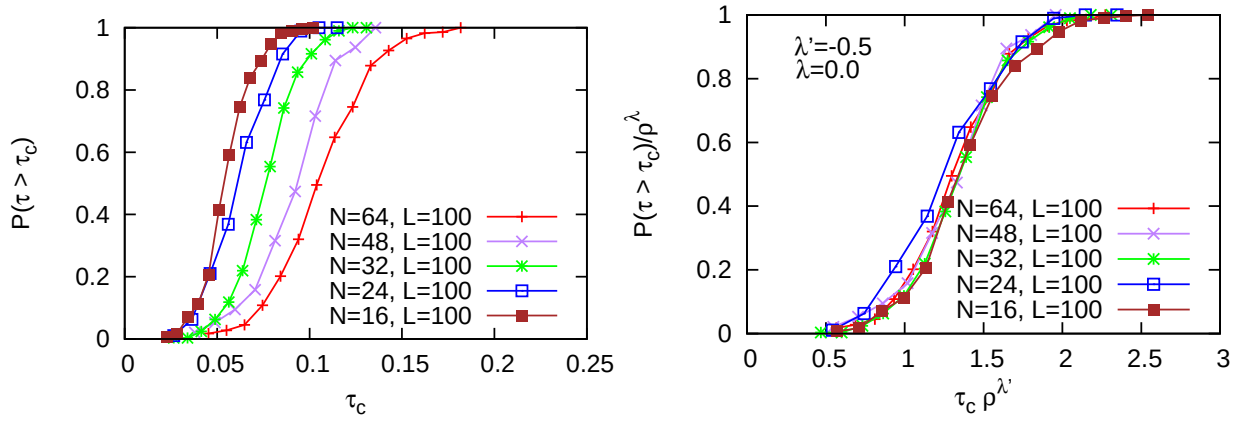

Figure 8.2: (color online) (left) The cumulative distribution of critical stresses τ_c for 5 different numerical densities. Each curve is extracted from 288 runs with $N = 64, 32, 16$ dislocations and 96 runs with $N = 48, 24$ dislocations in a square box of side $L = 100$. The smaller the density, the narrower the distribution and smaller the mean τ_c (see next Fig. 8.3). (right) We obtain a good collapse using the expression $p(\tau_c, \rho) \sim \rho^{\lambda} f[\tau_c \rho^{\lambda'}]$. $\lambda = 0$ since the cumulative probability is restricted in $[0, 1]$. $\lambda' = -0.5 \pm 0.02$. The rescaling of the horizontal axis indicates that $\tau_c \sim \rho^{0.5}$. The collapse quantifies the fact that the distributions get steeper and have a smaller mean for lower density ρ (see Fig. 8.3).

results, we neither expect nor find a jamming point equivalent to their jamming point J where $\tau_c = 0$. This means there can be no density, however small, that will unjam our system at zero applied external stress. The reason is that dislocations have long-range interactions [58]. No matter how far apart they are, they always feel each other.

8.2 Theoretical Calculation of Critical Stress

Consider $N^{+}_{R,\Delta R}$ positive and $N^{-}_{R,\Delta R}$ negative edge dislocations parallel to the z-axis randomly distributed on a ring of radius R and thickness ΔR on the (x, y)-plane. The stress exerted at the origin is given by,

$$\tau_{R,\Delta R} = \int_{R}^{R+\Delta R} d^2 r \frac{\rho^{+}(r,\theta) - \rho^{-}(r,\theta)}{r} K(\theta) \tag{8.2}$$

adapted from [60] using Eq. (6.2) where

$$\rho^{\pm}(r,\theta) = \sum_{i=1}^{N^{\pm}_{R,\Delta R}} \frac{\delta(r - r_i)}{r^{d-1}} \delta(\theta - \theta_i) \tag{8.3}$$

and

$$K(\theta) \sim \cos(\theta)\cos(2\theta). \tag{8.4}$$

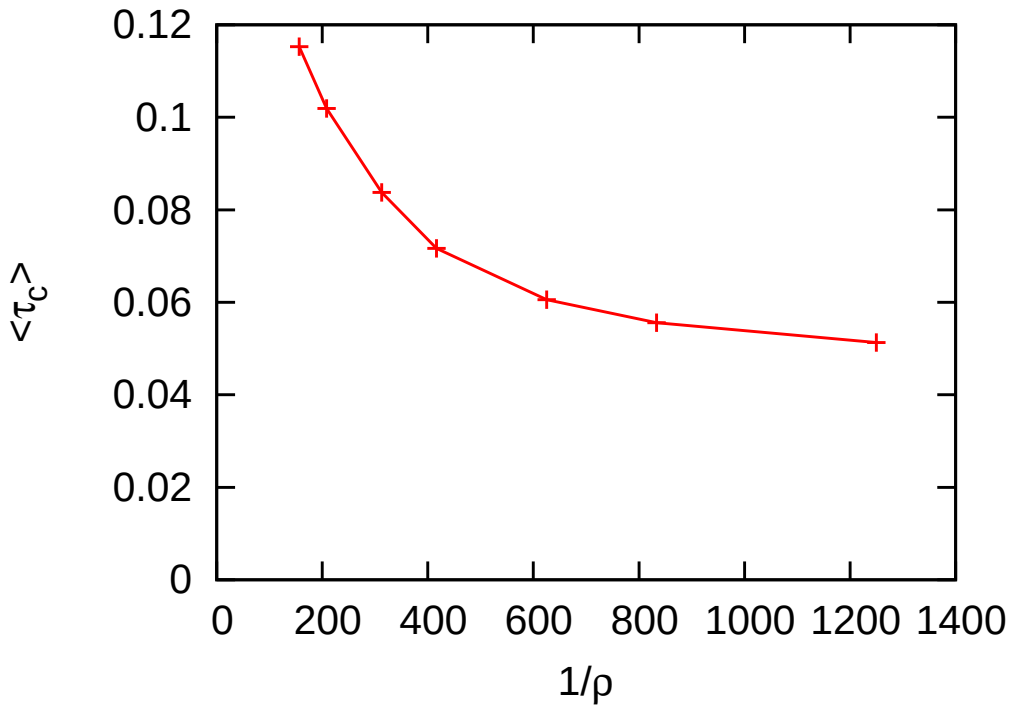

Figure 8.3: (color online) The mean critical stress $\langle \tau_c \rangle$ plotted against the inverse numerical dislocation density ρ. The system is jammed below the line ($\tau < \tau_c$) and unjammed above the line ($\tau > \tau_c$). Each point is extracted from 288 runs with $N = 64, 32, 16, 8$ dislocations and 96 runs with $N = 48, 24, 12$ dislocations in a square box of side $L = 100$. The critical stress has a similar qualitative dependence on the density as in the proposed jamming phase diagram by Liu and Nagel [55]. However for dislocations $\tau_c(\rho) > 0$ for all non-zero densities ρ.

We express all distances in terms of l, the mean dislocation distance, i.e. $\rho = N/L^d = 1/l^d$ in d dimensions, i.e. $X = R/l$ and $x = r/l$. For any power law $r^{-\alpha}$ interaction, we get

$$\tau_{X,\Delta X} = \frac{l^d}{l^\alpha} \int_X^{X+\Delta X} d^d x \frac{\rho^+(x,\Theta) - \rho^-(x,\Theta)}{x^\alpha} K(\Theta) \tag{8.5}$$

with

$$\rho^\pm(x,\Theta) = \frac{1}{l^d} \sum_{i=1}^{N^\pm_{X,\Delta X}} \frac{\delta(x - x_i)}{x^{d-1}} \delta(\Theta - \Theta_i). \tag{8.6}$$

where Θ now is a generalized angle in d dimensions. For small ring thickness we can approximate the integral with the value of the integrand at X times ΔX. The average over the number of the dislocations to first order gives

$$\langle \tau_{X,\Delta X} \rangle \sim \frac{1}{l^\alpha X^\alpha} (\langle N^+_{X,\Delta X} \rangle - \langle N^-_{X,\Delta X} \rangle) = 0 \tag{8.7}$$

with

$$\langle N^+ \rangle = \langle N^- \rangle = \langle N \rangle. \tag{8.8}$$

The effect of the number fluctuations on the stress per ring thickness is:

$$\langle \tau^2_{X,\Delta X} \rangle \sim \frac{\langle (N^+_{X,\Delta X} - N^-_{X,\Delta X})^2 \rangle}{l^{2\alpha} X^{2\alpha}} \sim \frac{1}{l^{2\alpha}} \frac{\langle N_{X,\Delta X} \rangle}{X^{2\alpha}} \tag{8.9}$$

since $N^{\pm}$ are independent random variables, Poisson distributed with the same mean and variance. Assuming that there are N dislocations of each kind in the entire area L^d where $X_L = L/l >> 1$, their mean number in the ring can be expressed as

$$\langle N_{X,\Delta X} \rangle \sim N \frac{X^{d-1} \Delta X}{X_L^d}. \tag{8.10}$$

Substituting into Eq. (8.9) we find,

$$\langle \tau^2_{X,\Delta X} \rangle \sim \frac{1}{l^{2\alpha}} \frac{N}{X_L^d} \frac{\Delta X}{X^{2\alpha - d + 1}}. \tag{8.11}$$

Integrating over the entire region and using $N/X_L^d = 1$ we extract the global stress fluctuations

$$\langle \tau^2 \rangle \equiv \int \langle (\tau^2_{X,\Delta X} \rangle \sim \frac{1}{l^{2\alpha}} \int_{X_{min}}^{X_L} \frac{dX}{X^{2\alpha - d + 1}}. \tag{8.12}$$

With $X_{min} = b/l$ the closest possible distance between 2 dislocations it gives us

$$\sqrt{\langle \tau^2 \rangle} \sim \frac{1}{l^{\alpha}} \frac{1}{\sqrt{2\alpha - d}} \sqrt{\frac{1}{X_{min}^{2\alpha - d}} - \frac{1}{X_L^{2\alpha - d}}} \tag{8.13}$$

$$\sim \frac{1}{l^{\frac{d}{2}}} \frac{1}{\sqrt{2\alpha - d}} \sqrt{\frac{1}{b^{2\alpha - d}} - \frac{1}{L^{2\alpha - d}}} \tag{8.14}$$

$$\sim \sqrt{\rho} \frac{1}{\sqrt{2\alpha - d}} \sqrt{\frac{1}{b^{2\alpha - d}} - \frac{1}{L^{2\alpha - d}}} \tag{8.15}$$

for $2\alpha > d$. In the thermodynamic limit, $L \to \infty$, this translates to the rms stress scaling as

$$\sqrt{\langle \tau^2 \rangle} \sim \sqrt{\rho}. \tag{8.16}$$

For $2\alpha < d$,

$$\sqrt{\langle \tau^2 \rangle} \sim \frac{1}{l^\alpha} \frac{1}{\sqrt{d-2\alpha}} \sqrt{X_L^{d-2\alpha} - X_{min}^{d-2\alpha}} \tag{8.17}$$

$$\sim \frac{1}{l^{\frac{d}{2}}} \frac{1}{\sqrt{d-2\alpha}} \sqrt{L^{d-2\alpha} - b^{d-2\alpha}} \tag{8.18}$$

$$\sim \sqrt{\rho} \frac{1}{\sqrt{d-2\alpha}} \sqrt{L^{d-2\alpha} - b^{d-2\alpha}} \tag{8.19}$$

and the thermodynamic limit doesn't exist. For parallel straight edge dislocations in 2 dimensions $2\alpha = d = 2$ and

$$\sqrt{\langle \tau^2 \rangle} \sim \frac{1}{l^{\frac{d}{2}}} \sqrt{\ln(L/b)} \sim \sqrt{\rho} \sqrt{\ln(L/b)} \tag{8.20}$$

This agrees with our numerical result from the scaling collapse in Fig. 8.2 which was at fixed system size $L = 100$ and the numerical result from the scaling collapse in Fig. 8.4 which was at fixed dislocation number $N = 32$. The two scaling collapses verify the appropriate choice for the lower limit of the integral in Eq. 8.12 which leads to Eq. 8.20.

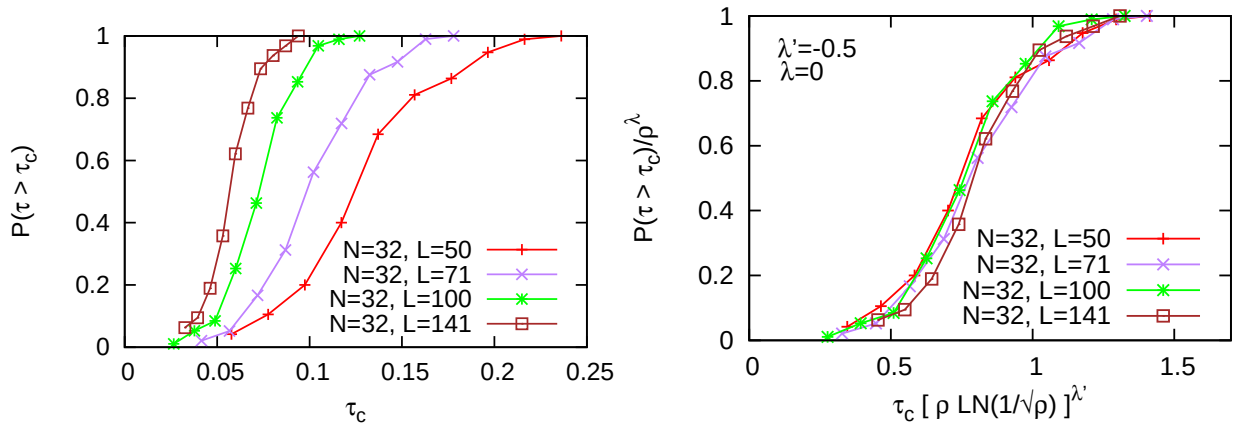

Figure 8.4: (color online) (left) The cumulative distribution of critical stresses τ_c for 4 different numerical densities. Each curve is extracted from 96 runs with $N = 32$ dislocations in a square box of side $L = 50, 71, 100, 141$. The smaller the density, the narrower the distribution and smaller the mean τ_c (similar to Fig. 8.3). (right) We obtain a good collapse based on the expression $p(\tau_c, \rho) \sim \rho^\lambda f[\tau_c(\rho \ln(1/\sqrt{\rho}))^{\lambda'}]$. The collapse quantifies the fact that the distributions get steeper and have a smaller mean for lower density ρ. The exponent $\lambda = 0$ since the cumulative probability is restricted in $[0, 1]$. $\lambda' \approx -0.5$ approximately. The rescaling of the horizontal axis indicates that $\tau_c \sim (\rho \ln(1/\sqrt{\rho}))^{0.5}$ which is equivalent to Eq. 8.20 for fixed N.

8.3 Discussion

We were able to show, using a discrete dislocation dynamics model, that the mean critical stress of an ensemble of dislocation systems with long-range interactions, $\tau_{\text{int}} \sim 1/r$, scales with the square root of the dislocation density, $\langle \tau_c \rangle \sim \sqrt{\rho}$, for straight parallel edge dislocations. Eq. (8.20) also agrees with the Taylor hardening relation [59] and is analogous to the effective velocity of a point vortex in 2 dimensional hydrodynamics [61]. We were able to perform the analytical calculation for any power law interaction, $\tau_{\text{int}} \sim 1/r^{\alpha}$, and for arbitrary d dimensions. The theoretical result agrees with our simulation at fixed system size $L = \text{const}$. Our results, both numerical and theoretical, show that for dislocations or particles with long-range interactions there can be no jamming point at a finite density (only at $\rho = 0$), even if there is screening with a screening length that grows as dislocation density decreases.

Chapter 9

The Model @ T>0 (PFC)

9.1 The Phase Field Crystal Model

[1] The phase field crystal model describes how the local density of atoms changes with time while maintaining the symmetries and periodicity of the lattice. In addition, the elastic interactions of the atoms are also captured by the PFC allowing for elasticity of the crystal to be expressed. These characteristic properties of the phase field crystal model are distinctly different from the generic phase field model. In a typical phase field model the phase field describes the dynamics of interfaces that separate dissimilar regions without keeping track of the microscopic information inside those regions. As we saw in Chapter 4 Koslowski et al. [13] developed a phase field model to simulate dislocations as interfaces (probably separating crystal regions with different accumulated slip). In studying plasticity it is important to capture the microscopic details such as the dislocations who disrupt the periodicity of the perfect lattice. At the same time is important to capture the macroscopic behavior as well such as the collective motion of the dislocation ensemble. The phase field crystal model is particularly successful in doing that in an elegant way.

Mathematically the phase field crystal (PFC) model is given by the free energy density [63, 64]

$$f = \frac{\rho}{2}(\nabla^2 + 1)^2\rho + \frac{r}{2}\rho^2 + \frac{\rho^4}{4}, \tag{9.1}$$

where r is the undercooling and $\rho(\vec{x}, t)$ is the local density of the phase field. The first term in Eq. (9.1) forces $\rho(\vec{x}, t)$ to be periodic (and one can have a phase field crystal that is able to describe a periodic structure). The last two terms impose a double well potential (to lowest order) similar to the Landau ansatz. For $r > 0$ one gets a liquid, constant ρ, phase (because the potential is single well) while for $r > 0$ one can get a triangular lattice or a striped phase (due to the double well potential). r can be thought of as a reduced temperature, $(T - T_c)/T_c$. The material is liquid for temperatures higher than a critical while it crystalizes for temperatures below a critical. This behavior can be readily seen in the PFC phase diagram, Fig. 9.1.

[1] This work of ours was published in Physical Review Letters [14] while an extensive description of the phase field crystal model can be found in [62].

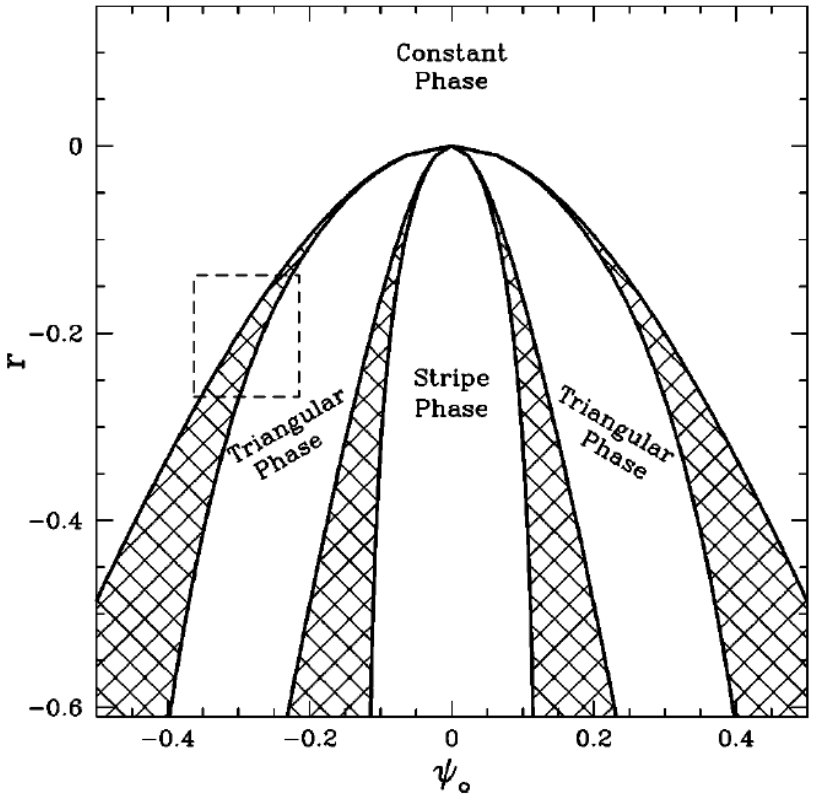

Figure 9.1: The PFC phase diagram. The figure is taken from Elder and Grant [64]. K. R. Elder and Martin Grant, Modeling elastic and plastic deformations in nonequilibrium processing using phase field crystals, Phys. Rev. E, 70:051605, 2004. Copyright 2004 by the American Physical Society.

The dynamics associated with this free energy is conservative, relaxational and diffusive, and systematically derivable from density-functional theory [65].

In order to study the plastic response of the PFC model under shear, we add an applied strain rate along the x direction at the $y = 0, L_y$ boundaries, $v(y)\partial\rho/\partial x$, to the dynamical equation:

$$\frac{\partial^2\rho}{\partial t^2} + (\beta)\frac{\partial\rho}{\partial t} = (\alpha)^2\nabla^2\frac{\delta F}{\delta\rho} + v(y)\frac{\partial\rho}{\partial x} + \eta, \tag{9.2}$$

where

$$v(y) = \begin{cases} v_0 e^{-y/\lambda} & \text{for} \quad 0 < y < L_y/2 \\ -v_0 e^{-(L_y-y)/\lambda} & \text{for} \quad L_y/2 < y < L_y \end{cases} \tag{9.3}$$

is the shearing profile. In Eq. (9.3) v_0 is the magnitude and λ the penetration depth of the shearing rate. The simulations take place in a square box of sides $L_x(L_y)$ in the $x(y)$ direction. In Eq. (9.2) α and β control

the range and time scale of elastic interactions (phonon excitations) propagating through the medium [66],

$$F \equiv \int f(\vec{x}) d^d x \tag{9.4}$$

is the total free energy and η is the thermal noise satisfying the fluctuation-dissipation theorem

$$\langle \eta(\vec{x}, t)\eta(\vec{x}', t')\rangle = -\epsilon\nabla^2\delta(\vec{x} - \vec{x}')\delta(t - t'). \tag{9.5}$$

Here ϵ is the noise amplitude. It is directly proportional to the temperature, $k_B T$. The value of v_0 controls the magnitude of the shearing force; the penetration depth, λ, controls how deep the shearing force extends into the material. In all simulations we set $\lambda \ll L_y$, so the actual value of λ does not affect our simulation results. The boundary conditions are periodic in x and fixed at $y = 0, L_y$ (i.e. we design the simulation cell with the following boundary conditions: the crystal terminates at $y = 0, L_y$ and does not wrap around as in $x = 0, L_x$). That way we can easily apply a fixed shear rate at the $y = 0, L_y$ boundaries (see just above Eq. 9.3) and allow the dislocations to flow unbounded at the $x = 0, L_x$ boundaries effectively simulating a larger thermodynamic system than the mere dimensions of our basic simulation cell.

9.2 Advantages of the Phase Field Crystal Model

One of the advantages of using the PFC model is that we do not have to impose any ad hoc assumptions about the creation and annihilation of dislocations. Recall that in dislocation dynamics simulations, dislocations are treated as elementary particles and usually only the far field interaction between dislocations is captured. When dislocations get too close to each other (a few atomic spacings), the highly nonlinear interaction between them is not captured and more importantly, the annihilation of dislocations is not accounted for. The standard practice is then to impose some annihilation rules—dislocations of opposite topological charges annihilate when they get too close to each other [5]. Similarly, dislocations have to be created by hand when the local strain is high. Although these rules are consistent with our physical intuition, particular ways of implementing them are sometimes difficult to justify. However, because the PFC model captures the nonlinear elastic behavior of a crystal, the interaction between dislocations is completely captured. In addition, because the PFC model simulates the atoms in the lattice (the PFC density is periodic in its ground state with peaks representing atoms and troughs inter-atomic space), but not the dislocations themselves, creation and annihilation of them are also naturally captured as collective excitations of the lattice. No *ad hoc* rules or assumptions have to be imposed.

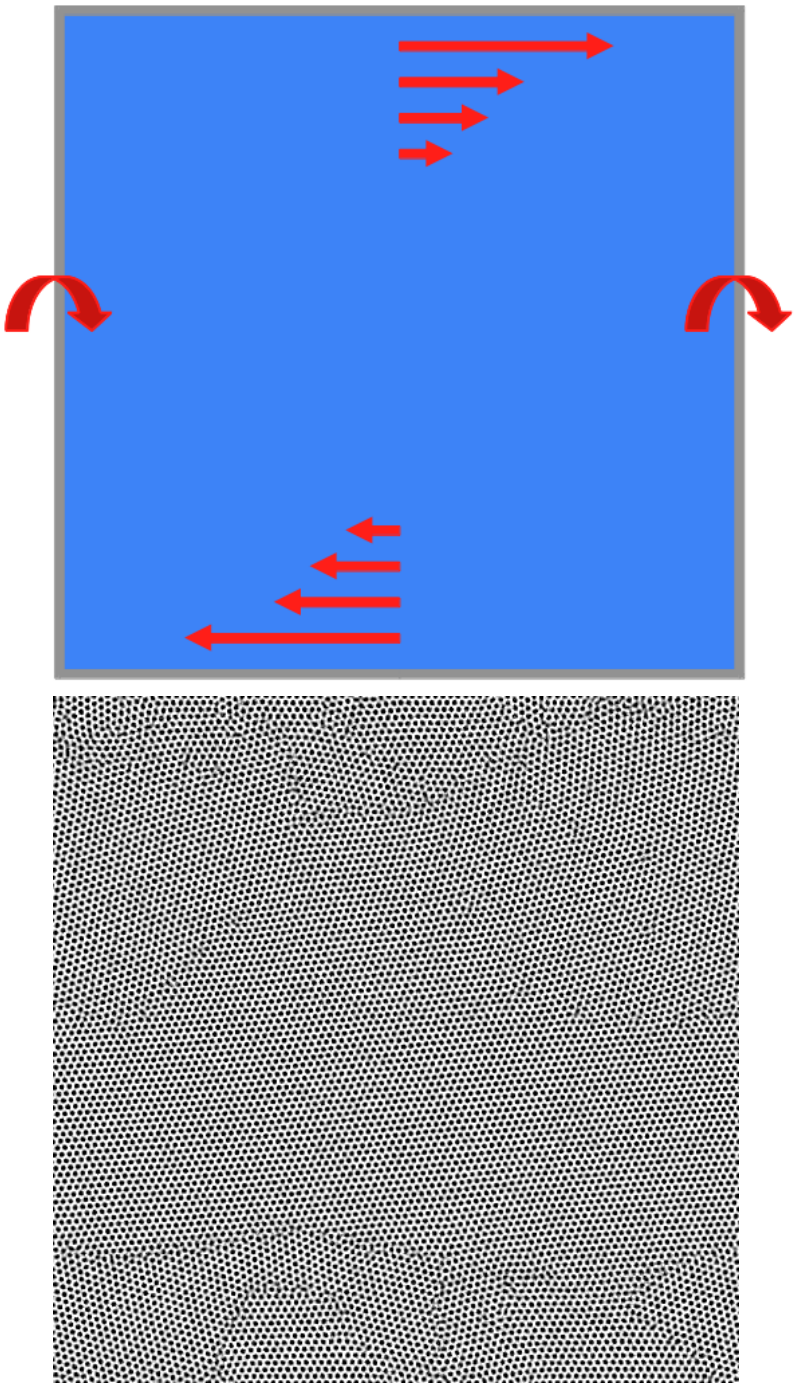

Figure 9.2: (color online) (top) The PFC simulation cell setup where the boundary conditions are indicated: periodic in x and fixed at $y = 0, L_y$ where the exponentially decaying shearing rate is applied. (bottom) A single frame from a PFC simulation. Peaks in ρ can be identified with black and indicate atoms while troughs in ρ are white and signify interatomic space. In the perfect 2-dimensional crystal the PFC "atoms" arrange themselves in a triangular or hexagonal lattice. In that case every atom has exactly 6 neighbors and there are no dislocations. Individual dislocations can be seen near the PFC "atoms" with 5 or 7 neighbors. In some regions dislocations form grain boundaries. The x-axis lies horizontally while the y-axis vertically in these figures.

Chapter 10

Results @ T>0 (PFC)

10.1 Introduction

[1] In this chapter we approach plastic deformation from the flow side of the non-equilibrium critical point, manifested in the strain-rate dependence of the acoustic emission. Importantly, we are able to systematically vary the strain-rate and temperature in simulations, and moreover we relate the critical point underlying plastic flow at finite strain rates to the scaling of interface depinning [25, 1, 44]. We find remarkable agreement between simulations and analytical mean field theory predictions of exponents. Our results strongly support the critical point picture of plasticity, and suggest new experiments.

We study dislocation avalanches during plastic flows using the phase field crystal (PFC) model [63, 64]. This approach is well-suited to this problem, because it can be performed at finite temperature, for large systems, and over long time periods. The PFC model describes the dynamics of the local crystalline density field, and has been shown to give an excellent account of numerous materials properties including polycrystalline solidification, vacancy diffusion, grain growth, grain boundary energetics, epitaxial growth, fracture [64], grain coarsening [67], elasticity [66], dislocation annihilation, glides and climb [68], as well as vacancy dynamics [69]. The model has been applied to the commensurate-incommensurate transition [70] and has been related the density functional theory and extended to the case of binary alloys [71]. In this work, we augment the model to treat external shearing forces by adding an advective term to the dynamics near the boundary. We obtain the main scaling behavior of the distribution of a variety of avalanche measures and for several different temperatures and shearing rates. Our scaling findings are consistent with the interface depinning picture [1, 44].

[1]This chapter is based on work of ours that was published in Physical Review Letters [14].

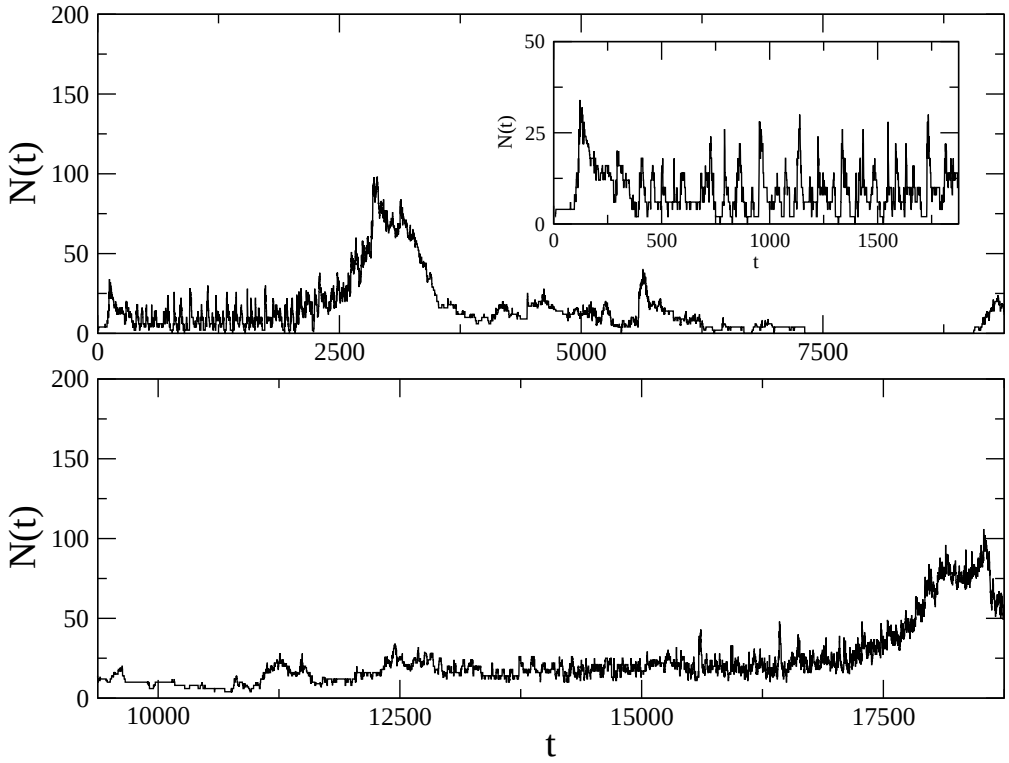

Figure 10.1: The number of dislocations (or the number of defect atoms) in a sheared PFC crystal. Intermittent events with sizes differing in orders of magnitude is observed. Parameters are $L = 512$, $(\alpha)^2 = 255$, $\beta = 0.9$, $v_0 = 1.581$, $\rho_0 = 0.3$, $\epsilon = 1.5$, $\lambda = 40.0$ and $r = -0.5$.

10.2 PFC simulations at Finite Shearing Rate and Temperature

We solve Eq.(9.2) in a 2d square simulation cell (i.e. $L_x = L_y = L$). The crystal is initially perfectly triangular. As the crystal is sheared, dislocations are created near the fixed boundaries $y = 0, L$ where the stress is higher. They then propagate into the bulk. They interact with each other and glide giving slip avalanches. To quantify the avalanche activity, we calculate the total speed of all dislocations in the simulation cell,

$$V(t) = \sum_{i=1}^{N(t)} |\vec{v}_i|, \tag{10.1}$$

where $N(t)$ is the number of dislocations in the system at time t and $\vec{v}_i$ is the velocity of the i-th dislocation. This measure is similar to the acoustic emission signal in Weiss *et al.*'s single crystal ice experiments (e.g. [5]).

As dislocations are generated and interact with each other in the domain, in addition to the fast avalanching dynamics, quasi-static structures, such as grain boundaries, can form. These slow dynamics should not be measured because they are really not part of the avalanches. This leads to the distinction between

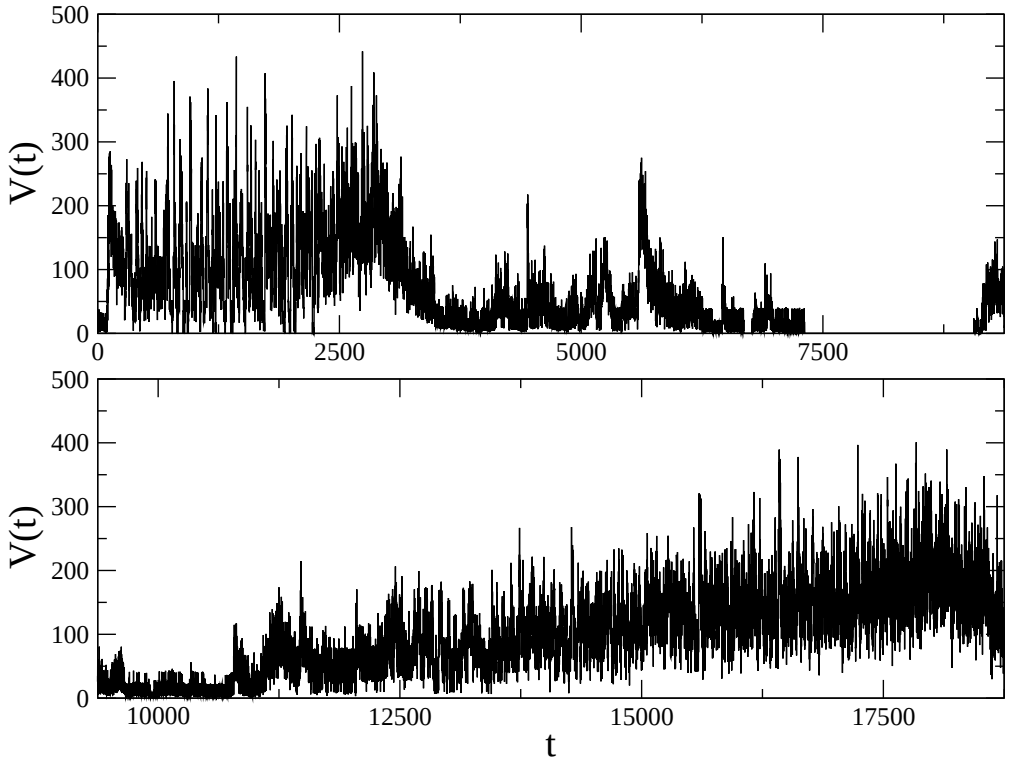

Figure 10.2: The collective speed of dislocations (or defect atoms) in a sheared PFC crystal. Intermittent events with sizes differing in orders of magnitude is observed. Parameters are $L = 512$, $(\alpha)^2 = 255$, $\beta = 0.9$, $v_0 = 1.581$, $\rho_0 = 0.3$, $\epsilon = 1.5$, $\lambda = 40.0$ and $r = -0.5$.

fast-moving and slowly-moving dislocations introduced by Miguel *et al.* [5]. In essence, they introduced a threshold in dislocation speed and measured only dislocations with speed higher than the threshold. In that way, they tried to retain only the avalanche activity in the (spiked) acoustic emission signal but not the background (continuous) noise.

Another way to eliminate the slow dynamics is to study the power spectrum of the signal, instead of studying the signal itself. The slow dynamics, which contributes to a locally smooth background in the total signal then translates into the low frequency end of the power spectrum, which can easily be eliminated. This method is employed for the study of Barkhausen noise in magnets in [53, 72], where the scaling of the power spectrum is also derived.

We employed yet another method to tackle this problem. Instead of simulating a very large system, with all sorts of dislocation activities, we simulated a moderate size of system with approximately 10000 atoms. For this system size, dislocation avalanches come and go, i.e. not many dislocations are left in the system after every avalanche. As a result, no grain boundaries, or slow dynamics, is present and we obtain clean avalanche data. It is fair to mention that this method severely limits the system size, and thus the resulting

avalanche sizes. The system size we chose contains approximately 100 dislocations in the largest avalanche events. The tradeoff, which we exploit, is the cleanness of the avalanche signal and the speed of the resulting simulations. Different methods, such as those we mentioned above, would have to be employed if larger avalanche sizes are desired.

We count the number of nearest neighbors of each atom, n_i, using the Delaunay triangulation method in computational geometry [73, 74]. Because we have $n_i = 6$ for every atom in a perfectly triangular crystal, and because there are no vacancies introduced in our PFC model (vacancies can be introduced into the PFC model by breaking the up-down symmetry of the PFC free energy, as detailed in [69]), any atom having $n_i \neq 6$ is sitting next to a dislocation. So these "defect atoms" are tracking the locations of dislocations. Instead of measuring the total sum of dislocation speeds, $V(t)$, we then measure the total sum of these defect atoms' speeds,

$$\tilde{V}(t) = \sum_{i=1}^{N_{\text{defect}}(t)} |\vec{u}_i|, \tag{10.2}$$

where $N_{\text{defect}}(t)$ is the number of defect atoms and $\vec{u}_i$ is the velocity of defect atom i. Note that the velocity of a defect atom is not the velocity of any atom in the system, but the velocity of the dislocation it is tracking. Because the two measures, $V(t)$ and $\tilde{V}(t)$ are proportional to each other with the proportionality constant being the mean number of defect atoms sitting next to a dislocation, we can use the latter for convenience. Fig. 10.1 shows the typical time dependence of $N(t)$ from a simulation. $N(t)$ changes as dislocations are being created and annihilated. There are intermittent events of creation of dislocations, with number of dislocations involved ranging from a few to 100. Fig 10.2 shows the acoustic emission signal, $V(t)$, in the same simulation. Similar to $N(t)$, the signal ranges from 0 to 400, with intermittent pulses of various sizes.

In order to partition the signal into individual avalanches we apply a threshold, V_{thr}, to it for each temperature and shearing rate we simulate. The probability distribution of the avalanche size (also called activity fluctuations in the flowing state)

$$S = \int_{t_{\text{start}}}^{t_{\text{finish}}} V(t)dt, \tag{10.3}$$

duration

$$t_{\text{aval}} = t_{\text{finish}} - t_{\text{start}}, \tag{10.4}$$

and energy

$$E = \int_{t_{\text{start}}}^{t_{\text{finish}}} V^2(t)dt, \tag{10.5}$$

where t_{start} and t_{finish} are the starting and ending time of the event respectively, were then extracted. In

order to see the fluctuations that correspond to slip avalanches in addition to the effect of the shear rate we applied a threshold equal to the average of the signal in each realization of total time t_{total},

$$V_{\text{threshold}} = \frac{1}{t_{\text{total}}} \int_0^{t_{\text{total}}} V(t)dt, \tag{10.6}$$

For each shearing rate and temperature, 48 different realizations are run to obtain sufficient statistics. This results in tens of thousands of avalanche events for each shearing rate and temperature. In Fig. 10.3 we show the event size distribution for different temperatures at the same shearing rate. We find that the distribution follows a power law for small event sizes and cuts off at larger sizes, with the maximum avalanche size not exhibiting a strong dependence on temperature.

10.3 Scaling Behavior of the avalanches at Finite Temperature and Shear Rate

The probability distributions of the avalanche size, duration and energy shown in Fig. 10.3 are at the same shearing rate, $v_0 = 0.765$, and different temperature parameter values ϵ. In Fig. 10.4 we present the probability distributions of the avalanche size, duration, energy and average size versus duration are at the same temperature parameter values $\epsilon = 1.6$ and different shearing rates, v_0. Each curve is characterized by a power law for several decades and a cutoff at large values which does not depend strongly on temperature. The slip events distribute themselves according to power laws

$$D_S(S) \sim S^{-1.5}, \tag{10.7}$$

$$D_t(t_{\text{aval}}) \sim t_{\text{aval}}^{-2}, \tag{10.8}$$

$$D_E(E) \sim E^{-1.3}, \tag{10.9}$$

with critical exponents that are in agreement with the Mean Field interface depinning transition universality class (Table 7.1).

10.4 Discussion

Our results agree with the majority of the robust experimental and computational results in the literature. Richeton *et al.* [17] find $\kappa_E = 1.5$ for the energy distribution of acoustic emission while Dimiduk *et al.*

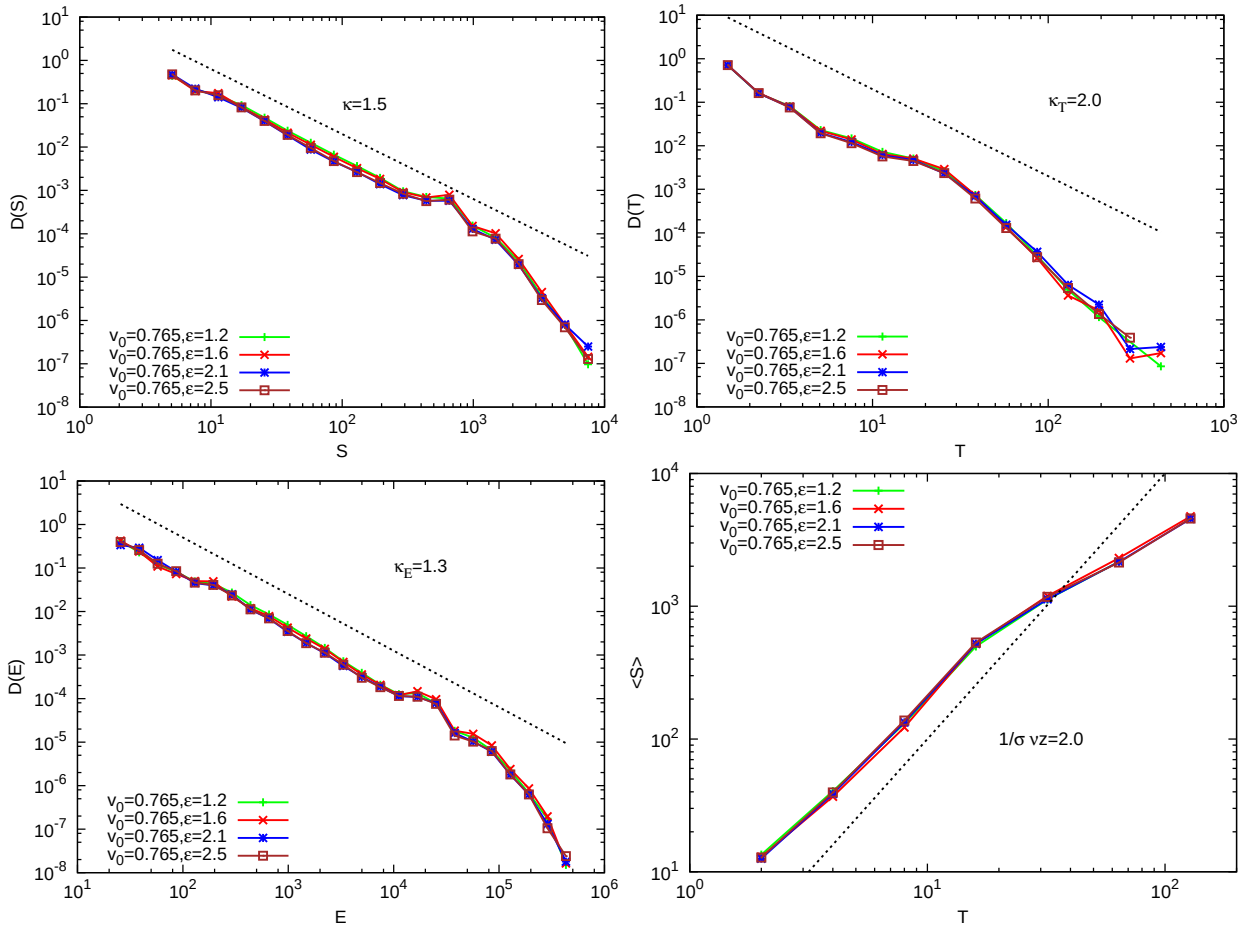

Figure 10.3: (color online) The probability distribution of the avalanche size (top left), the duration (top right), the energy (bottom left) and the average size versus duration of dislocation avalanches (bottom right), for different values of the temperature parameter at the same shearing rate. The probability distribution of the avalanche size of dislocation avalanches exhibits a power law of $\kappa \approx 1.5$, of durations of $\kappa_t \approx 2$ and of energies of $\kappa_E \approx 1.3$. The average size scales with the square of the duration, $1/\sigma\nu z \approx 2$. These results are in agreement with MFT (Table 7.1). The temperature range we used preserved the PFC crystal (did not melt it). (In producing these distributions we used logarithmic binning and ignored bins with only one count to avoid the trivial power law of $1/S$ that comes from normalizing the logarithmic bins with their size.)

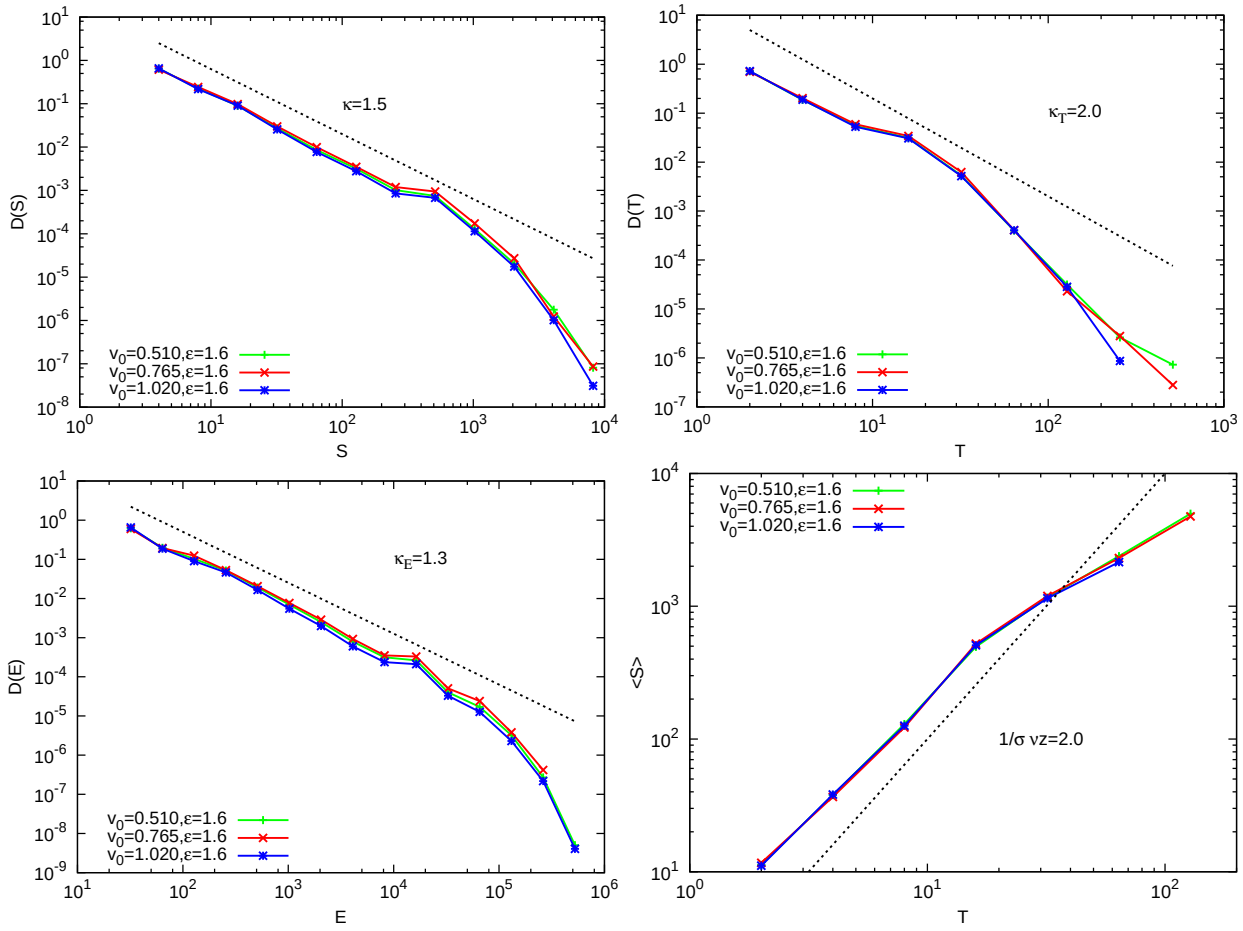

Figure 10.4: (color online) The probability distribution of the avalanche size (top left), the duration (top right), the energy (bottom left) and the average size versus duration of dislocation avalanches (bottom right), for different shearing rates at the same temperature. The probability distribution of the avalanche size of dislocation avalanches exhibits a power law of $\kappa \approx 1.5$, of durations of $\kappa_t \approx 2$ and of energies of $\kappa_E \approx 1.3$. The average size scales with the square of the duration, $1/\sigma\nu z \approx 2$. These results are in agreement with MFT (Table 7.1). (In producing these distributions we used logarithmic binning and ignored bins with only one count to avoid the trivial power law of $1/S$ that comes from normalizing the logarithmic bins with their size.)

reports $\kappa = 1.5 - 1.6$ in experiments at fixed compression stress that leads to shearing [4]. Similarly, for adiabatic stress increase in the pinned regime, Zaiser *et al.* finds $\kappa = 1.4$ [6, 51]. The distribution of energy amplitudes decays with the exponent $\kappa_E = 1.8$ [5] in simulations, and with $\kappa_E = 1.6$ in experiments [5]. Koslowski *et al.* employing a phase field (PF) model measured $\kappa_A = 1.8$ in simulations at fixed stress [12, 13].

Studies (including this work) at adiabatically slow shear rate have suggested analogies between plasticity and the interface depinning transition [1, 44]. Just as in the 2d DDD, we expect the upper critical dimension for the 2d PFC model to be the same and therefore mean field theory (MFT) is expected to give exact scaling results. The exponents we found are in excellent agreement with the mean field theory of the interface depinning universality class (see Table 7.1). At zero temperature the critical shear rate is $v_c = 0$. Our simulations, however, are performed at finite temperature $\epsilon \sim k_B T$. Temperature-induced dislocation creep causes the critical shear rate to appear to be nonzero in finite systems (see for example Fig. 5.2), with the apparent

$$v_c(\epsilon) \to 0 \quad \text{as} \quad \epsilon \to 0. \tag{10.10}$$

This causes the scaling distributions in Fig. 10.3 & 10.4 to be less precise and with more fluctuations than in zero temperature studies.

Chapter 11

Conclusion & Discussion

As the miniaturization trend in modern technological products progresses we need to know how materials deform on small scales. Experiments show that plasticity is an intermittent process in minute scales since one can sense the discreteness of the periodic crystal and, most importantly, the discontinuities of its periodicity. Crystalline materials on small scales deform intermittently-in-time and inhomogeneously-in-space. They exhibit a random sequence of slip events whose distribution shows power-law scaling. The dislocations interact with each other and demonstrate collective behavior. For applied stresses below the flow stress the dislocations are pinned/jammed and deformation proceeds with avalanches. For applied stresses above the flow stress the dislocations are mobile (depinned/unjammed) and the deforming body is constantly flowing. This behavior is characteristic of interfaces driven by an external force through a background of pinning centers. The phenomenon of plasticity can be studied as a depinning non-equilibrium phase transition.

Although initially ignored in deformation experiments, the jerky patterns of plasticity exhibit power law scaling. Initial indications were followed by a wealth of experiments in different materials, structures, and testing conditions. Studied sample sizes were pushed from mm [19] to μm [4] and all the way down to nm recently [21, 22]. The power laws are persistent and, remarkably, the same!

The exciting experimental evidence prompted a great deal of theoretical analysis. As a statistical physics problem a collection of dislocations is a non-trivial problem and has proven hard to solve analytically (at least for the time being). In order to solve the problem numerically several clever computational models were devised. Discrete dislocation dynamics and stochastic continuum models were able to reporduce the slip avalanche size distributions and give a first proof of the existence of a critical point [6]. Phase field models [13] also gave power law distributions.

However there were several open questions when we begum this work. Some studies of static properties seemed to exhibit mean field behavior. Other studies of dynamic properties showed non-mean-field behavior. The understanding of the apparent discrepancy was limited. In this Thesis we addressed a series of important open questions: If the dislocation interactions are long range then are the critical exponents mean field? What about the scaling functions? Is the scaling behavior mean field like both in the static properties and

the dynamical properties? How do the average temporal speed profiles of the slip avalanches look? Can we predict and test scaling functions in addition to the traditionally tested scaling exponents? What about finite-size effects?

In this study we undertook a considerable computational effort with an established model (DDD) at zero temperature and a newer model (PFC) at finite temperature. Besides reproducing the most reliable results in the literature we were able to answer several new questions and clarify and correct contradictory results in the literature. With the discrete dislocation dynamics (DDD) simulations at zero temperature we were able to extract the average temporal avalanche profiles. This constitutes the first test of a scaling function against MFT predictions. We showed that the corresponding universal exponents and scaling function agree with the scaling exponents of the power spectra and with mean field theory. These findings rectify previous results on the power spectra and avalanche profiles in the literature [8]. We were also successful in performing a finite-size scaling analysis extracting the critical exponent ν and calculating the depinning exponent β both in agreement with the MFT of interface depinning transition. In addition to the avalanche size distribution we were able to obtain the energy and the duration distributions, the latter from the phase field crystal (PFC) model.

There is still some work to be done to close this problem. The roughness exponent seems to disagree with the MFT of interface depinning most likely due to finite-size effects [1]. Also, what is the effect of temperature on the scaling behavior of plastically deformed systems? What is the thermal critical exponent? We are currently investigating the roughness with the DDD model and the temperature effects with the PFC model. We are planning to report results from these studies in the near future.

Appendix A

Details of the DDD Numerics

A.1 Lekner summation of images for the DDD

In this Section we derive the Lekner summation formula to account for the images and avoid edge effects in our simulation. We based our calculation on Lekner's ideas [46]. The interaction between dislocation i at (x_i, y_i) and dislocation j at (x_j, y_j) is given by

$$\tau_{\rm int}(\vec{r_i} - \vec{r_j}) = \sum_{\text{all images}} \frac{(x_i - x_j)[(x_i - x_j)^2 - (y_i - y_j)^2]}{[(x_i - x_j)^2 + (y_i - y_j)^2]^2} \tag{A.1}$$

We can reduce the x and y distances between the two dislocations within the basic simulation cell

$$x_i - x_j = \chi L \qquad y_i - y_j = \psi L \qquad |\chi|, |\psi| < 1 \tag{A.2}$$

The interaction stress when one accounts for an infinite number of image cells, $-\infty < l(m) < +\infty$, in $x(y)$ direction can be written as follows, making use of the reduced coordinates,

$$\tau(\chi, \psi) = \frac{1}{L} \sum_{l=-\infty}^{\infty} \sum_{m=-\infty}^{\infty} \frac{(\chi + l)[(\chi + l)^2 - (\psi + m)^2]}{[(\chi + l)^2 + (\psi + m)^2]^2} \tag{A.3}$$

What we have here is essentially two terms for which we need to perform a summation over an infinite number of image cells $l(m)$ in both, $x(y)$, directions. For each of the two terms there are two ways to simplify them using the Euler transformation, Eq. (A.35), the Poisson-Jacobi identities, Eqs. (A.40-A.43), and the integral representation of the Bessel K functions, Eq. (A.36). We calculate both Way I and Way II explicitly below. The two Ways are expected to be equivalent and they indeed yield similar results but not identical at least in their numerical evaluation. It turns out that Way I is better behaved numerically [1] and that's the one we used in the computer simulations.

[1] Way I is comprised of a single sum in contrast to Way II which is comprised of 2 sums and a continuous function and that makes Way I easier to deal with numerically although the 2 are mathematically equivalent.

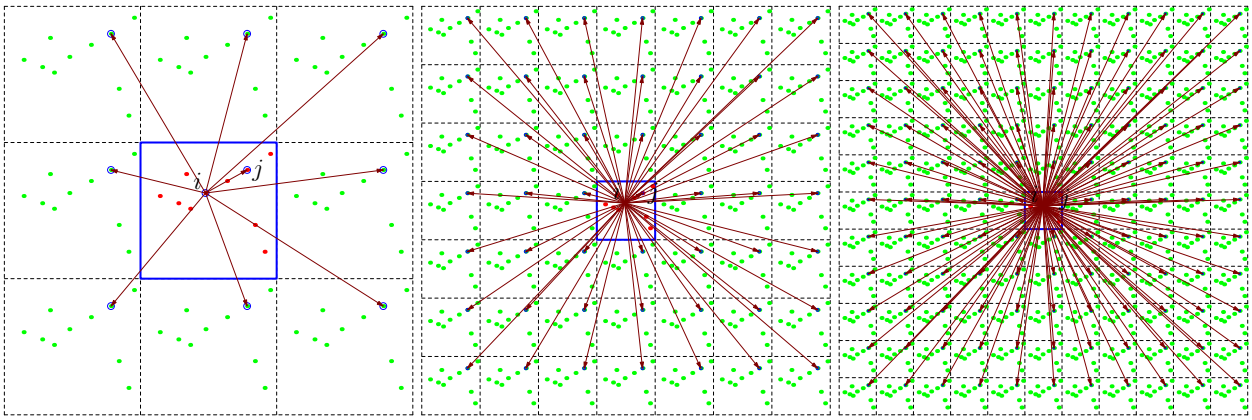

Figure A.1: (color online) Schematic of the Lekner summation method for the image cells. The basic simulation cell is drawn in blue and the image cells in black dashed dotted lines. The dislocations in the basic cell are in red and the image dislocations in green. The interaction pairs are shown with brown lines. Since periodic boundary conditions are needed to simulate behavior bigger than the basic cell, image cells are needed to be tiled around the basic simulation cell. The more image cells are used the higher the accuracy of the results. We used as many image cells as necessary in both directions to reach a relative accuracy of better than EPSILON $= 10^{-12}$ in the Lekner series. Image courtesy of Yang Liu.

A.1.1 Way I

For $\chi \neq 0$ we can use the Poisson-Jacobi identities to simplify expression A.3 according to Way I. First we make use of the Euler transformation, Eq. (A.35) for $\nu = 2$ to write,

$$\tau_I(\chi \neq 0, \psi) \equiv \frac{1}{L} \sum_{l=-\infty}^{\infty} \sum_{m=-\infty}^{\infty} \frac{(\chi+l)^3 - (\chi+l)(\psi+m)^2}{[(\chi+l)^2 + (\psi+m)^2]^2} \tag{A.4}$$

$$= \frac{1}{L} \sum_{l=-\infty}^{\infty} \sum_{m=-\infty}^{\infty} \left[(\chi+l)^3 - (\chi+l)(\psi+m)^2\right] \int_0^{\infty} dt t e^{-(\chi+l)^2 t - (\psi+m)^2 t} \tag{A.5}$$

$$= \frac{1}{L} \sum_{l=-\infty}^{\infty} (\chi+l)^3 \int_0^{\infty} dt t e^{-(\chi+l)^2 t} \sum_{m=-\infty}^{\infty} e^{-(\psi+m)^2 t}$$

$$-\frac{1}{L} \sum_{l=-\infty}^{\infty} (\chi+l) \int_0^{\infty} dt t e^{-(\chi+l)^2 t} \sum_{m=-\infty}^{\infty} (\psi+m)^2 e^{-(\psi+m)^2 t} \tag{A.6}$$

Then using the first, Eq. (A.40), and third Eq. (A.42) Poisson-Jacobi identities on the ψ term,

$$\tau_I(\chi \neq 0, \psi) = \frac{1}{L} \sum_{l=-\infty}^{\infty} \int_0^{\infty} dt t (\chi+l)^3 e^{-(\chi+l)^2 t} \frac{\pi^{\frac{1}{2}}}{t^{\frac{1}{2}}} \sum_{m=-\infty}^{\infty} e^{-\frac{\pi^2 m^2}{t}} \cos(2\pi m\psi)$$

$$-\frac{1}{L} \sum_{l=-\infty}^{\infty} (\chi+l) \int_0^{\infty} dt t e^{-(\chi+l)^2 t} \frac{1}{2} \frac{\pi^{\frac{1}{2}}}{t^{\frac{3}{2}}} \sum_{m=-\infty}^{+\infty} e^{-\frac{\pi^2 m^2}{t}} \cos(2\pi m\psi)$$

$$+\frac{1}{L} \sum_{l=-\infty}^{\infty} (\chi+l) \int_0^{\infty} dt t e^{-(\chi+l)^2 t} \frac{\pi^{\frac{5}{2}}}{t^{\frac{5}{2}}} \sum_{m=-\infty}^{+\infty} e^{-\frac{\pi^2 m^2}{t}} m^2 \cos(2\pi m\psi) \tag{A.7}$$

Rearranging and taking advantage of the fact that the expression is even in m to separate the sum to convenient partial sums

$$\begin{aligned}\tau_I(\chi\neq 0,\psi)=\frac{\pi^{\frac{1}{2}}}{L}\sum_{l=-\infty}^{\infty}\sum_{m=1}^{\infty}(\chi+l)^3\cos(2\pi m\psi)\int_0^{\infty}dtt^{\frac{1}{2}}e^{-(\chi+l)^2t}e^{-\frac{\pi^2m^2}{t}}\\ +\frac{\pi^{\frac{1}{2}}}{L}\sum_{l=-\infty}^{\infty}(\chi+l)^3\int_0^{\infty}dtt^{\frac{1}{2}}e^{-(\chi+l)^2t}\\ -\frac{\pi^{\frac{1}{2}}}{L}\sum_{l=-\infty}^{\infty}\sum_{m=1}^{+\infty}(\chi+l)\cos(2\pi m\psi)\int_0^{\infty}dtt^{-\frac{1}{2}}e^{-(\chi+l)^2t}e^{-\frac{\pi^2m^2}{t}}\\ +\frac{2\pi^{\frac{5}{2}}}{L}\sum_{l=-\infty}^{\infty}\sum_{m=1}^{+\infty}(\chi+l)m^2\cos(2\pi m\psi)\int_0^{\infty}dtt^{-\frac{3}{2}}e^{-(\chi+l)^2t}e^{-\frac{\pi^2m^2}{t}}\\ -\frac{\pi^{\frac{1}{2}}}{2L}\sum_{l=-\infty}^{\infty}(\chi+l)\int_0^{\infty}dtt^{-\frac{1}{2}}e^{-(\chi+l)^2t}\end{aligned}\tag{A.8}$$

Three of the integrals above are the Bessel $K_{\frac{1}{2}}$, Eq. (A.38), and $K_{\frac{3}{2}}$ Eq. (A.39) functions,

$$\begin{aligned}\tau_I(\chi\neq 0,\psi)=\frac{2\pi^{\frac{1}{2}}}{L}\sum_{l=-\infty}^{\infty}\sum_{m=1}^{\infty}(\chi+l)^3\cos(2\pi m\psi)2\left(\pi\left|\frac{m}{\chi+l}\right|\right)^{\frac{3}{2}}K_{\frac{3}{2}}(2\pi|m(\chi+l))\\ +\frac{\pi^{\frac{1}{2}}}{L}\sum_{l=-\infty}^{\infty}(\chi+l)^3\frac{\Gamma(\frac{3}{2})}{[(\chi+l)^2]^{\frac{3}{2}}}\\ -\frac{\pi^{\frac{1}{2}}}{L}\sum_{l=-\infty}^{\infty}\sum_{m=1}^{+\infty}(\chi+l)\cos(2\pi m\psi)2\left(\pi\left|\frac{m}{\chi+l}\right|\right)^{\frac{1}{2}}K_{\frac{1}{2}}(2\pi|m(\chi+l)|)\\ +\frac{2\pi^{\frac{5}{2}}}{L}\sum_{l=-\infty}^{\infty}\sum_{m=1}^{+\infty}(\chi+l)m^2\cos(2\pi m\psi)2\left(\pi\left|\frac{m}{\chi+l}\right|\right)^{-\frac{1}{2}}K_{\frac{1}{2}}(2\pi|m(\chi+l)|)\\ -\frac{\pi^{\frac{1}{2}}}{2L}\sum_{l=-\infty}^{\infty}(\chi+l)\frac{\Gamma(\frac{1}{2})}{[(\chi+l)^2]^{\frac{1}{2}}}\end{aligned}\tag{A.9}$$

and substituting for them gives,

$$\begin{aligned}\tau_I(\chi\neq 0,\psi)=\frac{4\pi^2}{L}\sum_{l=-\infty}^{\infty}\sum_{m=1}^{\infty}(\chi+l)^3\cos(2\pi m\psi)\left|\frac{m}{\chi+l}\right|^{\frac{3}{2}}\sqrt{\frac{\pi}{2}}\frac{e^{-2\pi|m(\chi+l)|}}{\sqrt{2\pi|m(\chi+l)|}}\frac{(1+2\pi|m(\chi+l)|)}{2\pi|m(\chi+l)|}\\ +\frac{\pi^{\frac{1}{2}}}{L}\sum_{l=-\infty}^{\infty}(\chi+l)^3\frac{\frac{\sqrt{\pi}}{2}}{[(\chi+l)^2]^{\frac{3}{2}}}\\ -\frac{2\pi}{L}\sum_{l=-\infty}^{\infty}\sum_{m=1}^{+\infty}(\chi+l)\cos(2\pi m\psi)\left|\frac{m}{\chi+l}\right|^{\frac{1}{2}}\sqrt{\frac{\pi}{2}}\frac{e^{-2\pi|m(\chi+l)|}}{\sqrt{2\pi|m(\chi+l)|}}\\ +\frac{4\pi^2}{L}\sum_{l=-\infty}^{\infty}\sum_{m=1}^{+\infty}(\chi+l)m^2\cos(2\pi m\psi)\left|\frac{\chi+l}{m}\right|^{\frac{1}{2}}\sqrt{\frac{\pi}{2}}\frac{e^{-2\pi|m(\chi+l)|}}{\sqrt{2\pi|m(\chi+l)|}}\end{aligned}$$

$$-\frac{\pi^{\frac{1}{2}}}{2L}\sum_{l=-\infty}^{\infty}(\chi+l)\frac{\sqrt{\pi}}{[(\chi+l)^2]^{\frac{1}{2}}} \tag{A.10}$$

$$\begin{aligned}
&= \frac{\pi}{L}\sum_{l=-\infty}^{\infty}\sum_{m==1}^{\infty}\frac{(\chi+l)^3}{|\chi+l|^3}\cos(2\pi m\psi)e^{-2\pi|m(\chi+l)|}(1+2\pi|m(\chi+l)|) \\
&\quad +\frac{\pi}{2L}\sum_{l=-\infty}^{\infty}\frac{(\chi+l)^3}{|\chi+l|^3} \\
&\quad -\frac{\pi}{L}\sum_{l=-\infty}^{\infty}\sum_{m=1}^{+\infty}\frac{\chi+l}{|\chi+l|}\cos(2\pi m\psi)e^{-2\pi|m(\chi+l)|} \\
&\quad +\frac{2\pi^2}{L}\sum_{l=-\infty}^{\infty}\sum_{m=1}^{+\infty}(\chi+l)\frac{m^2}{|m|}\cos(2\pi m\psi)e^{-2\pi|m(\chi+l)|} \\
&\quad -\frac{\pi}{2L}\sum_{l=-\infty}^{\infty}\frac{\chi+l}{|\chi+l|}
\end{aligned} \tag{A.11}$$

$$\begin{aligned}
&= \frac{\pi}{L}\sum_{l=-\infty}^{\infty}\sum_{m=1}^{\infty}\mathrm{sgn}(\chi+l)\cos(2\pi m\psi)e^{-2\pi|m(\chi+l)|}(1+2\pi|m(\chi+l)|) \\
&\quad +\frac{\pi}{2L}\sum_{l=-\infty}^{\infty}\mathrm{sgn}(\chi+l) \\
&\quad -\frac{\pi}{L}\sum_{l=-\infty}^{\infty}\sum_{m=1}^{+\infty}\mathrm{sgn}(\chi+l)\cos(2\pi m\psi)e^{-2\pi|m(\chi+l)|} \\
&\quad +\frac{2\pi^2}{L}\sum_{l=-\infty}^{\infty}\sum_{m=1}^{+\infty}(\chi+l)|m|\cos(2\pi m\psi)e^{-2\pi|m(\chi+l)|} \\
&\quad -\frac{\pi}{2L}\sum_{l=-\infty}^{\infty}\mathrm{sgn}(\chi+l)
\end{aligned} \tag{A.12}$$

The result is

$$\tau_I(\chi\neq 0,\psi) = \frac{4\pi^2}{L}\sum_{l=-\infty}^{\infty}\sum_{m=1}^{+\infty}(\chi+l)m\cos(2\pi m\psi)e^{-2\pi|m(\chi+l)|} \tag{A.13}$$

For $\chi = 0$ and $\psi \neq 0$ we have,

$$\tau_I(\chi=0,\psi\neq 0) = \frac{1}{L}\sum_{l=-\infty}^{\infty}\sum_{m=-\infty}^{\infty}l\frac{l^2-(\psi+m)^2}{[l^2+(\psi+m)^2]^2} \tag{A.14}$$

$$\begin{aligned}
&= \frac{4\pi^2}{L}\sum_{l=-\infty,\neq 0}^{\infty}\sum_{m=1}^{+\infty}lm\cos(2\pi m\psi)e^{-2\pi|ml|} \\
&\quad +\frac{1}{L}\sum_{m=-\infty}^{\infty}l\frac{l^2-(\psi+m)^2}{[l^2+(\psi+m)^2]^2}\bigg|_{l=0} \\
&\quad +\frac{1}{L}\sum_{l=-\infty,\neq 0}^{\infty}l\frac{l^2-(\psi+m)^2}{[l^2+(\psi+m)^2]^2}\bigg|_{m=0}
\end{aligned} \tag{A.15}$$

$$= 0 + 0 + 0 \tag{A.16}$$

which is symmetrically zero for all y's at $x = 0$. The expression in Eq. (A.13) already contains this information, i.e. gives zero for $\chi = 0$.

Way I gives a compact, quickly convergent sum due to the exponential that is very useful for the numerical evaluation of the interaction properly taking into account the image cells and avoiding discontinuity problems that can arise because of the periodic boundary conditions. Expression A.13 is antisymmetric with respect to χ (x) and symmetric with respect to ψ (y) just like the interaction expression without any images Eq. (A.1). Way I, Eq. (A.13), is depicted in Fig. A.2.

A.1.2 Way II

For $\psi \neq 0$ we can use the Poisson-Jacobi identities to simplify the expression Eq. (A.3) according to Way II. First we make use of the Euler transformation, Eq. (A.35) for $\nu = 2$ to write,

$$\tau_{II}(\chi, \psi \neq 0) \equiv \frac{1}{L} \sum_{l=-\infty}^{\infty} \sum_{m=-\infty}^{\infty} \frac{(\chi+l)^3 - (\chi+l)(\psi+m)^2}{[(\chi+l)^2 + (\psi+m)^2]^2} \tag{A.17}$$

$$= \frac{1}{L} \sum_{l=-\infty}^{\infty} \sum_{m=-\infty}^{\infty} [(\chi+l)^3 - (\chi+l)(\psi+m)^2] \int_0^{\infty} dt t e^{-(\chi+l)^2 t - (\psi+m)^2 t} \tag{A.18}$$

$$= \frac{1}{L} \sum_{m=-\infty}^{\infty} \int_0^{\infty} dt t e^{-(\psi+m)^2 t} \sum_{l=-\infty}^{\infty} (\chi+l)^3 e^{-(\chi+l)^2 t}$$

$$- \frac{1}{L} \sum_{m=-\infty}^{\infty} (\psi+m)^2 \int_0^{\infty} dt t e^{-(\psi+m)^2 t} \sum_{l=-\infty}^{\infty} (\chi+l) e^{-(\chi+l)^2 t} \tag{A.19}$$

Then using the second, Eq. (A.41), and fourth, Eq. (A.43), Poisson-Jacobi identity on the χ terms,

$$\tau_{II}(\chi, \psi \neq 0) = \frac{1}{L} \sum_{m=-\infty}^{\infty} \int_0^{\infty} dt t e^{-(\psi+m)^2 t} \sum_{l=-\infty}^{+\infty} \left[\frac{3}{2} \frac{\pi^{\frac{3}{2}}}{t^{\frac{5}{2}}} e^{-\frac{\pi^2 l^2}{t}} l \sin(2\pi l \chi) - \frac{\pi^{\frac{7}{2}}}{t^{\frac{7}{2}}} e^{-\frac{\pi^2 l^2}{t}} l^3 \sin(2\pi l \chi) \right]$$

$$- \frac{1}{L} \sum_{m=-\infty}^{\infty} (\psi+m)^2 \int_0^{\infty} dt t e^{-(\psi+m)^2 t} \frac{\pi^{\frac{3}{2}}}{t^{\frac{3}{2}}} \sum_{l=-\infty}^{+\infty} e^{-\frac{\pi^2 l^2}{t}} l \sin(2\pi l \chi) \tag{A.20}$$

$$= \frac{3\pi^{\frac{3}{2}}}{L} \sum_{l=1}^{+\infty} \sum_{m=-\infty}^{\infty} l \sin(2\pi l \chi) \int_0^{\infty} dt t^{-\frac{3}{2}} e^{-(\psi+m)^2 t} e^{-\frac{\pi^2 l^2}{t}}$$

$$- \frac{2\pi^{\frac{7}{2}}}{L} \sum_{l=1}^{+\infty} \sum_{m=-\infty}^{\infty} l^3 \sin(2\pi l \chi) \int_0^{\infty} dt t^{-\frac{5}{2}} e^{-(\psi+m)^2 t} e^{-\frac{\pi^2 l^2}{t}}$$

$$- \frac{2\pi^{\frac{3}{2}}}{L} \sum_{l=1}^{+\infty} \sum_{m=-\infty}^{\infty} (\psi+m)^2 l \sin(2\pi l \chi) \int_0^{\infty} dt t^{-\frac{1}{2}} e^{-(\psi+m)^2 t} e^{-\frac{\pi^2 l^2}{t}} \tag{A.21}$$

Substituting for the Bessel K functions, Eq. (A.38) and Eq. (A.39), wherever possible,

$$\begin{aligned}
\tau_{II}(\chi,\psi\neq 0) &= \frac{3\pi^{\frac{3}{2}}}{L}\sum_{l=1}^{+\infty}\sum_{m=-\infty}^{+\infty} l\sin(2\pi l\chi)2\left(\pi\left|\frac{l}{\psi+m}\right|\right)^{-\frac{1}{2}} K_{\frac{1}{2}}(2\pi|l(\psi+m)|)\\
&\quad -\frac{2\pi^{\frac{7}{2}}}{L}\sum_{l=1}^{+\infty}\sum_{m=-\infty}^{\infty} l^3\sin(2\pi l\chi)2\left(\pi\left|\frac{l}{\psi+m}\right|\right)^{-\frac{3}{2}} K_{\frac{3}{2}}(2\pi|l(\psi+m)|)\\
&\quad -\frac{2\pi^{\frac{3}{2}}}{L}\sum_{l=1}^{+\infty}\sum_{m=-\infty}^{\infty} (\psi+m)^2 l\sin(2\pi l\chi)2\left(\pi\left|\frac{l}{\psi+m}\right|\right)^{\frac{1}{2}} K_{\frac{1}{2}}(2\pi|l(\psi+m)|) \qquad \text{(A.22)}\\
&= \frac{6\pi}{L}\sum_{l=1}^{+\infty}\sum_{m=-\infty}^{+\infty} l\sin(2\pi l\chi)\left(\left|\frac{\psi+m}{l}\right|\right)^{\frac{1}{2}}\sqrt{\frac{\pi}{2}}\frac{e^{-2\pi|l(\psi+m)|}}{\sqrt{2\pi|l(\psi+m)|}}\\
&\quad -\frac{4\pi^2}{L}\sum_{l=1}^{+\infty}\sum_{m=-\infty}^{\infty} l^3\sin(2\pi l\chi)\left(\left|\frac{\psi+m}{l}\right|\right)^{\frac{3}{2}}\sqrt{\frac{\pi}{2}}\frac{e^{-2\pi|l(\psi+m)|}}{\sqrt{2\pi|l(\psi+m)|}}\frac{1+2\pi|l(\psi+m)|}{2\pi|l(\psi+m)|}\\
&\quad -\frac{4\pi^2}{L}\sum_{l=1}^{+\infty}\sum_{m=-\infty}^{\infty} (\psi+m)^2 l\sin(2\pi l\chi)\left(\left|\frac{l}{\psi+m}\right|\right)^{\frac{1}{2}}\sqrt{\frac{\pi}{2}}\frac{e^{-2\pi|l(\psi+m)|}}{\sqrt{2\pi|l(\psi+m)|}} \qquad \text{(A.23)}\\
&= \frac{3\pi}{L}\sum_{l=1}^{+\infty}\sum_{m=-\infty}^{+\infty}\frac{l}{|l|}\sin(2\pi l\chi)e^{-2\pi|l(\psi+m)|}\\
&\quad -\frac{\pi}{L}\sum_{l=1}^{+\infty}\sum_{m=-\infty}^{\infty}\frac{l^3}{|l|^3}\sin(2\pi l\chi)e^{-2\pi|l(\psi+m)|}(1+2\pi|l(\psi+m)|)\\
&\quad -\frac{2\pi^2}{L}\sum_{l=1}^{+\infty}\sum_{m=-\infty}^{\infty}\frac{(\psi+m)^2}{|\psi+m|}l\sin(2\pi l\chi)e^{-2\pi|l(\psi+m)|} \qquad \text{(A.24)}\\
&= \frac{3\pi}{L}\sum_{l=1}^{+\infty}\sum_{m=-\infty}^{+\infty}\mathrm{sgn}(l)\sin(2\pi l\chi)e^{-2\pi|l(\psi+m)|}\\
&\quad -\frac{\pi}{L}\sum_{l=1}^{+\infty}\sum_{m=-\infty}^{\infty}\mathrm{sgn}(l)\sin(2\pi l\chi)e^{-2\pi|l(\psi+m)|}(1+2\pi|l(\psi+m)|)\\
&\quad -\frac{2\pi^2}{L}\sum_{l=1}^{+\infty}\sum_{m=-\infty}^{\infty} l|\psi+m|\sin(2\pi l\chi)e^{-2\pi|l(\psi+m)|} \qquad \text{(A.25)}
\end{aligned}$$

The result is

$$\tau_{II}(\chi,\psi\neq 0) = \frac{2\pi}{L}\sum_{l=1}^{+\infty}\sum_{m=-\infty}^{+\infty}\sin(2\pi l\chi)e^{-2\pi|l(\psi+m)|}(1-2\pi l|\psi+m|) \qquad \text{(A.26)}$$

which is identically zero for $x=0$ for all y's.

For $\chi\neq 0$ and $\psi=0$ we have

$$\tau_{1II}(\chi\neq 0,\psi=0) = \frac{1}{L}\sum_{l=-\infty}^{\infty}\sum_{m=-\infty}^{\infty}\frac{(\chi+l)^3-(\chi+l)m^2}{[(\chi+l)^2+m^2]^2} \qquad \text{(A.27)}$$

$$= \frac{2\pi}{L}\sum_{l=1}^{+\infty}\sum_{m=-\infty,\neq 0}^{+\infty}\sin(2\pi l\chi)e^{-2\pi|lm)|}(1-2\pi l|m|) + \frac{1}{L}\sum_{l=-\infty}^{+\infty}\frac{1}{\chi+l}\Bigg|_{m=0} \tag{A.28}$$

$$= \frac{2\pi}{L}\sum_{l=1}^{+\infty}\sum_{m=-\infty,\neq 0}^{+\infty}\sin(2\pi l\chi)e^{-2\pi|lm|}(1-2\pi|lm|) + \frac{\pi}{L}\cot(\pi\chi) \tag{A.29}$$

where in the last line we used the Mittag-Leffler expansion of the cotangent, Eq. (A.44).

Way II, Eq. (A.26) and Eq. (A.29), gives a little less compact way of calculating the interaction with images than Way I, Eq. (A.13). At first look this may seem not obvious because Way II still carries the rapidly convergent exponentials as Way II. This salient difference lies in the fact that Way I is a single sum while Way II has two separate sums and a continuous term (the cot is a sum that is already performed for infinite number of terms). Nevertheless Way II exhibits the same quick convergence (due to the exponentials) and symmetries as Way I, Eq. (A.13) and can be used provided special care is taken for convergence during evaluation. The combined expression of Way II, from Eq. (A.26) and Eq. (A.29), is depicted in Fig. A.3.

A.1.3 Self-Energy

If two dislocations occupy the same space (location) then their interaction diverges. In the image summation we need to account for the interactions of particle i with all its images (self-energy) and not count the interaction with its own self. That is the case for $\chi = 0$ and $\psi = 0$ where the term $l = 0, m = 0$ is explicitly excluded. This summation is denoted by

$$\left(\sum_{l=-\infty}^{+\infty}\sum_{m=-\infty}^{+\infty}\right)' \equiv \sum_{l=-\infty}^{+\infty}\sum_{m=-\infty}^{+\infty} -(l=0, m=0 \text{ term}) \tag{A.30}$$

In our case we have,

$$\tau_I(\chi=0,\psi=0) = \frac{1}{L}\left(\sum_{l=-\infty}^{\infty}\sum_{m=-\infty}^{\infty}\right)' l\frac{l^2-m^2}{[l^2+m^2]^2} \tag{A.31}$$

$$= \frac{2}{L}\sum_{l=-\infty}^{\infty}\sum_{m=1}^{\infty} l\frac{l^2-m^2}{[l^2+m^2]^2} + \frac{1}{L}\sum_{l=-\infty,\neq 0}^{\infty}\frac{1}{l} \tag{A.32}$$

$$= 0 \tag{A.33}$$

Obviously the $l = 0, m = 0$ term diverges,

$$(l = 0, m = 0 \text{ term}) = \frac{1}{L}\frac{1}{l}\bigg|_{l\to 0} \to \infty \tag{A.34}$$

as one would expect from the expression of the interaction without images, Eq. (A.1).

A.1.4 Euler Transformation

The Euler transformation is,

$$\frac{1}{x^\nu} = \frac{1}{\Gamma(\nu)}\int_0^\infty dt \cdot t^{\nu-1}e^{-xt} \qquad (\nu > 0) \tag{A.35}$$

where $\Gamma(\nu)$ is the Gamma function. It allows us to convert fractions into integral expressions that can be transformed (with the help of Eq. (A.36)) to quickly decaying Bessel functions.

A.1.5 Bessel K function Integral Representation

The Bessel K function can be represented by an integral,

$$\int_0^\infty dt \cdot t^{\nu-1}e^{-\frac{\pi^2 l^2}{t} - m^2 t} = 2\left(\pi\left|\frac{l}{m}\right|\right)^\nu K_\nu(2\pi|lm|)) \tag{A.36}$$

Also the Bessel K functions are even with respect to their order,

$$K_\nu(z) = K_{-\nu}(z) \tag{A.37}$$

The Bessel K functions we are going to need here are,

$$K_{\frac{1}{2}}(z) = \sqrt{\frac{\pi}{2}}\frac{e^{-z}}{\sqrt{z}} \tag{A.38}$$

$$K_{\frac{3}{2}}(z) = \sqrt{\frac{\pi}{2}}\frac{e^{-z}}{\sqrt{z}}\left(1 + \frac{1}{z}\right) \tag{A.39}$$

These fractional Bessel K function are easy to use because they can be written in closed form with well-behaved, fast decaying exponentials.

A.1.6 Poisson-Jacobi Identities

The Poisson-Jacobi identities are very useful in transforming the integrals from the Lekner summation to accept converging Bessel function through their integral representation (shown just above).

$$\sum_{l=-\infty}^{+\infty} e^{-(\chi+l)^2 t} = \frac{\pi^{\frac{1}{2}}}{t^{\frac{1}{2}}} \sum_{l=-\infty}^{+\infty} e^{-\frac{\pi^2 l^2}{t}} \cos(2\pi l\chi) \tag{A.40}$$

Taking the 1st derivative over χ, $\frac{d}{d\chi}$,

$$\begin{aligned} \frac{d}{d\chi} \sum_{l=-\infty}^{+\infty} e^{-(\chi+l)^2 t} &= \frac{d}{d\chi} \frac{\pi^{\frac{1}{2}}}{t^{\frac{1}{2}}} \sum_{l=-\infty}^{+\infty} e^{-\frac{\pi^2 l^2}{t}} \cos(2\pi l\chi) \\ \sum_{l=-\infty}^{+\infty} (\chi+l) e^{-(\chi+l)^2 t} &= \frac{\pi^{\frac{3}{2}}}{t^{\frac{3}{2}}} \sum_{l=-\infty}^{+\infty} e^{-\frac{\pi^2 l^2}{t}} \cdot l \cdot \sin(2\pi l\chi) \end{aligned} \tag{A.41}$$

Taking the 2nd derivative over χ,

$$\sum_{l=-\infty}^{+\infty} (\chi+l)^2 e^{-(\chi+l)^2 t} = \frac{1}{2} \frac{\pi^{\frac{1}{2}}}{t^{\frac{3}{2}}} \sum_{l=-\infty}^{+\infty} e^{-\frac{\pi^2 l^2}{t}} \cos(2\pi l\chi) - \frac{\pi^{\frac{5}{2}}}{t^{\frac{5}{2}}} \sum_{l=-\infty}^{+\infty} e^{-\frac{\pi^2 l^2}{t}} \cdot l^2 \cdot \cos(2\pi l\chi) \tag{A.42}$$

Taking the 3rd derivative over χ,

$$\sum_{l=-\infty}^{+\infty} (\chi+l)^3 e^{-(\chi+l)^2 t} = \frac{3}{2} \frac{\pi^{\frac{3}{2}}}{t^{\frac{5}{2}}} \sum_{l=-\infty}^{+\infty} e^{-\frac{\pi^2 l^2}{t}} \cdot l \cdot \sin(2\pi l\chi) - \frac{\pi^{\frac{7}{2}}}{t^{\frac{7}{2}}} \sum_{l=-\infty}^{+\infty} e^{-\frac{\pi^2 l^2}{t}} \cdot l^3 \cdot \sin(2\pi l\chi) \tag{A.43}$$

A.1.7 Mittag-Leffler expansion of cotangent

$$\sum_{l=-\infty}^{+\infty} \frac{1}{z+l} = \pi \cot(\pi z) \tag{A.44}$$

A.2 Evaluation of the Lekner series; Convergence criteria

The Lekner formalism is particularly elegant and powerful because of the fast decaying Bessel functions. In the case at hand of the DDD interaction it is very convenient to have Bessel functions for which an analytic form exists and converges rapidly, like the exponential e^{-z}. Naively thinking one may want to numerically evaluate the sum up to some truncation cutoff parameter values, e.g. n_l and n_m,

$$\tau_I(\chi \neq 0, \psi) = \frac{4\pi^2}{L} \sum_{l=-n_l}^{+n_l} \sum_{m=1}^{+n_m} (\chi+l) m \cos(2\pi m\psi) e^{-2\pi|m(\chi+l)|} \tag{A.45}$$

$$\tau_I(\chi = 0, \psi \neq 0) = 0 \tag{A.46}$$

or

$$\tau_{II}(\chi, \psi \neq 0) = \frac{2\pi}{L} \sum_{l=1}^{+n_l} \sum_{m=-n_m}^{+n_m} \sin(2\pi l\chi) e^{-2\pi|l(\psi+m)|}(1 - 2\pi l|\psi + m|) \tag{A.47}$$

$$\tau_{II}(\chi \neq 0, \psi = 0) = \frac{2\pi}{L} \sum_{l=1}^{+n_l} \sum_{m=-n_m, \neq 0}^{+n_m} \sin(2\pi l\chi) e^{-2\pi|lm|}(1 - 2\pi l|m|) + \frac{\pi}{L}\cot(\pi\chi) \tag{A.48}$$

This may introduce a bias and yield very different numerical results unless one makes sure that the series has converged (e.g. [75]). In our implementation we truncated the series when the absolute value of the last term was within a very low precision relative to the absolute value of the sum of all the previous terms. For our double sums the convergence scheme we applied was:

$$g(1) = \sum_{l=-1}^{1} f(l, 1) \quad \text{for} \quad n = 1 \tag{A.49}$$

$$g(n) = \sum_{m=1}^{n-1} f(l = n, m) + \sum_{m=1}^{n-1} f(l = -n, m) + \sum_{l=-n}^{n} f(l, m = n) \quad \text{for} \quad n > 1 \tag{A.50}$$

$$\text{if} \quad \left|g(n+1)\right| < \text{EPSILON} \times \left| \sum_{m=1}^{+n} \sum_{l=-n}^{+n} f(l, m) \right| \quad \text{then} \quad \text{stop} \tag{A.51}$$

$$\text{else} \quad n = n + 1 \quad \text{and} \quad \text{check} \quad \text{again} \tag{A.52}$$

In other words, we sum the terms of the next shell in (l, m), i.e. $g(n+1)$ and compare it to the sum so far $|\sum_{m=1}^{+n}\sum_{l=-n}^{+n} f(l, m)|$. If the next term $g(n+1)$ to be added to the series is relatively smaller than the set precision (we chose EPSILON $= 10^{-12}$)[2] the series has converged. Otherwise we repeat the process onto the next shell and until the series has converged.

In addition we imposed another convergence criterion by making sure that the exponential had converged to a very tiny value similar to the series,

$$z > 28 \quad \rightarrow \quad e^{-z} = 6.91 \times 10^{-13} < 10^{-12} = \text{EPSILON} \tag{A.53}$$

In our case the first convergence criterion on the truncation of the series is always more restrictive than the second convergence criterion on the exponential. However it is good practice to include both.[3]

[2] We picked EPSILON to be close enough but not better than the precision of a double in our computer architecture which was approximately 10^{-14}.

[3] In the general case where our Lekner sums contain Bessel functions without an analytic form, the application of the second convergence criterion on the argument of the Bessel function becomes: e.g. $z > 35 \quad \rightarrow \quad K_1(z) < 1.35 \times 10^{-16}$.

The two Ways of carrying out the summation of the series converge to the same results for different total number of images (n's) in general. Lastly, the trigonometric terms oscillate rapidly for different values of l and m and may give a value very close to zero indicating false convergence before the series has converged itself. Therefore it is better to check the convergence of the series without the trigonometric terms first, find the appropriate n's and then sum the series up to those n's including the sines and cosines.

A.3 Numerical Implementation of the Interaction

Calculating several terms of the Lekner sums for each dislocation pair at every timestep of the simulation during runtime (on the fly) is very demanding on the CPU. In every time step of a run with N dislocations the number of operations is proportional to N^2 FLOPS [4]. This was very time consuming so we decided to calculate the interaction for a sufficient number of possible pair distances and store them in a look-up table. During runtime we load the look-up table on to the RAM. At every timestep and for every dislocation pair we "look-up" the stress values at the nearest distance values and interpolate to find the interaction stress at the distance of interest.

Because the dislocations are placed on planes at integer values of y the integers $y = 0, 1, 2...L/2$ give exact and unique (due to the symmetry of the Lekner summation) interaction stress values. In other words no interpolation was performed along the y-direction. On the other hand, the dislocations are allowed to exist at any real x so the density of exact interaction stress values to store in the look-up is a parameter we need to optimize for a succesful interpolation scheme. The minimum number of points we considered in the x-axis was the integers (like in the y case) $x = 0, 1, 2...L/2$. From then on we increased the density of points which we declared as 1/fac. Considering only the integers (like just above) translates to 1/fac = 1. For fac = 2 we added one more x-point for every integer x, $x = 0, 0.5, 1, 1.5, 2...L/2$. For fac = 5 we added four more x-points for every integer x, $x = 0, 0.2, 0.4, 0.6, 0.8, 1, ...L/2$ and so on. This means that we have $L/2 + 1$ y distances and fac $\cdot\, L/2 + 1$ x distances. In total our look-up table has (fac $\cdot\, L/2 + 1) \times (L/2 + 1)$ entries.

The total relative error of n-th order polynomial interpolation is proportional to the distance between the points where the interaction is known to the next power of $n + 1$. For a spatial resolution of fac this translates to the total relative error between the interaction stress as calculated from the Lekner sum and the interpolated interaction from the Lekner interaction stress at neighboring points that are 1/fac apart to

[4] N dislocations form $\frac{N(N-1)}{2}$ pairs

scale as,

$$\text{TOTAL RELATIVE ERROR(fac)} \sim \left(1/\text{fac}\right)^{n+1}. \tag{A.54}$$

We calculated the total error

$$\text{TOTAL RELATIVE ERROR(fac)} = \sqrt{\frac{\sum_{x_i=0}^{200\cdot L/2}\sum_{j=0}^{L/2}\left(\tau_{\text{interpolated}}(x_i,j)-\tau(x_i,j)\right)^2}{\sum_{x_i=0}^{200\cdot L/2}\sum_{j=1}^{L/2}\tau(x_i,j)^2}} \tag{A.55}$$

for several different spatial resolution in x fac $= 1, 2, 5, 10, 20, 50, 100$ and plot it in Fig. A.4. The scaling jumps right out of the figure. The x points on which we performed the sum for the calculation of the total relative error where $x_i = 0, 0.005, 0.001, 0.0015, ...L/2$, i.e. the $200 \cdot L/2+1$ points that fac $= 200$ would give.

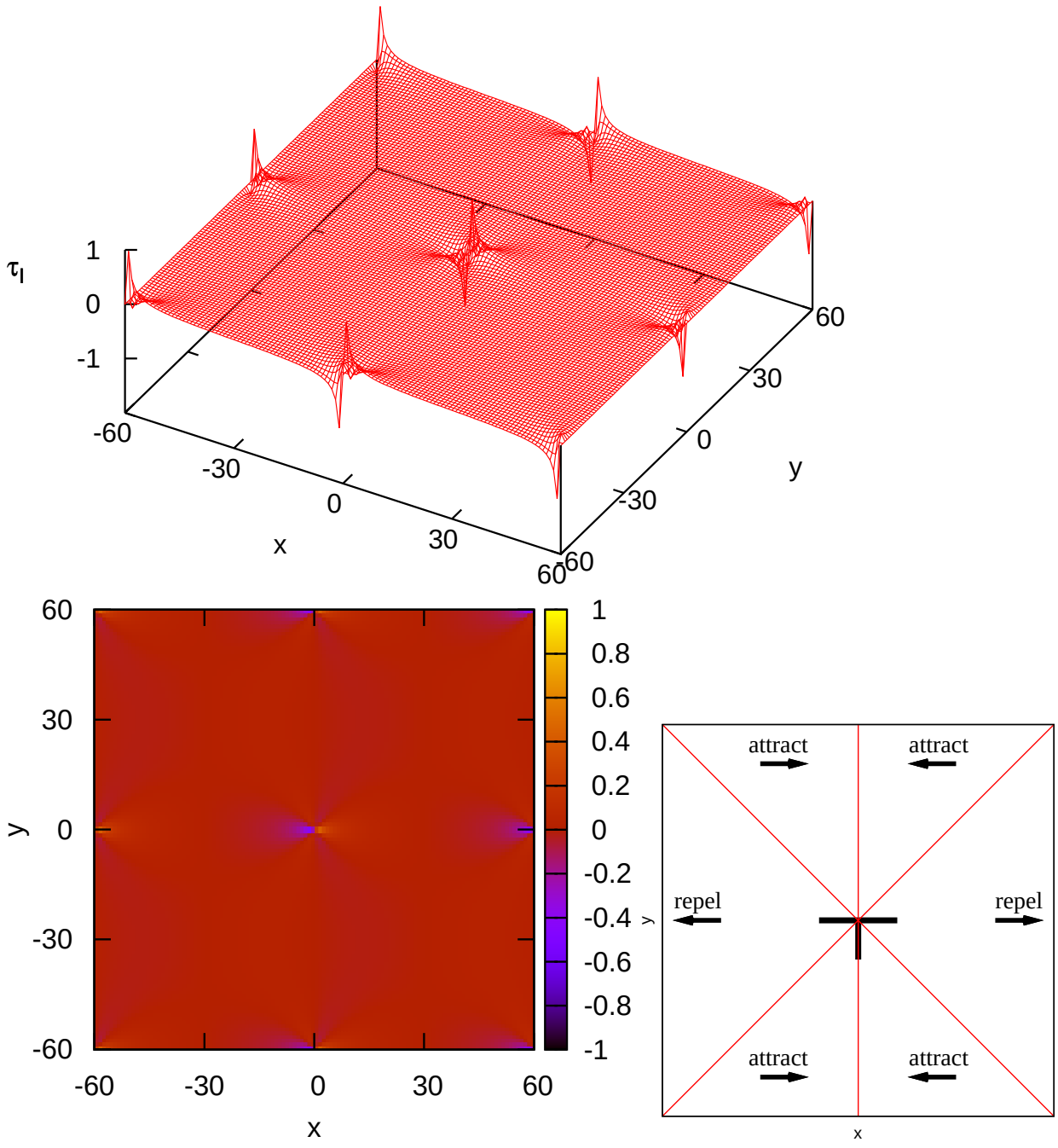

Figure A.2: (color online) The result of the converged Lekner series according to Way I (Eq. A.13) for a small system of $L = 60$. It is depicted as a surface plot (top) and as a color contour plot (bottom left). The anisotropy of the interaction is indicated bottom right. In order to reveal its anisotropy Way I is plotted in an area of $2L \times 2L$.

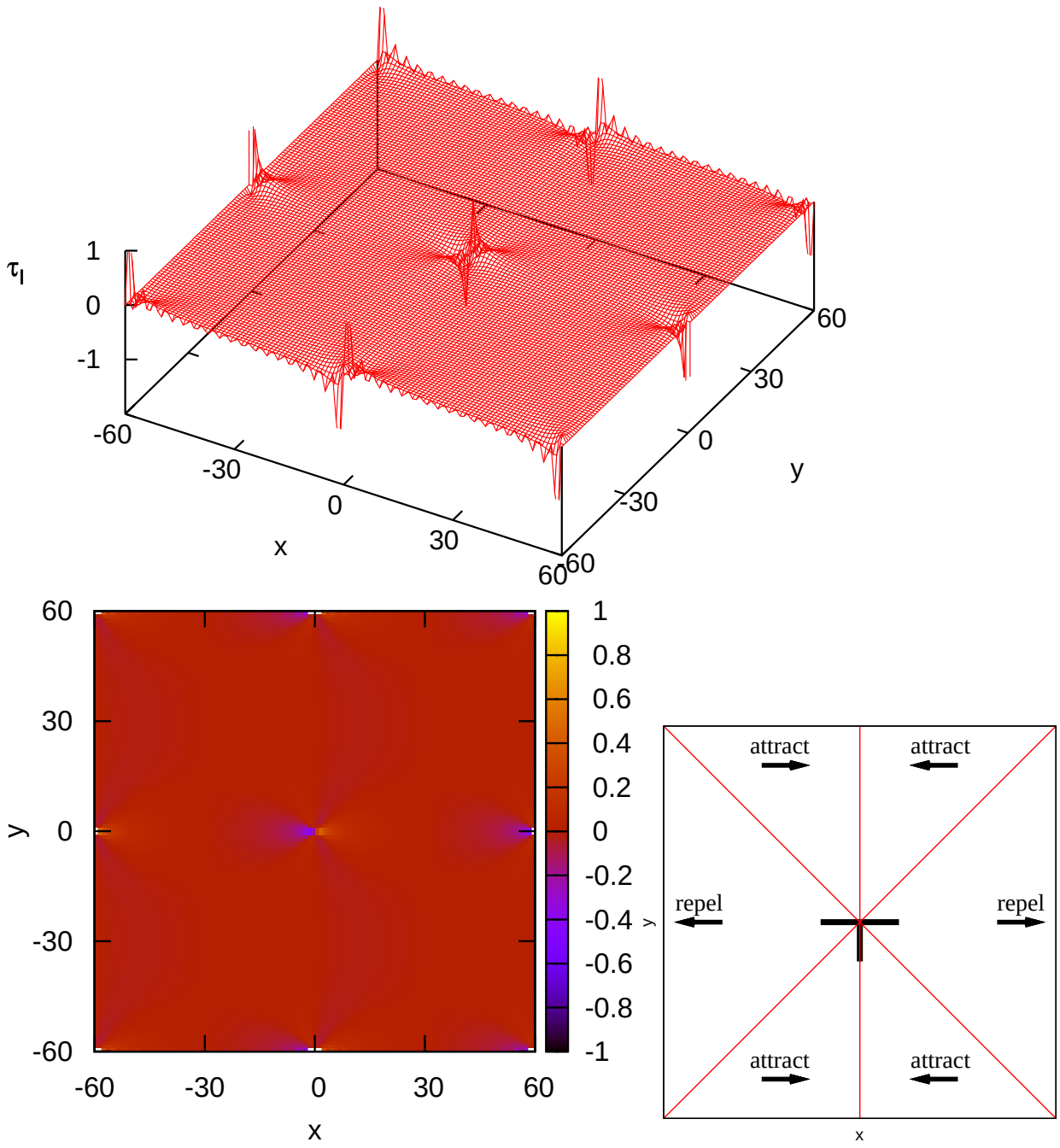

Figure A.3: (color online) The result of the converged Lekner series according to Way II (combined expression A.26 and A.29) for a small system of $L = 60$. It is depicted as a surface plot (top) and as a color contour plot (bottom left). The anisotropy of the interaction is indicated bottom right. In order to reveal its anisotropy Way II is plotted in an area of $2L \times 2L$.

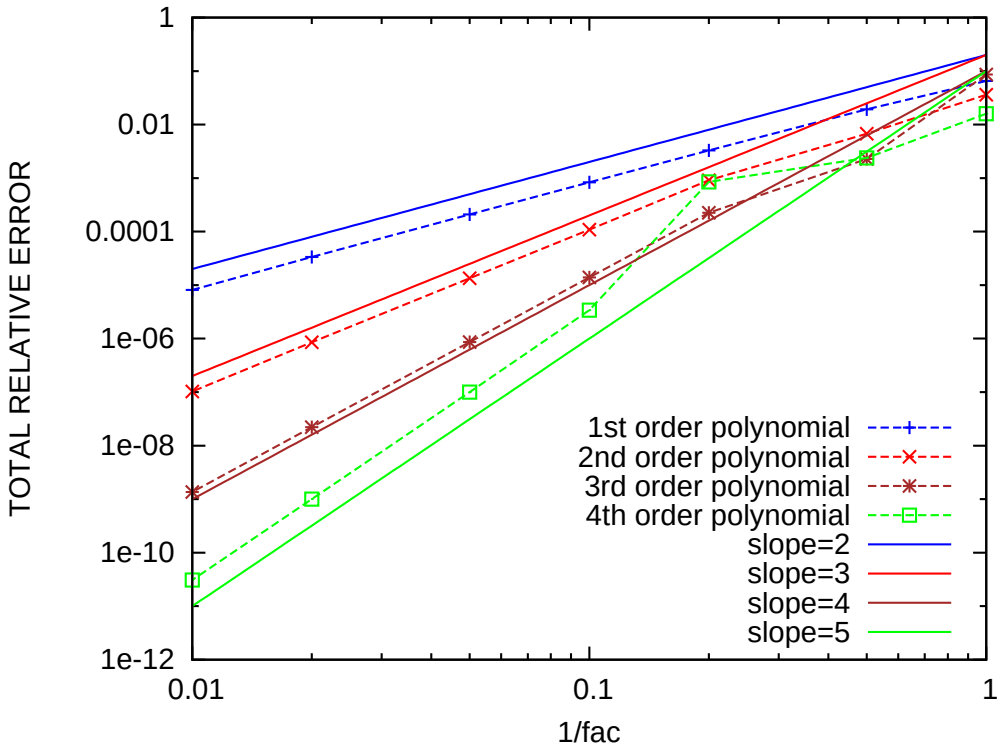

Figure A.4: (color online) The total relative error of our interpolation (Eq. A.55) from the look-up table for different fac, the spatial resolution in x.

Appendix B

Scaling Relations Derived

B.1 Distribution of Avalanche Sizes

B.1.1 Binned in Stress

As long as the dislocation activity, $V(t)$, is above the threshold value, i.e. $V(t) > V_{\text{th}}$, the system is exhibiting an avalanche. We define its size as

$$S = \int_{\text{avalanche}} V(t)dt. \tag{B.1}$$

The distribution of the avalanche sizes should scale with the closeness to the critical stress as

$$D_S(S,\tau) \sim S^{-\kappa} f_S[S(1-\tau/\tau_c)^{1/\sigma}]. \tag{B.2}$$

Essentially it exhibits a power law behavior, $D_S(S) \sim S^{-\kappa}$, up to a maximum, "cutoff", size $S_{\max}$, which increases as the stress, τ, approaches the critical value, τ_c

$$S_{\max} \sim \left(1 - \frac{\tau}{\tau_c}\right)^{-\frac{1}{\sigma}}. \tag{B.3}$$

B.1.2 Integrated in Stress

If one now integrates the binned-in-stress distribution over the entire range of stress, $\tau = 0$ to $\tau = \tau_c$ obtains the stress-integrated distribution:

$$\begin{aligned} D_{S,\text{int}}(S) &= \int_0^{\tau_c} D_S(S,\tau)d\tau \\ &= \int_0^{\tau_c} S^{-\kappa} f_S[S(1-\tau/\tau_c)^{1/\sigma}]d\tau \\ &\sim S^{-\kappa} \int_0^1 f_S[S^{\sigma}(1-\tau/\tau_c)]d(1-\tau/\tau_c) \end{aligned}$$

$$
\begin{aligned}
&= S^{-\kappa-\sigma}\int_0^{S^\sigma} f_S[S^\sigma(1-\tau/\tau_c)]d(S^\sigma(1-\tau/\tau_c)) \\
&= S^{-\kappa-\sigma}\int_0^{S^\sigma} f_S[w]dw \qquad \text{(B.4)} \\
&\sim S^{-(\kappa+\sigma)} \qquad \text{(B.5)}
\end{aligned}
$$

assuming that $f_S(w)$ is a well-behaved and bounded function (and the integral over f_S converges). This is usually the case for $f_S(w)$ since it expresses a probability distribution function. More specifically $f_S(w \to \infty) \to 0$ and $f_S(w \to 0) \to 1$.

B.2 Distribution of Avalanche Durations

B.2.1 Binned in Stress

The cutoff size of the $D_S(S,\tau)$ scales as $S_{\max} \sim (1-\tau/\tau_c)^{-1/\sigma}$. On the other hand one can plot the distribution of avalanche durations t_{aval}. It should also exhibit a power law that gets truncated by a cutoff duration, $t_{\text{aval,max}}$, that decreases the further the stress is from the critical stress,

$$
t_{\text{aval,max}} \sim \xi^z \sim \left(1-\frac{\tau}{\tau_c}\right)^{-\nu z}. \qquad \text{(B.6)}
$$

For the distribution of avalanche durations at stress τ we can write down the following expression:

$$
D(t_{\text{aval}},S,\tau) \sim S^{-x} f[S(1-\tau/\tau_c)^{1/\sigma}, t_{\text{aval}}/S^{\sigma\nu z}] \qquad \text{(B.7)}
$$

In order to find the unknown exponent x we need to integrate out the duration t_{aval} variable and compare the result to the size distribution.

$$
\begin{aligned}
\int D(t_{\text{aval}},S,\tau)dt_{\text{aval}} &\sim \int S^{-x} f[S(1-\tau/\tau_c)^{1/\sigma}, t_{\text{aval}}/S^{\sigma\nu z}]dt_{\text{aval}} \\
&\sim S^{-x+\sigma\nu z}\int f[S(1-\tau/\tau_c)^{1/\sigma}, t_{\text{aval}}/S^{\sigma\nu z}]d(t_{\text{aval}}/S^{\sigma\nu z}) \\
&\sim S^{-x+\sigma\nu z} f[S(1-\tau/\tau_c)^{1/\sigma}]. \qquad \text{(B.8)}
\end{aligned}
$$

Comparing the above with $D_S(S,\tau) \sim S^{-\kappa} f_S[S(1-\tau/\tau_c)^{1/\sigma}]$ we get $x = \kappa+\sigma\nu z$. To find the distribution of avalanche durations that does not depend on the size S we need to integrate over S.

$$
D_t(t_{\text{aval}},\tau) \sim \int D(t_{\text{aval}},S,\tau)dS
$$

$$
\begin{aligned}
&\sim \int S^{-\kappa-\sigma\nu z} f[S(1-\tau/\tau_c)^{1/\sigma}, t_{\text{aval}}/S^{\sigma\nu z}]dS \\
&\sim t_{\text{aval}}^{-(\kappa+\sigma\nu z)/\sigma\nu z} \int f[t_{\text{aval}}(1-\tau/\tau_c)^{\nu z}, t_{\text{aval}}/S^{\sigma\nu z}]dS \\
&\sim t_{\text{aval}}^{-(\kappa+\sigma\nu z-1)/\sigma\nu z} \int f[t_{\text{aval}}(1-\tau/\tau_c)^{\nu z}, t_{\text{aval}}/S^{\sigma\nu z}]d(S/t_{\text{aval}}^{1/\sigma\nu z}) \\
&\sim t_{\text{aval}}^{-(\kappa+\sigma\nu z-1)/\sigma\nu z} f_t[t_{\text{aval}}(1-\tau/\tau_c)^{\nu z}] \qquad \text{(B.9)}
\end{aligned}
$$

which can be simplified to

$$
D_t(t_{\text{aval}}, \tau) \sim t_{\text{aval}}^{-\kappa_t} f_t[t_{\text{aval}}(1-\tau/\tau_c)^{\nu z}] \qquad \text{(B.10)}
$$

where $\kappa_t = 1 + (\kappa - 1)/\sigma\nu z$.

B.2.2 Integrated in Stress

We can integrate the duration distribution over the entire stress range, $\tau = 0 \to \tau_c$, and obtain the stress-integrated version:

$$
\begin{aligned}
D_{t,\text{int}}(t_{\text{aval}}) &= \int D_t(t_{\text{aval}}, \tau)d\tau \\
&= \int t_{\text{aval}}^{-\kappa_t} f_t[t_{\text{aval}}(1-\tau/\tau_c)^{\nu z}]d\tau \\
&\sim t_{\text{aval}}^{-\kappa_t} \int f_t[t_{\text{aval}}^{1/\nu z}(1-\tau/\tau_c)]d(1-\tau/\tau_c) \\
&= t_{\text{aval}}^{-\kappa_t-1/\nu z} \int f_t[t_{\text{aval}}^{1/\nu z}(1-\tau/\tau_c)]d(t_{\text{aval}}^{1/\nu z}(1-\tau/\tau_c)) \\
&= t_{\text{aval}}^{-\kappa_t-1/\nu z} \int f_t[w]dw \\
&\sim t_{\text{aval}}^{-(\kappa_t+1/\nu z)}. \qquad \text{(B.11)}
\end{aligned}
$$

with $f_t(w)$ a well-behaved and bounded function that gives a finite integral ($f_t(w \to \infty) \to 0$ and $f_t(w \to 0) \to 1$).

B.3 Distribution of Avalanche Energies

B.3.1 Binned in Stress

The energy of a slip avalanche has been shown to relate to the square of the activity, which leads us to define the energy of a slip avalanche to be

$$E = \int_{\text{avalanche}} V(t)^2 dt \tag{B.12}$$

where the integral is taken over the duration t_{aval} of an avalanche. The energy of an avalanche scales with the collective speed and duration like

$$E \sim V^2 t_{\text{aval}} \sim (S/t_{\text{aval}})^2 t_{\text{aval}} \sim S^2/t_{\text{aval}} \sim S^{2-\sigma\nu z} \tag{B.13}$$

The distribution of energies should then have the scaling form,

$$D(E, t_{\text{aval}}, S, \tau) \sim S^{-y} f(E/S^{2-\sigma\nu z}, S(1-\tau/\tau_c)^{1/\sigma}, t_{\text{aval}}/S^{\sigma\nu z}) \tag{B.14}$$

In order to find the new exponent y we had to integrate the above distribution over the energies and obtain a form,

$$\begin{aligned} D(t_{\text{aval}}, S, \tau) &\sim \int D(E, t_{\text{aval}}, S, \tau) dE \\ &\sim \int \frac{1}{S^y} f(E/S^{2-\sigma\nu z}, S(1-\tau/\tau_c)^{1/\sigma}, t_{\text{aval}}/S^{\sigma\nu z}) dE \\ &\sim \frac{1}{S^{y-2+\sigma\nu z}} f(S(1-\tau/\tau_c)^{1/\sigma}, t_{\text{aval}}/S^{\sigma\nu z}) \end{aligned} \tag{B.15}$$

we can directly compare to $D(t_{\text{aval}}, S, \tau)$ above. We find the value $x = \kappa + \sigma\nu z$ and get $y = \kappa + 2$. The distribution of energies results if we integrate out the slip size S and duration t_{aval}.

$$\begin{aligned} D_E(E, \tau) &\sim \int D(E, t_{\text{aval}}, S, \tau) dt_{\text{aval}} dS \\ &\sim \frac{1}{E^{\frac{\kappa+2}{2-\sigma\nu z}}} \int f(E(1-\tau/\tau_c)^{\frac{2-\sigma\nu z}{\sigma}}, S(1-\tau/\tau_c)^{1/\sigma}, t_{\text{aval}}(1-\tau/\tau_c)^{\nu z}) dt_{\text{aval}} dS \\ &\sim \frac{(1-\tau/\tau_c)^{-\nu z - \frac{1}{\sigma}}}{E^{\frac{\kappa+2}{2-\sigma\nu z}}} f(E(1-\tau/\tau_c)^{\frac{2-\sigma\nu z}{\sigma}}) \\ &\sim \frac{1}{E^{1+\frac{\kappa-1}{2-\sigma\nu z}}} f_E(E(1-\tau/\tau_c)^{\frac{2-\sigma\nu z}{\sigma}}) \end{aligned} \tag{B.16}$$

B.3.2 Integrated in Stress

We can integrate the energy distribution over the entire stress range, $\tau = 0 \rightarrow \tau_c$, and obtain the stress-integrated expression:

$$\begin{aligned} D_{E,\mathrm{int}}(E) &= \int D_E(E(1-\tau/\tau_c)^{\frac{2-\sigma\nu z}{\sigma}})d(1-\tau/\tau_c) \\ &\sim \frac{1}{E^{1+\frac{\kappa-1}{2-\sigma\nu z}}} \int f_E(E(1-\tau/\tau_c)^{\frac{2-\sigma\nu z}{\sigma}})d(1-\tau/\tau_c) \\ &\sim \frac{1}{E^{1+\frac{\kappa-1+\sigma}{2-\sigma\nu z}}} \int f_E(E^{\frac{\sigma}{2-\sigma\nu z}}(1-\tau/\tau_c))d(E^{\frac{\sigma}{2-\sigma\nu z}}(1-\tau/\tau_c)) \\ &\sim \frac{1}{E^{1+\frac{\kappa-1+\sigma}{2-\sigma\nu z}}} \int f_E[w]dw \\ &\sim \frac{1}{E^{1+\frac{\kappa-1+\sigma}{2-\sigma\nu z}}} \end{aligned} \tag{B.17}$$

with $f_E(w)$ a well-behaved and bounded function that gives a finite integral ($f_E(w \rightarrow \infty) \rightarrow 0$ and $f_E(w \rightarrow 0) \rightarrow 1$).

References

[1] M. Zaiser. Scale invariance in plastic flow of crystalline solids. *Advances in Physics*, 55(1):185–245, 2006.

[2] W.F. Hosford. *Mechanical Behavior of Materials*. Cambridge University Press, 2005.

[3] J. P. Hirth and J. Lothe. *Theory of Dislocations*. John Wiley and Sons, Inc., New York, USA, 2nd edition, 1982.

[4] D.M. Dimiduk, C. Woodward, R. LeSar, and M.D. Uchic. Scale-Free Intermittent Flow in Crystal Plasticity. *Science*, 312(5777):1188–1190, 2006.

[5] M.-C. Miguel, A. Vespignani, S. Zapperi, J. Weiss, and J.R. Grasso. Intermittent dislocation flow in viscoplastic deformation. *Nature*, 410:667–671, 2001.

[6] M. Zaiser, B. Marmo, and P. Moretti. The 'yielding transition' in crystal plasticity - discrete dislocations and continuum models. *Proceedings of Science (Statistical Mechanics of Plasticity and Related Instabilities)*, 053, 2005.

[7] M.-C. Miguel, A. Vespignani, S. Zapperi, J. Weiss, and J. R. Grasso. Complexity in dislocation dynamics: model. *Mater. Sci. Eng. A*, 309-310:324–327, 2001.

[8] L. Laurson and M. Alava. 1/f noise and avalacnhe scaling in plastic deformation. *Phys. Rev. E*, 74:066106, 2006.

[9] P. D. Ispanovity, I. Groma, G. Gyorgyi, F. F. Csikor, and D. Weygand. Submicron plasticity: Yield stress, dislocation avalanches, and velocity distribution. *Phys. Rev. Lett.*, 105:085503, 2010.

[10] G. Tsekenis, N. Goldenfeld, and K. A. Dahmen. Dislocations jam at any density. *Phys. Rev. Lett.*, 106:105501, 2011.

[11] F. F. Csikor, C. Motz, D. Weygand, M. Zaiser, and S. Zapperi. Dislocation avalanches, strain bursts, and the problem of plastic forming at the micrometer scale. *Science*, 318:251, 2007.

[12] M Koslowski, R. LeSar, and R. Thomson. Avalanches and scaling in plastic deformation. *Phys. Rev. Lett.*, 93(12), 2004.

[13] M Koslowski. Scaling laws in plastic deformation. *Phil. Mag.*, 87(8-9):1175–1184, 2007.

[14] P. Y. Chan, G. Tsekenis, J. Dantzig, K. A. Dahmen, and N. Goldenfeld. Plasticity and dislocation dynamics in a phase field crystal model. *Phys. Rev. Lett.*, 105:015502, 2010.

[15] J.P. Sethna, K.A. Dahmen, and C.R. Myers. Crackling noise. *Nature*, 410:242–250, 2001.

[16] M. Zaiser and P. Moretti. Fluctuation phenomena in crystal plasticity - a continuum model. *J. Stat. Mech.*, P08004, 2005.

[17] T. Richeton, P. Dobron, F. Chmelik, J. Weiss, and F. Louchet. On the critical character of plasticity in metallic single crystals. *Mater. Sci. Eng. A*, 424:190–195, 2006.

[18] T. Richeton, J. Weiss, and F. Louchet. Dislocation avalanches: Role of temperature, grain size and strain hardening. *Acta Mat.*, 53:4463–4471, 2005.

[19] J. Weiss, F. Lahaie, and J.R. Grasso. Statistical analysis of dislocation dynamics during viscoplastic deformation from acoustic emission. *J. Geo. Res,*, 105:433–442, 2000.

[20] J. Weiss and J.R. Grasso. Acoustic emission in single crystals of ice. *J. Phys. Chem. B*, 101:6113–6117, 1997.

[21] M. Zaiser, J. Schwerdtfeger, A. S. Schneider, C. P. Frick, B. G. Clark, P. A. Gruber, and E. Arzt. Strain bursts in plastically deforming molybdenum micro- and nanopillars. *Philosophical Magazine*, 88(30-32):3861 – 3874, 2008.

[22] Steffen Brinckmann, Ju-Young Kim, and Julia R. Greer. Fundamental differences in mechanical behavior between two types of crystals at the nanoscale. *Phys. Rev. Lett.*, 100(15):155502, Apr 2008.

[23] N. Goldenfeld. Roughness-Induced Critical Phenomena in a Turbulent Flow. *Phys. Rev. Lett.*, 96:044503, 2006.

[24] M.-C. Miguel, A. Vespignani, M. Zaiser, and S. Zapperi. Dislocation jamming and andrade creep. *Phys. Rev. Lett.*, 89(16):165501, 2002.

[25] D. S. Fisher. Collective transport in random media: from superconductors to earthquakes. *Physics Reports*, 301:113–150, 1998.

[26] M. Cieplak and M. O. Robbins. Dynamical transition in quasistatic fluid invasion in porous media. *Phys. Rev. Lett.*, 60(20):2042–2045, 1988.

[27] B. Koiler and M. O. Robbins. Morphology transitions in three-dimensional domain growth with gaussian random fields. *Phys. Rev. B*, 62(9):5771–5778, 2000.

[28] S. Zapperi, P. Cizeau, G. Durin, and H. E. Stanley. Dynamics of a ferromagnetic domain wall: Avalanches, depinning transition, and the Barkhausen effect. *Phys. Rev. B*, 58(10):6353–6366, 1998.

[29] L. Roters, A. Hucht, S. Lubeck, U. Nowak, and K. D. Usadel. Depinning transition and thermal fluctuations in the random-field ising model. *Phys. Rev. E*, 60(5):5202–5207, 1999.

[30] O. Narayan. Self-similar barkhausen noise in magnetic domain wall motion. *Phys. Rev. Lett.*, 77(3855), 1996.

[31] D. S. Fisher. Threshold behavior of charge-density waves pinned by impurities. *Phys. Rev. Lett.*, 50(19):1486–1489, 1983.

[32] D. S. Fisher. Sliding charge-density waves as a dynamical critical phenomenon. *Phys. Rev. B*, 31(3):1396–1427, 1985.

[33] P. B. Littlewood. Sliding charge-density waves: A numerical study. *Phys. Rev. B*, 33(10):6694–6708, 1986.

[34] O. Narayan and D. S. Fisher. Critical behavior of sliding charge-density waves in 4- dimensions. *Phys. Rev. B*, 46(18):11520–11549, 1992.

[35] A. A. Middleton and D. S. Fisher. Critical behavior of charge-density waves below threshold: Numerical and scaling analysis. *Phys. Rev. B*, 47(7):3530–3552, 1993.

[36] C. R. Myers and J. P. Sethna. Collective dynamics in a model of sliding charge-density waves. i. critical behavior. *Phys. Rev. B*, 47(17):11171–11193, 1993.

[37] A. A. Middleton. Thermal rounding of the charge-density-wave depinning transition. *Phys. Rev. B (R)*, 45(16):9465–9468, 1992.

[38] O. Narayan and D. S. Fisher. Threshold critical dynamics of driven interfaces in random media. *Phys. Rev. B*, 48(10):7030–7042, 1993.

[39] C. S. Nolle, B. Koiller, N. Martys, and M. O. Robbins. Morphology and dynamics of interfaces in random two-dimensional media. *Phys. Rev. Lett.*, 71(13):2074–2077, 1993.

[40] A. A. Middleton. Asymptotic uniqueness of the sliding state for charge-density waves. *Phys. Rev. Lett.*, 68(5):670–673, 1992.

[41] T. Nattermann, S. Stepanow, L.-H. Tang, and H. Leschhorn. Dynamics of interface depinning in a disordered medium. *J. Phys II France*, 2(8):1483–1488, 1992.

[42] F. Family and T. Vicsek. Scaling of the active zone in the eden process on percolation networks and the ballistic deposition model. *J. Phys. A: Math. Gen.*, 18:L75–L81, 1985.

[43] H. Leschhorn, T. Nattermann, S. Stepanow, and L.-H. Tang. *Ann. Phys. (Leipzig)*, 6:1–34, 1997.

[44] K. A. Dahmen, Y. Ben-Zion, and J.T. Uhl. A micromechanical model for deformation in solids with universal predictions for stress strain curves and slip avalanches. *Phys. Rev. Lett.*, 102:175501, 2009.

[45] D. S. Fisher, K. A. Dahmen, S. Ramanathan, and Y. Ben-Zion. Statistics of earthquakes in simple models of heterogeneous faults. *Phys. Rev. Lett.*, 78:4885–4888, Jun 1997.

[46] J. Lekner. Summation of coulomb fields in computer-simulated disordered systems. *Physica A*, 176:485–498, 1991.

[47] W.H Press, S.A. Teukolsky, W.T. Vetterling, and B.P. Flannery. *Numerical Recipes in C: The Art of Scientific Computing*. Cambridge University Press, Cambridge, England, 2nd edition, 1992.

[48] Andrew T. Jennings, Michael J. Burek, and Julia R. Greer. Microstructure versus size: Mechanical properties of electroplated single crystalline cu nanopillars. *Phys. Rev. Lett.*, 104(13):135503, Apr 2010.

[49] Christopher R. Weinberger and Wei Cai. Surface-controlled dislocation multiplication in metal micropillars. *Proceedings of the National Academy of Sciences*, 105(38):14304–14307, 2008.

[50] N. Friedman, A. T. Jennings, G. Tsekenis, J.-Y. Kim, M Tao, J. T. Uhl, J. R. Greer, and K. A. Dahmen. Statistics of dislocation slip avalanches in the smallest-ever nanocrystals explained by a simple mean field model. *submitted*, 2011.

[51] M. Zaiser and N. Nikitas. Slip avalanches in crystal plasticity: scaling of the avalanche cut-off. *J. Stat. Mech.*, P04013, 2007.

[52] B. Bako, B., I. Groma, G. Gyorgyi, and G. T. Zimanyi. Dislocation glasses: Aging during relaxation and coarsening. *Phys. Rev. Lett.*, 98(075701), 2007.

[53] Matthew C. Kuntz and James P. Sethna. Noise in disordered systems: The power spectrum and dynamic exponents in avalanche models. *Phys. Rev. B*, 62(17):11699–11708, Nov 2000.

[54] J. Weiss, J. R. Grasso, M.-C. Miguel, A. Vespignani, and S. Zapperi. Complexity in dislocation dynamics: experiments. *Mater. Sci. Eng. A*, 309-310:360–364, 2001.

[55] A.J. Liu and S.R. Nagel. Jamming in not just cool any more. *Nature*, 396:21, 1998.

[56] C.S. O'Hern, S.A. Langer, A.J. Liu, and S.R. Nagel. Random packings of frictionless particles. *Phys. Rev. Lett.*, 88:7, 2002.

[57] C.S. O'Hern, L.E. Silbert, A.J. Liu, and S.R. Nagel. Jamming at zero temperature and zero applied stress: The epitome of disorder. *Phys. Rev. E*, 68:011306, 2003.

[58] A.J. Liu and S.R. Nagel. The jamming transition and the marginally jammed solid. *Annu. Rev. Condens. Matter Phys.*, 1:347–369, 2010.

[59] G. I. Taylor. The mechanism of plastic deformation of crystals. part i. theoretical. *Proceedings of the Royal Society of London. Series A, Containing Papers of aMathematical and Physical Character*, 145(855):362–387, 1934.

[60] I. Groma and B. Bako. Probability distribution of internal stresses in parallel straight dislocation systems. *Phys. Rev. B*, 58(6):2969–2974, 1998.

[61] P. H. Chavanis. Effective velocity created by a point vortex in two-dimensional hydrodynamics. *Phys. Rev. E*, 65:056302, 2002.

[62] Pak Yuen Chan. *Ph.D. Thesis, Scaling and Pattern Formation in Condensed Matter Systems*. University of Illinois at Urbana-Champaign, 2007.

[63] K. R. Elder, Mark Katakowski, Mikko Haataja, and Martin Grant. Modeling elasticity in crystal growth. *Phys. Rev. Lett.*, 88:245701, 2002.

[64] K. R. Elder and Martin Grant. Modeling elastic and plastic deformations in nonequilibrium processing using phase field crystals. *Phys. Rev. E*, 70:051605, 2004.

[65] S. Majaniemi and M. Grant. Dissipative phenomena and acoustic phonons in isothermal crystals: A density-functional theory study. *Phys. Rev. B*, 75(5):054301, Feb 2007.

[66] Peter Stefanovic, Mikko Haataja, and Nikolas Provatas. phase-field crystals with elastic interactions. *Phys. Rev. Lett.*, 96:225504, 2006.

[67] H. M. Singer and I. Singer. Analysis and visualization of multiply oriented lattice structures by a two-dimensional continuous wavelet transform. *Phys. Rev. E*, 74:031103, 2006.

[68] J. Berry and M. Grant. Diffusive atomistic dynamics of edge dislocations in two dimensions. *Phys. Rev. E*, 73:031609, 2006.

[69] Pak Yuen Chan, Nigel Goldenfeld, and Jonathan Dantzig. Molecular dynamics on diffusive time scales from the phase field crystal equation. *Phys. Rev. E (R)*, 79:035701:1–4, 2009.

[70] C. Achim, M. Karttunen, K. Elder, E. Granato, T. Ala-Nissila, and S. Ying. Phase diagram and commensurate-incommensurate transitions in the phase field crystal model with an external pinning potential. *Phys. Rev. E*, 74:021104, 2006.

[71] K. R. Elder, N. Provatas, J. Berry, P. Stefanovic, and M. Grant. Phase-field crystal modeling and classical density functional theory of freezing. *Phys. Rev. B*, 75(6):64107, 2007.

[72] A. Travesset, R. A. White, and K. A. Dahmen. Crackling noise, power spectra, and disorder-induced critical scaling. *Phys. Rev. B*, 66(2):024430, Jul 2002.

[73] J.R. Sack and J. Urrutia. *Handbook of computational geometry*. North-Holland Publishing Co. Amsterdam, Netherlands, 2000.

[74] J. O'Rourke. *Computational Geometry in C*. Cambridge University Press, 1998.

[75] M. Mazars. Lekner summations. *J. Chem. Phys.*, 115(7):2955–2965, 2001.